Effect of intravenous recombinant tissue plasminogen activator on ischemic stroke in a mouse model of middle cerebral artery occlusion measured by optical micro-angiography

---

By: Sawan Hurst

Presented to the Department of Biomedical Engineering
within
The School of Medicine
and the
Oregon Health & Science University
in partial fulfillment of
the requirements for the degree of
Master of Science
in
Biomedical Engineering
August 2010

Department of Biomedical Engineering
School of Medicine
Oregon Health & Science University

CERTIFICATE OF APPROVAL

This is to certify that the M.S. dissertation of
Sawan Ananda Hurst
has been approved

_____

Ruikang Wang, Ph.D.
Professor, Thesis Advisor*

_____

András Gruber, M.D.
Associate Professor

_____

Nabil Alkayed, M.D. Ph.D.
Professor

_____

Owen McCarty, Ph.D.
Assistant Professor

_____

Dedication

I dedicate this work to:

My grandmother JoAnn Stroup; I still remember my ABCs and the fly swatter. Thank you.

My parents John Hurst and Jerri Stroup; Thank you for this wonderful life you brought me into.

And finally and most close to my heart,

Anna, Leo, Ella, and Mystic Hurst; for their constant support and love through this journey we are on together.

Acknowledgment

Committee Members:

R.K. Wang: Thank you for pushing me towards my goals and future.

Andras Gruber: Thank you for always putting things into perspective with a smile on your face.

Owen McCarty: Thank you for helping me across the finish line.

Nabil Alkayed: Thank you for all the surgical training, space, and time.

Laboratory members who have helped with this work;

Yali Jia

An Lin

Yin Xin

Wenri Zhang

Erik Tucker

Table of Contents

List of Figures

List of Abbreviations

OMAG = optical micro-angiography

MCAO = middle cerebral artery occlusion

tPA = tissue Plasminogen Activator

CVD= Cardiovascular Disease

FIIa = activated factor II

FIX = factor IX

FIXa = activated factor IX

FV = factor V

FVa = activated factor V

FVIIa = activated factor VII

FVIII = factor VIII

FVIIIa = activated factor VIII

FX = factor X

FXa = activated factor X

FXI = factor XI

FXIa = activated factor XI

FXII = factor XII

FXIIa = activated factor XII

FXIII = factor XIII

TF = tissue factor

CCA = common carotid artery

ECA = external carotid atery

MCA = middle cerebral artery

RM = reference Mirror

FC = 2X2 fiber coupler

PC = polarization controller

L1-L5 = lens 1 through 5

SLD = super luminescent diode

OC = optical circulator

CCD = charge coupled device (camera)

OCT = optical coherence tomography

TDOCT = Time-domain OCT

FD = frequency domain

IAP = Iodoantipyrine

TTC = 2,3,5-triphenyltetrazolium chloride

LDF = transcranial Laser Doppler Flow

3D = three dimensional

2D = two dimensional

FDOCT = frequency domain optical coherence tomography

Abstract

Use of optical microangiography in the investigation of experimental ischemic stroke in mice.

Sawan A. Hurst, B.S.
Master of Science
Department of Biomedical Engineering
Oregon Health & Science University
School of Medicine
1 of August 2010

Thesis Advisor: Ruikang Wang, Ph.D.

We have developed a new optical micro-angiography (OMAG) imaging technique that is capable of resolving 3D distribution of dynamic blood perfusion at a 10 μm resolution within microcirculatory beds *in vivo*. The imaging contrast of blood perfusion is based on endogenous light scattering from moving blood cells within vessels, thus no exogenous contrast agents are necessary. The technique effectively separates the moving and static scattering elements within tissue to achieve high resolution images of blood flow, mapped into the 3-D optically sectioned tissue beds, at speeds that allow for perfusion assessment in *vivo*. We used OMAG to visualize the cerebral microcirculation of adult living mice through the intact cranium. These measurements would be difficult, if not impossible, with other optical imaging techniques. The purpose of this study is to validate OMAG as a method and assess its potential applications in the studies of cerebrovascular perfusion during and after induced stroke in treated mice. To do this we treated animals with tissue plasminogen activator (tPA) or vehicle and then used OMAG to obtain real time images to compare the mechanisms of reperfusion of each treatment. From these images tPA is shown to greatly effect the reperfusion. It is shown that tPA increases the reperfusion rate and blood volume into the affected hemisphere which in turn increases the animals' behavior and survival chances.

Chapter 1: Background

1.1 Rationale

Stroke is the third leading cause of death in the United States (1). As seen in Figure 1, approximately 6% of deaths every year are due to stroke. Out of 2.5 million deaths a year 150,000 are due to cerebrovascular disease. Annually however, there are 795,000 strokes with 87% of them being due to an ischemic injury (2, 3). This leaves approximately 645,000 people that have post-ischemic injuries which can cause chronic disabilities (3).

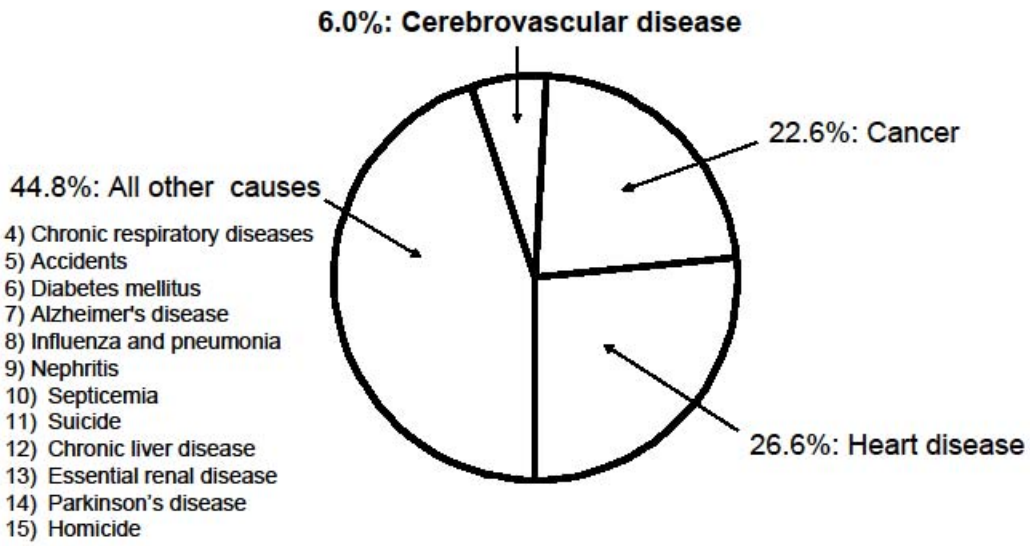

Figure 1: Causes of death in the United States from 2000-2008. Between these years there were approximately 2.5 million deaths per year in the United States. Deaths due to stroke were approximately 150,000 people or 6% of the total yearly deaths. Stroke is the third leading cause of death in America.

As seen in Figure 2, a large percentage of patients face long term disabilities which can have multi-symptom or single-symptom affects on their lives. It has been stated by some patients that they considered death a better outcome (4).

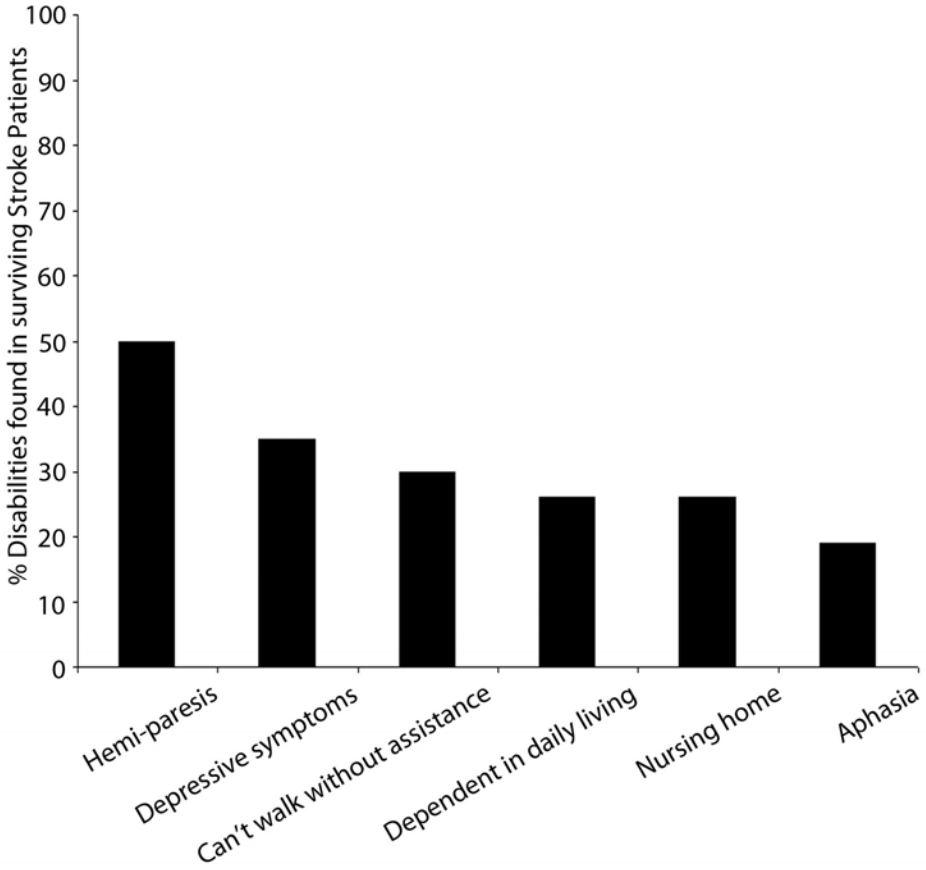

Figure 2: Percentage of patients with observed disabilities due to chronic brain injury caused by ischemic stroke. Annually there are approximately 615,000 stroke survivors. Patients exhibit one or multiple symptoms listed in above graph. Some patients claim death would be a better outcome due to disabilities.

Because of the long and short term effect of stroke it is estimated that indirect and direct costs are greater then sixty billion dollars annually (4). As seen in Figure 3 direct costs include hospital care, nursing home care, home healthcare, physicians costs, drugs, and medical disposables which when totaled come to more then 43.7 billion dollars annually. While the indirect costs due to mortality and morbidity can be estimated as high as 21.8 billion dollars. Cerebrovascular diseases have an expensive and heavy burden on society. It is thus important to understand them so that we can better treat them.

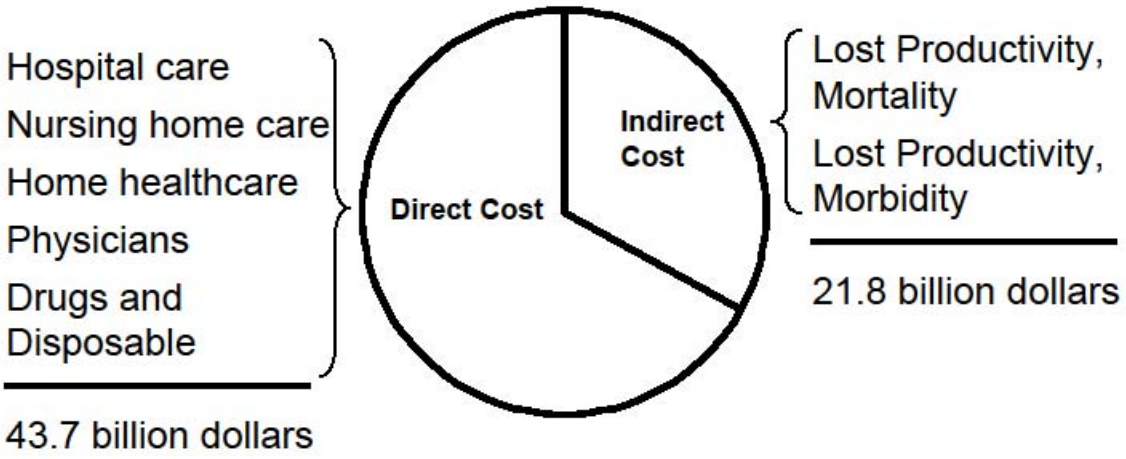

Figure 3: Indirect and Direct costs of stroke. Due to the cost of care for patients and the loss of their productivity in the work place stroke is considered to have a 65.5 billion dollar economic toll on patients, hospitals, and society.

1.2 Hemostasis & Thrombosis

What is the cause of cerebrovascular disease? Firstly, cerebrovascular disease is a form of cardiovascular disease (CVD). Thrombosis and hemostasis, although essential for survival, can cause CVDs. Through the improper activation of platelets and coagulation factors essential to hemostasis and thrombosis these diseases are triggered. The thrombotic and hemostatic pathologies caused by these triggers are due to platelet and coagulation factors being out of balance due to genetic disposition, trauma, or acquired auto-immune response to name some. The formation of a thrombus, which cause atherosclerotic plaques, starts from a cascade of coagulation factors through the intrinsic and or extrinsic coagulation pathways as described in Figure 4 (5, 6).

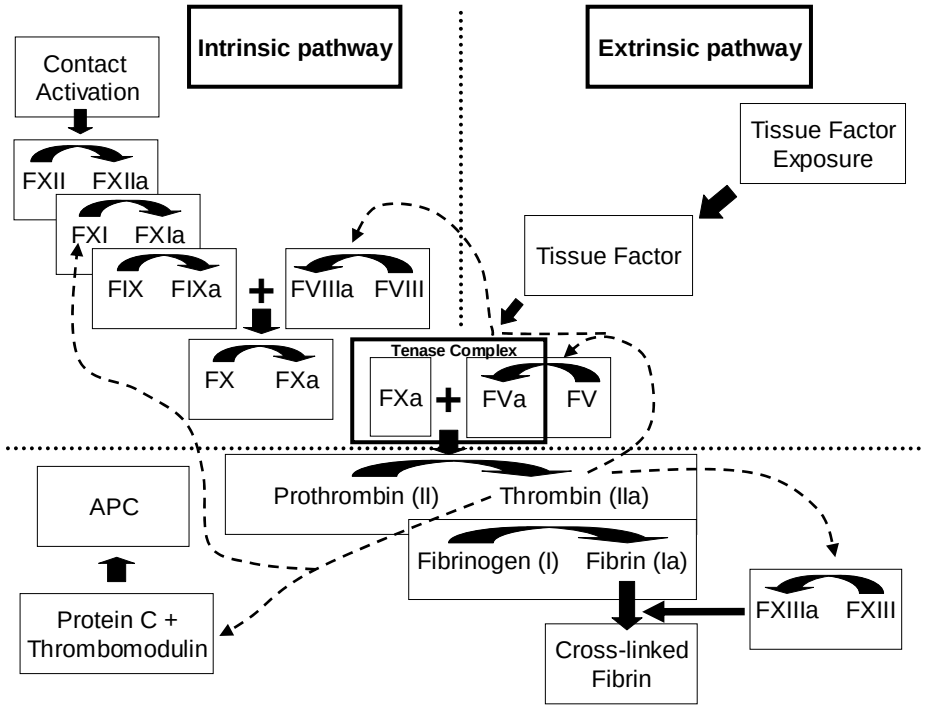

Figure 4: Coagulation Cascade. The intrinsic and extrinsic pathways contribute to hemostasis. Thrombosis caused by disease can drive this cascade into a hyper-coagulation response.

The formations of these atherosclerotic plaques, as seen in Figure 5, are the cause of ischemic stroke. These plaques are formed over time under blood flow from the activation of platelets and coagulation factors. When they rupture and embolize the result is the downstream ischemic injury caused by occluding blood flow to the brain. To combat these embolic events, thrombolytic agents and anticoagulants such as tissue-type plasminogen activator (tPA) are used to degrade thrombi. These thrombi which cause the occlusion to vessel are then removed allowing reperfusion into the ischemic tissue (7, 8). Tissue Plasminogen Activator has a thrombolytic activity by activating plasmin that is near a fibrin rich deposit. Plasmin then chews fibrin into its degradation product, as seen in Figure 6.

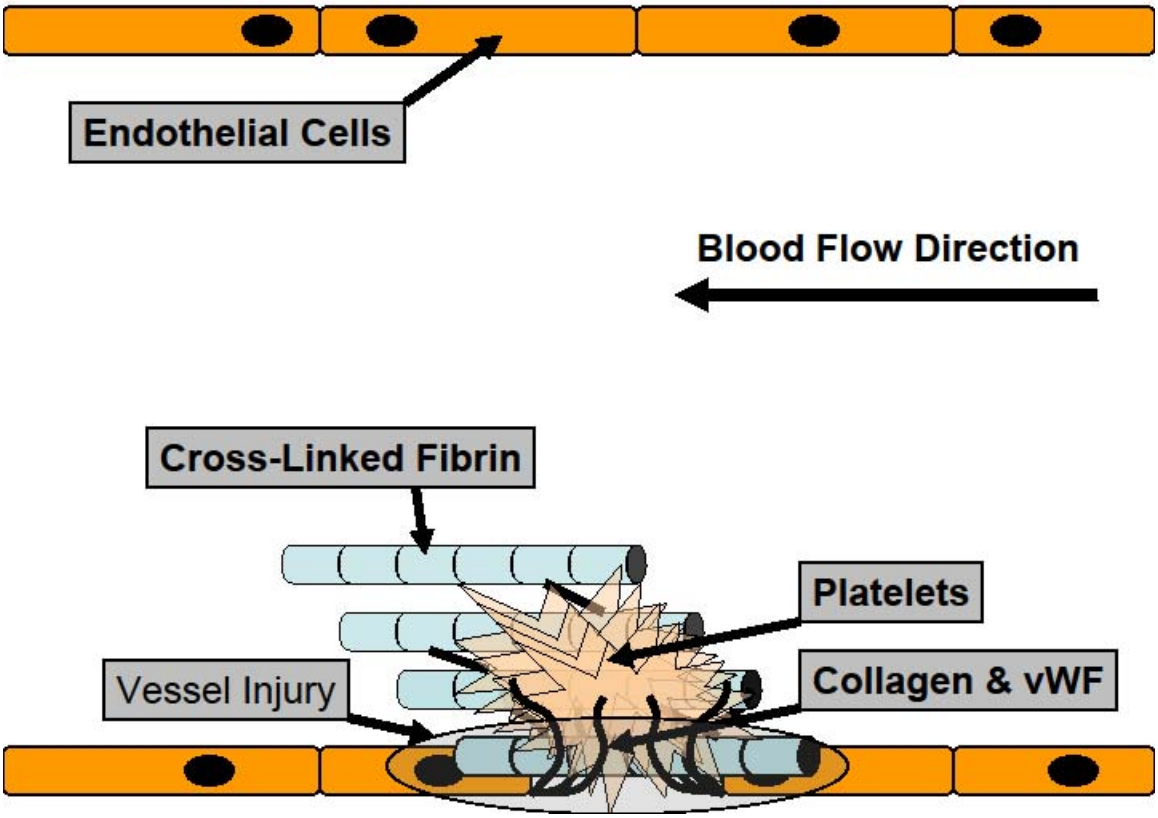

Figure 5: Vessel injury triggers hemostatic plug formation. Normal hemostasis requires coagulation for vessel repair. Thrombosis due to disease can lead to formation of an occlusion which can block blood flow causing ischemia to distal tissues.

These plaques are formed over time under blood flow from the activation of platelets and coagulation factors. When they rupture and embolize the result is the downstream ischemic injury caused by occluding blood flow to the brain. To combat these embolic events, thrombolytic agents and anticoagulants such as tissue-type plasminogen activator (tPA) are used to degrade thrombi. These thrombi which cause the occlusion to vessel are then removed allowing reperfusion into the ischemic tissue (7, 8). tPA has a thrombolytic activity by activating plasmin that is near a fibrin rich deposit. Plasmin then chews fibrin into its degradation product as seen in Figure 6.

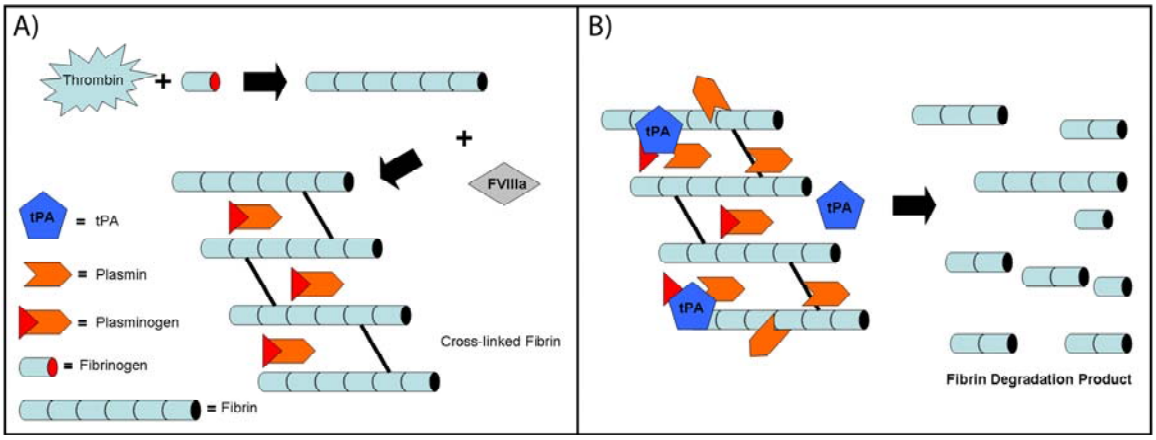

Figure 6: Diagram of the formation of a fibrin clot followed by thrombolysis. A) Formation of fibrin from thrombin activation. Fibrin is then cross-linked to create a fibrous material. B) Representation of tPA activating plasmin. Plasmin then degrades fibrin into D-dimer and fibrin degradation products.

1.3 Modern Therapeutic Treatment

At present, early tissue-type plasminogen activator (tPA)-induced thrombolysis is the only FDA approved treatment that improves neurological outcome (9, 10) of ischemic stroke. However thrombolytic treatments have been associated with hemorrhagic bleeding as a severe side effect. It has also been shown that tPA treatment increases risk for brain hemorrhaging and is capable of directly damaging neurons as well as having a 3-hour time window of efficacy (11). Accordingly, the use of tPA is restricted to a small percentage of stroke patients (12).

Since the introduction of tPA to clinics thirty years ago there have been no other pharmacological treatments developed that have worked to help the outcome of stroke. Despite the multitude of clinical trials, why have so many tested compounds failed? Numerous agents that have proved neuroprotective in experimental stroke have failed in subsequent clinical trials (13). More thrombosis-specific, and thus safer, antithrombotic agents are desperately needed and it is critical to elucidate the interactions that occur after the presentation of the injury. It is also important to distinguish the

pathophysiological changes that occur due to the treatment of the injury. This can be accomplished through modern imaging techniques. It has become standard practice in clinics to treat stroke depending on the image of the occluded area of the brain obtained through angiography, Computed Tomography (CT), and Magnetic Resonance Imaging (MRI) (14). Physicians relied on echoencephalography, thermography, radioisotope labeling, and skull films to treat patients before present day imaging techniques. Over time, imaging techniques are becoming readily used and relied upon for clinical treatment. The present day standard techniques are limited though due to the resolution of image obtained and to the signal to noise ratio of the individualistic system. Pre-clinical research, where clinical trail agents are first tested, use small animal models to test new compounds. Present day imaging techniques have a limited imaging resolution and ability to view the effect of new compounds on small animal models used to represent disease conditions.

In this study we have proposed the use of a newly developed optical micro-angiography (OMAG) imaging technique to image the effect of tPA in a mouse model of ischemic stroke. Optical microangiography is a novel noninvasive imaging technique that is capable of resolving 3D distribution of dynamic blood perfusion in real time, *in vivo*, at a 10 micron resolution at 2 mm depth from the tissue surface. OMAG is based on the differential analysis of the Doppler Effect on light scattering by moving blood cells within vessels versus stationary tissues. By using OMAG, we compared the effect of early treatment of reversible intraluminal middle carotid artery occlusion (MCAO) with tissue plasminogen activator (tPA) to vehicle (saline) on the cortical blood perfusion in a mouse model of ischemic stroke. Infusion of tPA both inhibited progressive cortical blood vessel occlusions due to thrombogenesis during MCAO, and enhanced post-MCAO reperfusion of the parietal cortex compared to saline infusion. This is the first report to demonstrate, *in vivo*, that the profibrinolytic agent, tPA, may act in part by reducing spatial extension of the ischemic region during occlusion of the MCA as well as allowing larger blood volume

hemispherical reperfusion. This study also validates OMAG as a useful research tool that could provide information about the mechanism of action of drugs, including tPA, that has been used to treat ischemic stroke. OMAG thus has potential applications in pharmacological studies of cerebrovascular perfusion in real time, during and after MCAO-induced stroke in a mouse model without the need for tissue sampling.

1.4 Hypothesis

We have developed a new optical micro-angiography (OMAG) imaging technique that is capable of resolving 3D distribution of dynamic blood perfusion at a 10 μm resolution within microcirculatory beds *in vivo*. The imaging contrast of blood perfusion is based on endogenous light scattering from moving blood cells within vessels, thus no exogenous contrast agents are necessary. The purpose of this study is to validate OMAG as a method and assess its potential applications in the studies of cerebrovascular perfusion during and after induced stroke in treated mice. To do this we are using the standard treatment modalities (tPA vs. vehicle) and are using OMAG to obtain real time images of their mechanism of action.

Chapter 2. Common Materials and Methods

2.1 Middle Cerebral Artery Occlusion (MCAO)

Mice are anesthetized initially with 4-5% halothane in oxygen enriched air using an induction chamber followed by a face mask, without premedication. All surgery is conducted under aseptic conditions. Sterile instrument tips via glass bead sterilizers and drapes are used. The surgeon wears surgical gown, surgical mask, and sterile gloves. Surgical anesthesia is induced with 4% and maintained with 1-2% isoflurane via face-mask in O_2-enriched air. Surgical sites are clipped free of hair and the skin is prepared with betadine. Temporalis muscle (needle sensor in muscle) and rectal (rectal sensor) temperatures are maintained at near 37^{O}C throughout the surgical procedure using a heating lamp (typically 18 inches above the animal), and warm water blanket underneath the animal. A midline ventral neck incision is made, carotids isolated (Figure 7), and unilateral (typically right side) MCAO is performed by inserting a 6.0 gauge nylon monofilament (with a heat-treated small and smooth bulge at the end) into the internal carotid artery from and via an external carotid artery stump (Figure 8).

Next a right inguinal incision is made, the femoral artery and vein are isolated, and a small custom made infusion system, (250 uL total volume) is inserted into the femoral vein directed proximal to entry point, entering the ascending femoral vein about 2 mm below the portal vein bifurcation.

In the treatment study groups, tPA (10 mg/kg/hr) or the vehicle (saline/dextrose) is infused at 250 ul per hour through the femoral infusion system in a volume of up to 250 uL 15 minutes after positioning the filament in the MCA. The filament is then positioned for occlusion at a distance of 6mm from the internal carotid/pterygopalatine artery bifurcation to the suture tip. Occlusion is confirmed and monitored until 30 minutes post reperfusion by a transcranial Laser Doppler flow (LDF) (Moore Instruments) probe. After 60 minutes of suture

occlusion the suture is withdrawn, establishing circulation to the brain. At this point, the animal

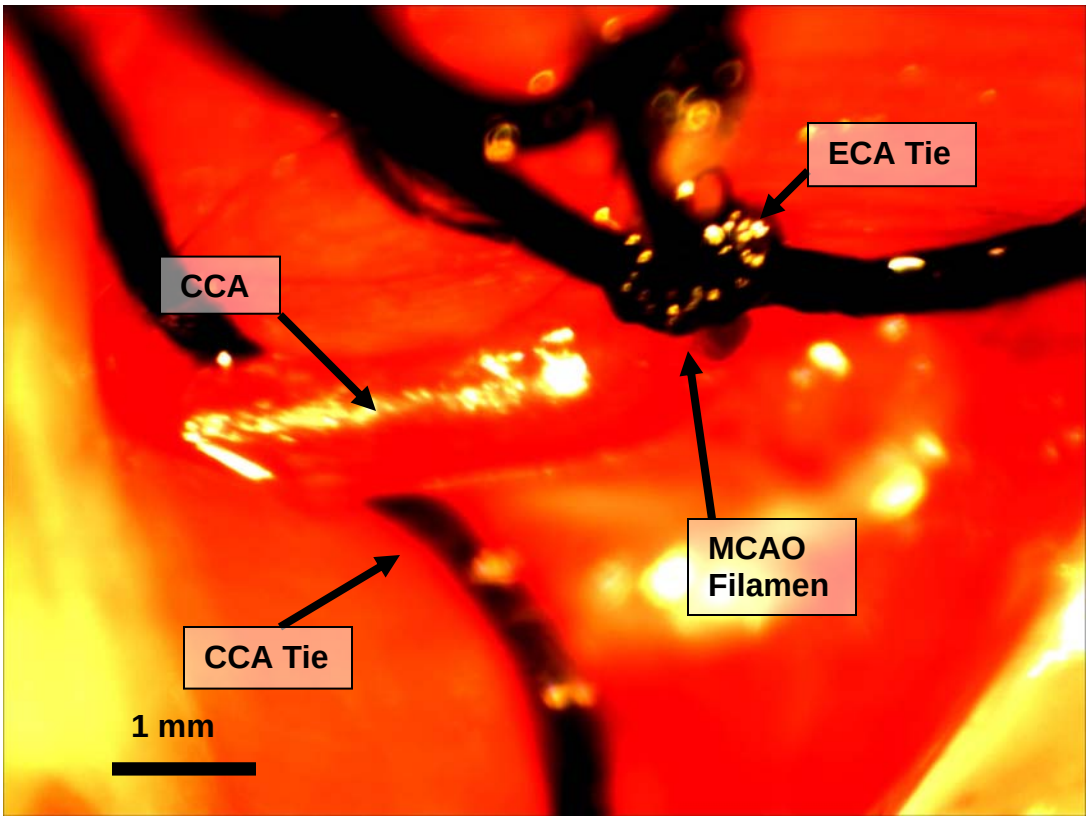

Figure 7: Picture of isolated CCA and ECA in mouse MCAO model. The filament shown in picture is progressed towards head (right) to occlude MCA region of brain.

is allowed to emerge from anesthesia. Immediate neurological outcome is determined and documented after emergence by documenting abnormal posturing, reflexes, or peripheral weakness. During the recovery period, the mouse receives supportive postoperative care. At the conclusion of the experiment (22 hours of reperfusion), the animals are deeply anesthetized with 4-5% isoflurane. The animal's blood is replaced with physiologic saline by left ventricular puncture (inlet) and left atrium puncture (outlet). The brain is then removed and 2 mm thick coronal sections are prepared. The middle sections are used for 2,3,5-triphenyltetrazolium chloride (TTC) staining and determination of infarction volume.

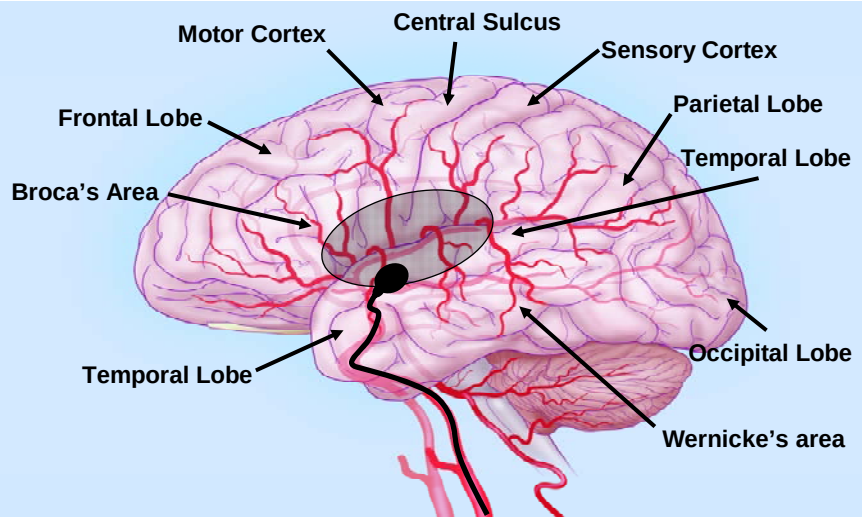

Figure 8: Ischemic occlusion of middle cerebral artery. The filament that is progressed into the MCA causes an ischemic penumbra to form. This penumbra grows over time until the filament is removed allowing reperfusion into tissue.

2.2 Optical micro-angiography (OMAG)

Optical micro-angiography setup used is shown below in Figure 9. OMAG is based on fiber Optical Coherence Tomography (OCT) systems. The incident light is split between a sample and reference arm. The signal returning from the two arms creates a coherence spectrum which is captured by a CCD camera. The spectrum then has a Fast Fourier transform performed on it which can then be processed into the image. More detailed explanation is given in chapter 3 & 4.

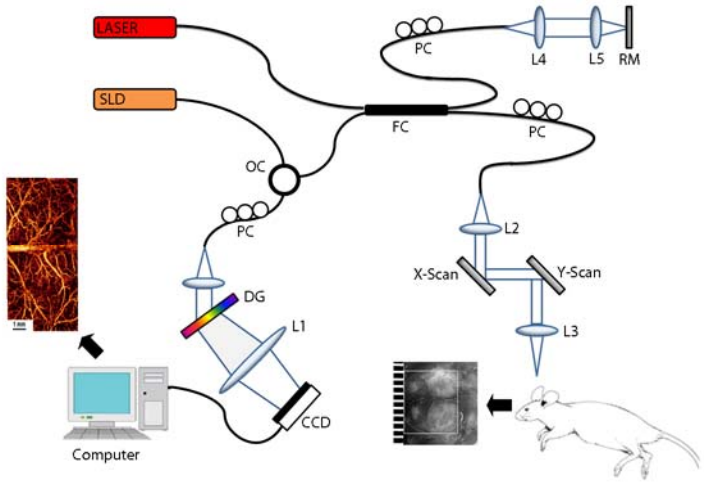

Figure 9: Optical microangiography setup.

The animals' heads are shaved 24 hours before imaging. For OMAG experiments, animals are placed in a stereotaxic stage while under sedation using 1-2% isoflurane via face-mask in O_2-enriched air (Figure 10). A 2 cm incision is made along sagital suture and each side of skin is pulled back using hemostats to expose the skull. Original cranial incision will be opened for all OMAG scans. OMAG is performed before MCAO, during the 60 minute occlusion, and for 50 minutes of reperfusion. The skull is kept hydrated and temperature is monitored and maintained at 37 °C. Animal is euthanized as explained in above section. Figure 11 is a picture of the full OMAG set-up being used to assess the effect of tPA on a mouse undergoing MCAO.

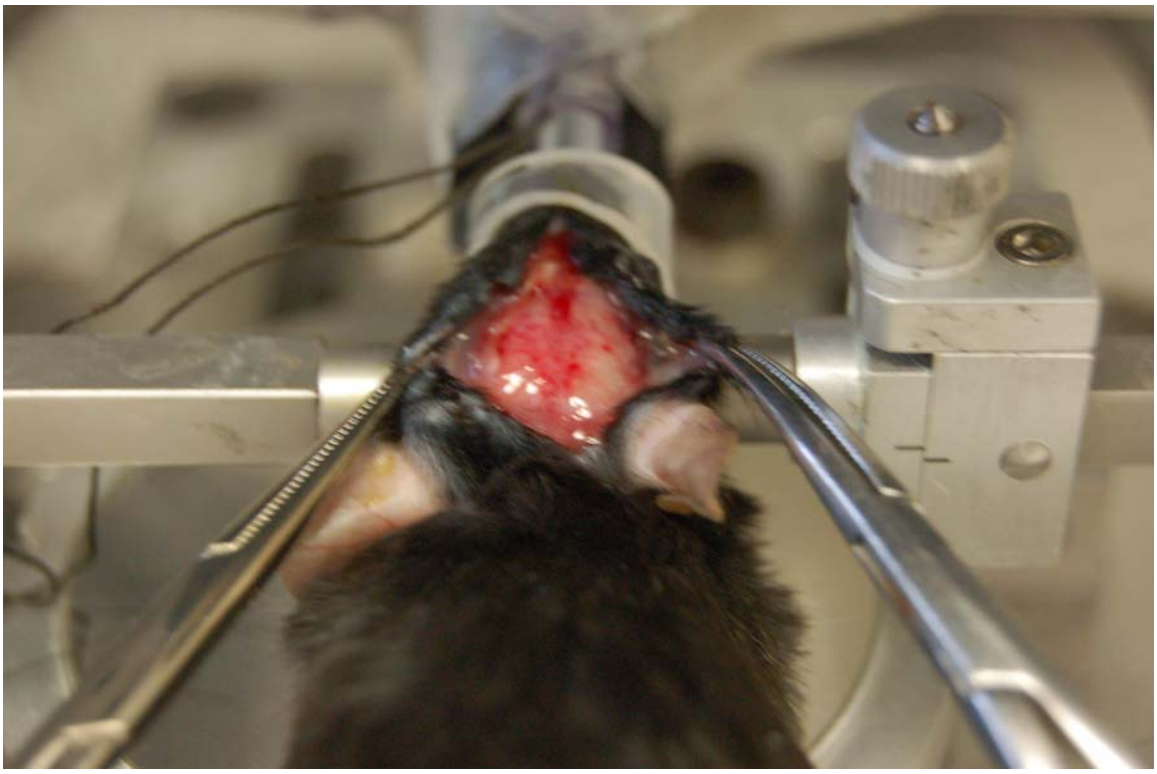

Figure 10: Custom stereotaxic stage stablizes mouse during OMAG imaging. This animals has an occlusion in right hemisphere MCA. The right side is undergoing an ischemic injury and is pale in comparison to the left side.

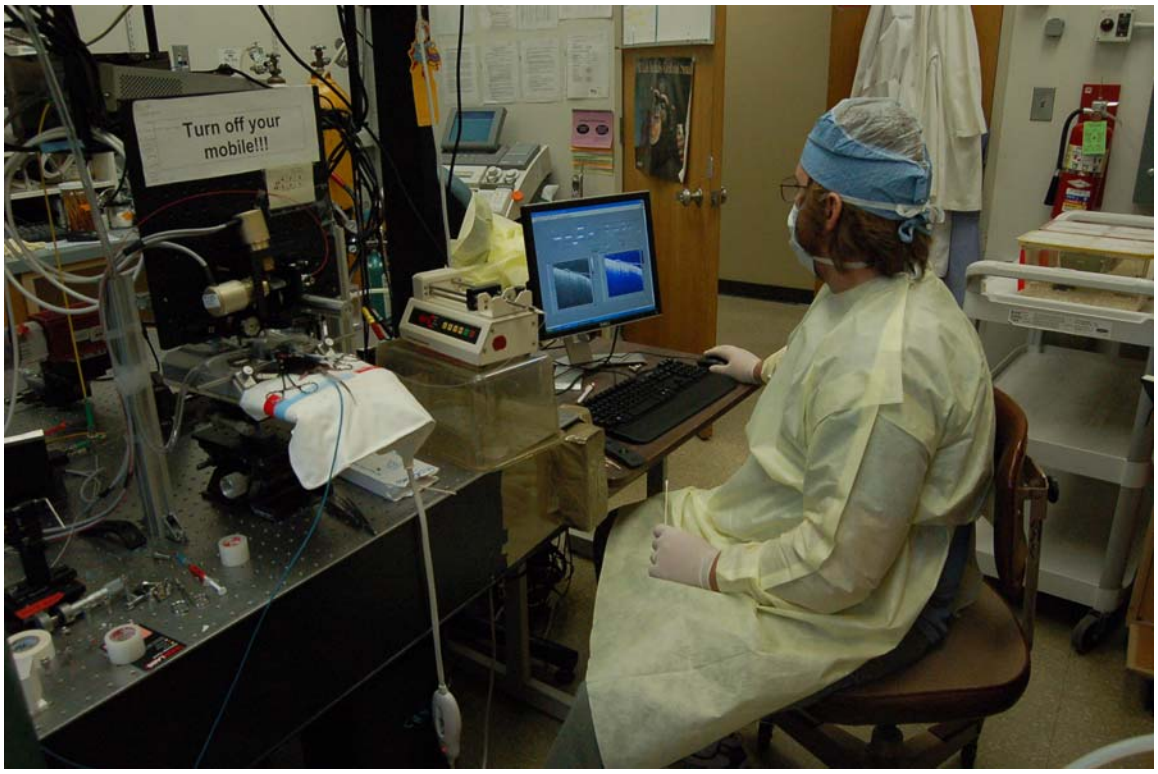

Figure 11: Experiment in progress

Chapter 3: Development of a three dimensional optical angiography system

3.1 Abstract

With existing optical imaging techniques three-dimensional (3-D) mapping of microvascular perfusion within tissue beds is severely limited by the efficient scattering and absorption of light by tissue. To overcome these limitations we have developed a method of optical angiography (OMAG) that can generate 3-D angiograms within millimeter tissue depths by analyzing the intrinsic optical scattering signal from an illuminated sample. The technique effectively separates the moving and static scattering elements within tissue to achieve high resolution images of blood flow, mapped into the 3-D optically sectioned tissue beds, at speeds that allow for perfusion assessment *in vivo*. We used OMAG to visualize the cerebral microcirculation, of adult living mice through the intact cranium, measurements which would be difficult, if not impossible, with other optical imaging techniques.

3.2 Introduction

Optical coherence tomography (OCT) (15, 16) is an emerging, non-invasive, three-dimensional (3-D) imaging technique, capable of optical ranging within a highly scattering sample, such as biological tissue, with visualization of microstructures at a resolution approaching that of conventional histology. The technique, based on the optical scattering properties of tissue, is feasible because most biological tissues have a sufficient number of complex microscopic scattering elements to produce good contrast for OCT images. Time-domain OCT (TDOCT) was the first version of OCT described in the early 1990s (17). As a result of improvements in the light source, the interferometer design, and the beam delivery systems, TDOCT is now being widely used to characterize tissue microstructures both in clinical studies and basic research laboratories (18-20). It

Wang, R. K., Jacques S. L., Ma, Z., Hurst, S., Hanson, S. R., Gruber, A. (2007). "Three dimensional optical angiography." Opt Express **15**(7): 4083-97.
All figures in Chapter 3 were created with the help of Dr. R.K. Wang.

was later recognized that OCT imaging could be performed in the frequency domain (FD) without the requirement to scan the optical delays to perform the ranging as in TDOCT (21), thus allowed for faster imaging. Importantly, the detection sensitivity and phase stability are also improved significantly (22). Such features are critical for the investigation of dynamic biological systems where the speed of data acquisition is vital. Over the past decade, particularly after the discovery of FDOCT, different modes of operation have emerged that enable the visualization and quantification of different tissue parameters *in vivo*, for example blood flow (23-25), birefringence (26), metabolic status (27), and elastic properties (28, 29), among others.

This chapter reports the development of three dimensional optical angiography (OMAG) that exploits the mathematical properties of Hilbert and Fourier transformations of real-valued interferometric signals for interpreting the light scattering properties of tissue. Specifically, we discuss the application of OMAG for the non-invasive, high resolution, and high sensitivity mapping of blood flow within thick tissue layers *in vivo*.

3.3 OMAG System setup

Figure 12 show the schematic diagram of the system used in this study to perform *in vivo* optical angiography. It is based on the Michelson optical interferometer and similar to an optical fiber based frequency domain optical coherence tomography (FDOCT) system previously reported (30). The system used a superluminescent diode with a central wavelength of 842 nm and FWHM bandwidth of 45 nm that yields a measured axial resolution of ~8 μm in air. After passing through an isolator (not shown in the Figure), the light was coupled into a fiber-based Michelson interferometer where the 2x2 fiber coupler acts as a beam splitter. The reference light was delivered onto a reference mirror that was either stationary or mounted on a piezo-translation stage driven by a 10 Hz saw tooth waveform with amplitude of 50 μm. The sample light was coupled into a probe, consisting of a pair of X-Y galvanometer scanners and the optics to deliver the

probing light onto and collect the light backscattered from the sample. The lateral imaging resolution was approximately 16μm determined by the objective lens that focused the sample light onto sample. The light power shone onto the sample was ~1 mW. The light returning from the reference and sample arms was recombined and sent to a custom built high speed spectrometer, consisting of a 30mm focal length collimator, a 1200 lines/mm diffracting grating and an achromatic focusing lens with 150 mm focal length. The focused light spectrum was captured in parallel by a line scan charge coupled device (CCD) (Basler Vision Tech. Germany) consisting of 2048 pixels, each with 10X10 microns in size and 10 bits in digital depth, and capable of 29.2 kHz line rate. Polarization controllers were used in the reference, sampling and detection arms in order to maximize the spectral interference fringe contrast at the detector. The spectrometer has a designed spectral resolution of 0.055 nm, resulting in an optical ranging of approximately 6.4 mm in air, i.e. the full depth in the Fourier space, (z axis shown in the Figure 12), where the positive frequency space (3.2 mm) was used for micro-structural imaging and the negative frequency space (3.2 mm) for flow imaging. The signal sensitivity of 95 dB was measured at $z=+0.5\ mm$ and dropped to 80 dB at $z=+2.0\ mm$ when the camera integration time was set at 34.1 μs.

The probe beam was scanned in the lateral direction (x axis shown in Figure 12) by the X-scanner, driven by a 10 Hz saw-tooth waveform with an amplitude equivalent to 2.2 mm. The Y-scanner, driven at 0.02 Hz with amplitude of also 2.2 mm scanned the probe beam in the elevational direction (y axis). The camera integration time was set at 99 μs for imaging, allowing 1 μs for downloading the spectral data from CCD (2048 pixels, A scan) to the host computer via CameraLink™ and a high-speed frame grabber board (PCI 1428, National Instruments, USA). In the x direction, there were 1000 discrete points measured that makes up a data matrix of 1000 by 2048 elements (slice, B scan). In the y direction, there were 500 discrete points over 2.2mm. Thus, a final volume data cube of 1000 by 500 by2048 (x-y-z) voxels was built from which the 3-

dimensional structural and flow images, each with 1000 by 500 by 1024 voxels (C scan), were computed (see Section 3.4 below). It took 50 seconds to obtain such volume data cube using the current setup. The actions for probe scanning, piezo-stage translation (if needed), data acquisition, data storage and hand-shaking between them were controlled by a custom software package written in Labview® language.

The key difference between OMAG and FDOCT is that the spectral interferogram in OMAG is modulated by a constant Doppler frequency that makes it feasible to separate the moving and static scattering components within sample. In the current setup, we used two methods to introduce the Doppler frequency (i.e. modulation frequency) in the spectral interferogram: 1) the reference mirror in the reference arm was mounted onto a linear Piezo-translation stage (Figure 12) that moved the mirror at a constant velocity across the B scan (i.e. x direction scan), and 2) the scanning probe in Figure 12 was designed such that the probe-beam passes the X-scanner at a certain distance away from the rotating point. In both the cases, the modulation frequency introduced in the spectral interferograms was 1.25 kHz with the CCD line rate set at 10 kHz, and they achieved almost the same OMAG results. Because the introduced modulation frequency is one eighth of the data acquisition rate, the phenomenon on the spectral interference fringe washout at the CCD camera can be neglected. The other methods to introduce this Doppler frequency modulation are straightforward, for example by means of phase modulator placed in either the reference or sample arms, or both.

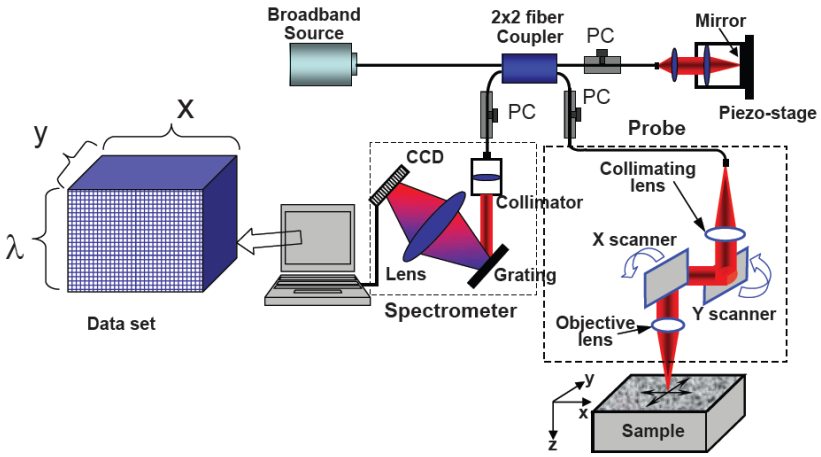

Figure 12: Schematic of the OMAG system used to collect the 3-D spectral interferogram data cube to perform the 3-D angiogram of thick tissue *in vivo*. CCD represents the charge coupled device, PC the polarization controller. Note that the mirror is mounted on the piezo-stage that moves at a constant speed, otherwise it is stationary. The sample was sliced with priority in the lateral direction, x, by raster-scanning the focused beam spot using a pair of X-Y galvanometer scanners to built a 3-D volume data set. During the imaging, the sample surface was adjusted just below the zero delay line to avoid the static image crossing the negative space.

3.4 Mathematical perspectives

Optical interferometry has long been used to detect movements such as red blood cell movements or background tissue movements. The mathematical analysis of the OMAG method essentially maps velocities moving into the tissue away from the surface into one image and velocities moving out of the tissue toward the surface into a second image.

Consider a real function that varies with two variables, both of time coordinates, t_1 and t_2:

$$B(t_1, t_2) = \cos(2\pi f_0 t_1 + 2\pi(f_M - f_D)t_2 + \varphi) \quad (1)$$

where f_0, f_M and f_D are the frequency components, respectively, and ϕ is a random phase term. We assume that there is no correlation between t_1 and t_2, and when t_1 varies t_2 is constant and vice versa. The analytic function of Equation

(1) against t_2 can be constructed through the well known Hilbert transformation if the Bedrosian theorem holds (31) which states that if the modulation frequency $f_M - f_D$ does not overlap the signal bandwidth caused by the random phase fluctuation term ϕ. Under this condition, the Hilbert transform of Equation (1) is equal to its quadrature representation. Bear in mind that the function $B(t_1,t_2)$ is modulated by the frequency $f_M - f_D$, and $2\pi f_0 t_1$ is a constant phase term. Therefore, if $f_M - f_D > 0$, the analytic function of Equation (1) can be written as:

$$\tilde{H}(t_1,t_2) = \cos(2\pi(f_M - f_D)t_2 + 2\pi f_0 t_1 + \phi) + j\sin(2\pi(f_M - f_D)t_2 + 2\pi f_0 t_1 + \phi) \quad (2)$$

where $j = \sqrt{-1}$; whereas if $f_M - f_D < 0$, it is as follows:

$$\tilde{H}(t_1,t_2) = \cos(2\pi(f_M - f_D)t_2 + 2\pi f_0 t_1 + \phi) - j\sin(2\pi(f_M - f_D)t_2 + 2\pi f_0 t_1 + \phi) \quad (3)$$

From the mathematical point of view, Equation (3) is clearly the complex conjugate of Equation (2). Now we perform the Fourier transformation against the time variable t_1 (Note that t_2 is now constant). It is obvious that the frequency component f_0 of Equation (2) is placed in the positive space in the entire Fourier plane, while it sits on the negative space for Equation (3). This is the key element that makes OMAG to image the microvascular flow within tissue.

Consider the case of OMAG (Figure 12), if we assume that the reference mirror mounted on the piezo-stage moves at a velocity $\bar{v}_{ref}$, with the probe beam proceeding in the B-scan (x-scan) at a velocity of v_x (scalar), and we further assume that a reflecting particle that is detected by OMAG also moves but with its directional velocity projecting onto the probe beam direction being $\bar{v}_s$, then for simplicity we can state the spectral interferogram in the wavelength λ domain as:

$$B(1/\lambda, x) = \cos\left(\frac{4\pi(z_s + (\bar{v}_{ref} + \bar{v}_s)\frac{x}{v_x})}{\lambda} + \varphi(x,z,\lambda)\right) \quad (4)$$

Note here that we use vector representations for velocities with the movement towards the incident beam being positive and that opposite being negative. The term z_s is the initial depth-position of the reflecting particle (e.g., the red blood cell) at the lateral position x, and $\vec{v}_s$ is the velocity of that reflecting particle, such that the pathlength difference between sample arm and reference arm is $2(z_s + (\vec{v}_s + \vec{v}_{ref})t_x)$, where $t_x = x/v_x$ is the scanning time of the probe beam in the B scan, and the factor of 2 accounts for the round trip of the sampling light scattered from the sample back into the interferometer. The term $\varphi(x, z, \lambda)$ is a random phase function that relates to the phases of the optical heterogeneous sample. The time $t_x = 0$ would be the start of a B scan. Hence, B(1/λ,x) is a sinusoidal oscillation function versus x for each $1/\lambda$ value. It is clear that Equation (1) and Equation (4) are identical if the following substitutions are used:

$$f_0 = z_s, \quad t_1 = \frac{2}{\lambda}, \quad f_M = \frac{2\vec{v}_{ref}}{\lambda}, \quad f_D = -\frac{2\vec{v}_s}{\lambda}, \quad t_2 = t_x \qquad (5)$$

Thus, the values of $\vec{v}_{ref}$ and $\vec{v}_s$ determine whether the analytic function of Equation (4) constructed through the Hilbert transformation is turned into Equation (2) or Equation (3). The analytic function is sequentially constructed through the Hilbert transformation to the B-scan along the x-axis at each 1/λ. During the operation, the factor $4\pi z_s/\lambda$ is simply a constant phase since it does not vary with x.

If $\vec{v}_s = 0$, positive velocities (v_{ref}) would modulate the signal with positive frequencies in x-space, and negative v_{ref} with negative frequencies. The Hilbert transformation converts the information of the modulated signal versus x into a complex number $\tilde{H}(1/\lambda, x)$, but now any subsequent Fast Fourier Transform (FFT) towards $2/\lambda$, $\mathrm{FFT}\left\{\tilde{H}(1/\lambda, x)\right\}\Big|_{\frac{2}{\lambda}}$, of the Hilbert-encoded information would map positive

frequency components into the positive-frequency space and map negative frequency components into the negative-frequency space of the FFT result. This is in contrast to simply taking $\left.\mathrm{FFT}\left\{B(1/\lambda, x)\right\}\right|_{\frac{2}{\lambda}}$, which always maps both positive and negative frequencies into both the positive- and negative-frequency spaces of the transform, resulting in only half of the space being useful for imaging.

Now, consider the effect of a moving particle, $v_s \neq 0$. The particle movement will modify the modulation frequency through the velocity mixing, $\vec{v}_{ref} + \vec{v}_s$, similar to the frequency mixing in the signal processing discipline. An opposite movement of the particle, e.g. blood cells, relative to the movement of the reference mirror results in a decrease of the difference in photon pathlength between sample and reference arm and decreases the effective frequency of the modulation. If the value of v_s is sufficiently large, the value $\vec{v}_{ref} + \vec{v}_s$ will change its sign. Consequently, after the operations of Hilbert and Fourier transforms, the corresponding signal due to the particle movement will map into the frequency space opposite to that with $v_s = 0$. However, any small particle movement that is not strong enough to change the sign of the value of $\vec{v}_{ref} + \vec{v}_s$ will still map to the frequency space of when $v_s = 0$. Hence, the signals from the perfused blood cells and the bulk static tissue can be separated in the frequency space of FFT, with the background noise due to small tissue movements rejected in the space that represents the image of blood perfusion.

In the current study, the reference mirror moved away from the beam splitter at 500 μm/s. With such a moving reference mirror, a stationary red blood cell appears to be moving into the tissue away from the surface. Any small movements less than 500 μm/s, such as small background movements and low blood perfusion rate, can modulate this velocity, but the red blood cell still appears to be moving into the tissue. Hence, these red blood cells will map into the first image, which we call the static image. Only red blood cells moving toward the surface in excess of 500 μm/s will exceed the reference mirror

movement and appear to be moving toward the surface. Hence, those red blood cells will map into the second image, which we call the perfusion image.
To image the perfusion into the tissue, the reference mirror needs to be moved toward the beam splitter rather than away from the beam splitter. Otherwise, the method is the same. The choice of 500 μm/s can be varied, such that the threshold for detection of low perfusion velocities can be adjusted. The effect of the moving reference mirror is a frequency modulation that can be achieved in several ways. The moving mirror is one method which is useful for the purpose of explanation.

3.5 Data processing outline

The X-Y scanner in Figure 12 enabled the collection of the 3-D spectral interferogram data set from which the 3-D OMAG image was computed. A typical 3-D data cube in this work consists of 1000 by 500 by 2048 voxels. The data processing was based on the slice (B scan) by slice basis. Each B scan contains 1000 (positions) by 2048 (wavelengths) pixels of the spectral interferogram data. The data processing stages to obtain the final 3-D OMAG image are:

3.5.1 Pre-processing

In this step, all the spectral interferograms in each slice along the x-direction are ensemble-averaged at each wavelength to obtain a reference spectrum, which is then subtracted from each A scans. This operation effectively removes/minimizes autocorrelation, self-cross correlation, and camera noise artifacts presented in the final OMAG images (30) that considerably improves the image quality. The subtracted spectral interferograms are then converted into the equal frequency space by use of the spline interpolation method as usually done in the FDOCT (32). This is because the spectral interferogram data matrix captured by the CCD camera are functions of wavelength, however the Fourier transform relationship is between time (distance) and frequency (wavenumber).

3.5.2 Hilbert and Fourier transformations

This is the essential step to obtain the final OMAG images. The pre-processed spectral data matrix is Hilbert-transformed row by row to form the discrete analytic functions, i.e. operation is done for each wavenumber along the positions separately. This Hilbert-transformed data matrix was then Fourier transformed column by column (i.e. performed at each position along the wavenumbers) to convert the data matrix from the spectral domain into the time domain that results in the positive and negative time-coordinates in the output separated by the zero-phase delay line. The resulted data matrix is then multiplied by the speed of light in the sample to give the distance information. The speed of light in the sample is taken as the speed of light in the vacuum ($2.99*10^8$m/s) divided by the refractive index of typical biological tissue which is approximately 1.4 (33, 34).

The data matrix is then split along the zero delay line into two equal parts. The positive part gives the microstructure information of the sample that is essentially the same as that of the conventional OCT image. The negative part gives only the signals pertinent to the moving particles within sample, such as the moving blood cells in the blood vessel, which is flipped to coincide with the microstructural image obtained in the positive part. Both images are of 1000 by 1024 pixels.

3.5.3 Loop

Return to a) to process the next slice until the last slice was completed in the 3-D data cube. Finally, two volume images are obtained, both of which are of 1000 by 500 by 1024 voxels.

3.5.4 Fusion (optional)

This step performs the data fusion to fuse the microstructural image and flow image into a single image to give us a better view on how the blood flow in

vessels is orientated in the tissue. The flow signal is normally coded with a color while the structural image coded with the grey scale.

Due to the computer memory limitations, the volume image was cropped to remove the bottom portion of the volume that does not contain useful imaging information, and then re-sampled and scaled down to 500x500x400 voxels, equivalent to a physical volume dimension of 2.2 by 2.2 by 1.7 mm^3. The 3-D image was log-compressed and displayed as grayscale (color if necessary) coded over 50 decibels (dB) where the minimum was set at 25 dB and the maximum at 75 dB.

For processing of the images presented in this work, the above algorithm was implemented in Matlab 7, running on a 1.8 GHz Windows XP based personal computer. The total processing time required to produce the final 3-D OMAG image shown in Figure 14 was ~ 35 minutes. However, the processing time can be shortened considerably if the algorithm was implemented in an optimized, compiled computer language and run on a more powerful computer. The 3-D data representations and movie making from the final OMAG data set obtained from the above algorithm that are presented in this work were rendered by separate Amira 3-D visualization software (Mercury Computer System, Inc., San Diego, USA).

3.6 *In vivo* Testing of OMAG

For demonstrating the potential of OMAG in the non-invasive assessment of microvascular blood flow, we obtained transcranial images of the cerebrovascular circulation in mice. The experimental protocol was in compliance with the Federal guidelines for care and handling of small rodents and approved by the Institutional Animal Care and Use Committee. Three-month-old male C57BL/6J mice were purchased from commercial breeders (Charles River Laboratories) and kept in our rodent colony until use. The mice, each weighing 23 to 28 g, were prepared for OMAG one day before the experiments by shaving

the heads followed by a depilatory cream to remove all remaining hair from the top of the skull. Anesthesia was induced by subcutaneous injection of a "Rodent cocktail" containing ketamine hydrochloride (30 mg/kg), xylazine hydrochloride (2 mg/kg) and acepromazine (1 mg/kg) in 100 µL total volume. Anesthesia was maintained by half of the induction dose, typically administered 45 to 60 min after induction. The right common carotid artery (CCA) was exposed, a loose 6-0 silk suture loop was placed around the vessel, and the edges of the wound were pulled together with both ends of the suture hanging out approximately 15 cm. The animal was then transferred to a custom stereotaxic imaging stage, positioned on its ventral side, and the head was secured with a tape to minimize its movement due to breathing. An incision of ~10 mm was made along the sagital suture; the skin was pulled to the sides exposing the frontal, parietal and intraparietal bones. The exposed skull bones were washed with saline, and a drop of mineral oil was used to keep the window hydrated. The animal was then positioned under the OMAG scanning probe as described in Section 3.3. Following the first full surface scan, the right CCA was narrowed by tightening the loose suture, and a second scan was performed to determine whether the cortical blood flow pattern was affected by the temporary stenosis. The animal was sacrificed and photographs of the scanned surface were obtained. The bone and meninges were then carefully removed, and the cerebral cortex was photographed for matching the visible superficial vessels with the OMAG images.

The experiments performed in this study confirmed that OMAG can evaluate transcranial blood perfusion at the capillary level of resolution. The cortical blood perfusion in mice was reproducibly visualized over several days with the cranium intact. In the current OMAG system (Figure 12), a near-infrared broadband light centered at 842nm was used to progressively slice the mouse brain with the skull intact so that a 3-D raw spectral interferogram dataset is collected.

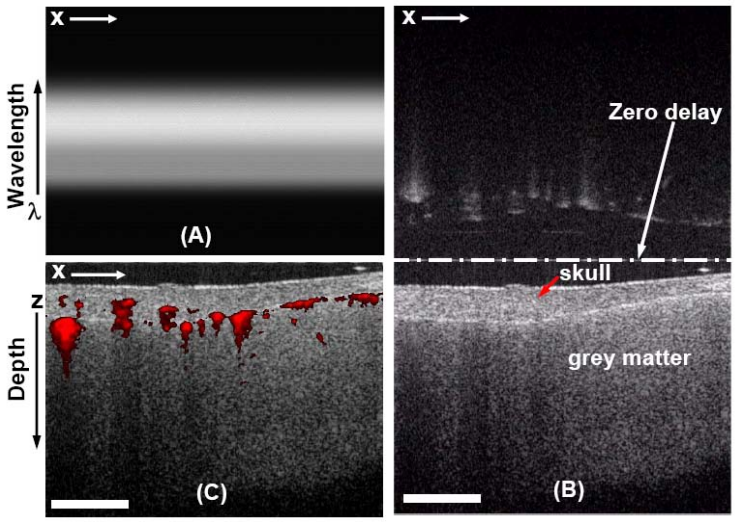

Figure 13: A cross-section (slice) of an adult mouse brain with the skull intact was imaged with OMAG *in vivo*. (A) The data set representing the slice contains 2-D real-valued spectral interferogram in x-λ2.2 mm by 112 nm centered at 842nm). **(B)** The imaging result obtained from (A) by OMAG. It is separated by the zero delay line into two equal spaces. The normal OCT image is located in the bottom region (2.2 by 1.7 mm) showing microstructures. The signals from the moving blood cells are located in the upper region (also 2.2 by 1.7 mm). (C) Folded and fused final OMAG image (2.2 by 1.7 mm) of the slice showing the location of moving blood (red color) within the cortex and mininges where there are more blood vessels than in the skull bone. A threshold above the noise floor of 15 decibels (dB) was used in the flow image before the image fusion took place to avoid the background noise. Both (B) and (C) images are displayed after log-compression of the OMAG data to enhance the imaging contrast into the depth due to the fact that the light attenuation into the scattering tissue roughly follows the Beer-Lambert law. The scale bar in (B) and (C) represents 500 μm.

Figure 13B shows the image obtained from the raw spectral interferograms (Figure 13A) representing one slice within the 3-D dataset using OMAG, where the entire Fourier space is separated into two equal regions. The bottom region is the positive frequency space containing the normal OCT cross-sectional image within which the histologically important layers such as cranium and cortex may be clearly demarcated, but it is almost impossible to identify the blood vessels. Because red blood cells flow through all blood vessels, including capillaries, these moving components can be precisely localized in the negative space (upper region, Figure 13B) in OMAG. As the positive and negative spaces are exactly mirrored, they can be folded to fuse a single image to localize with high

precision the blood vessels within the tissue (Figure 13C). Similar to OCT, OMAG is capable of resolving the cortical structures and blood perfusion at depths of ~1.5 mm through the cranium, a penetration depth that can not be achieved with confocal microcopy. This depth, primarily limited by the high scattering properties of the brain, can be extended further if a light having a longer wavelength is used for imaging, as opposed to 842nm used here. The axial resolution for resolving blood vessel dimensions in OMAG is determined by the bandwidth of the light source used; for the configuration shown in Figure 12, it was ~6μm within the biological tissue, which is capable of resolving the capillaries that are of an average size of 10 μm (35). Lateral resolution was ~16μm which is determined by the objective lens that focused the light into the tissue.

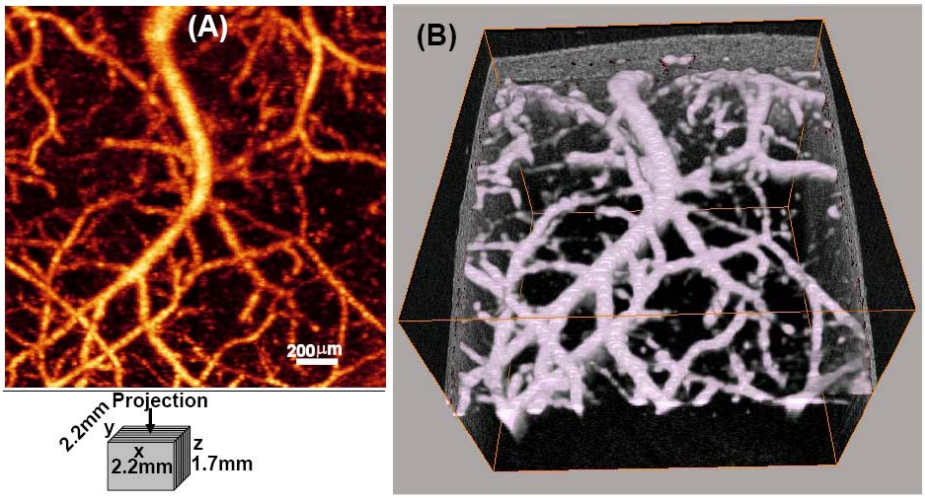

Figure 14: A volume of 2.2x2.2x1.7 mm^3 of an adult mouse brain with the skull intact was imaged with OMAG *in vivo*. The imaging time to obtain this 3-D OMAG image took about 50s using current system setup (Figure 12). **(A)** The 2-D x-y projection view of cerebro-vascular flow within the scanned volume that maps the detailed blood vessel network, including the capillaries. **(B)** Complete 3-D view of the blood flow map merged into the 3-D microstructures available in the positive space of the OMAG output. The 3-D volume rendering of the blood vessel network skeleton is shown to illustrate how the blood vessels are orientated and localized in the 3-D microstructure of tissue. Using suitable software, this 3-D view could be rotated, cut and examined from any angle to illustrate the spatial relationship between the blood flow and tissue microstructures.

3-D OMAG imaging can be performed by evaluating the spectrogram data slice by slice, then re-combining to yield the 3-D volume dataset (x-y-z), from which high quality information regarding vasculature, blood flow and microstructures can be extracted. A detailed 2-D vasculature mapping is obtained by projecting the 3-D flow image available in the negative space into the x-y plane (Figure 14A). Because OMAG also gives the 3-D microstructure of the sample in the positive space, the 3-D localized moving scattering elements in the negative space can be folded to combine with the 3-D structural image to give us a complete view of how the blood vessels are orientated within the tissue (see Figure 14B, and associated videos). In the current configuration of Figure 12, the imaging speed was 10 frames per second; the entire image acquisition time of Figure 14 was ~50s. This imaging time can be dramatically shortened by employing a higher power light source and a higher speed of detection camera. The computation time for post processing of images was ~4.2 s per slice on a personal computer, or about 35 min for a full 3D image. This computational load can be reduced significantly with parallel processing on a more powerful computer.

The detailed cerebro-vascular perfusion that can be visualized in 3-D using OMAG, combined with the quantification of blood flow within individual blood vessels and tissue volumes, holds considerable appeal for the investigation of neurological diseases in small animal models. For example, ischemic thrombotic stroke is widely studied in small animal models such as the genetically altered mouse. Thus a detailed view of cerebro-vascular blood flow phenomena and its regulation across the entire cerebral cortex – at the level of individual blood vessels down to the capillary – will be important to better understand the pathophysiology of cerebrovascular diseases and the potential benefits of pharmacological interventions. To document that OMAG can serve as a tool in the study of cerebro-vascular blood flow, multiple 3-D images of the mice brain

were collected over different regions of the skull. Images from different regions of brain were then combined as a mosaic.

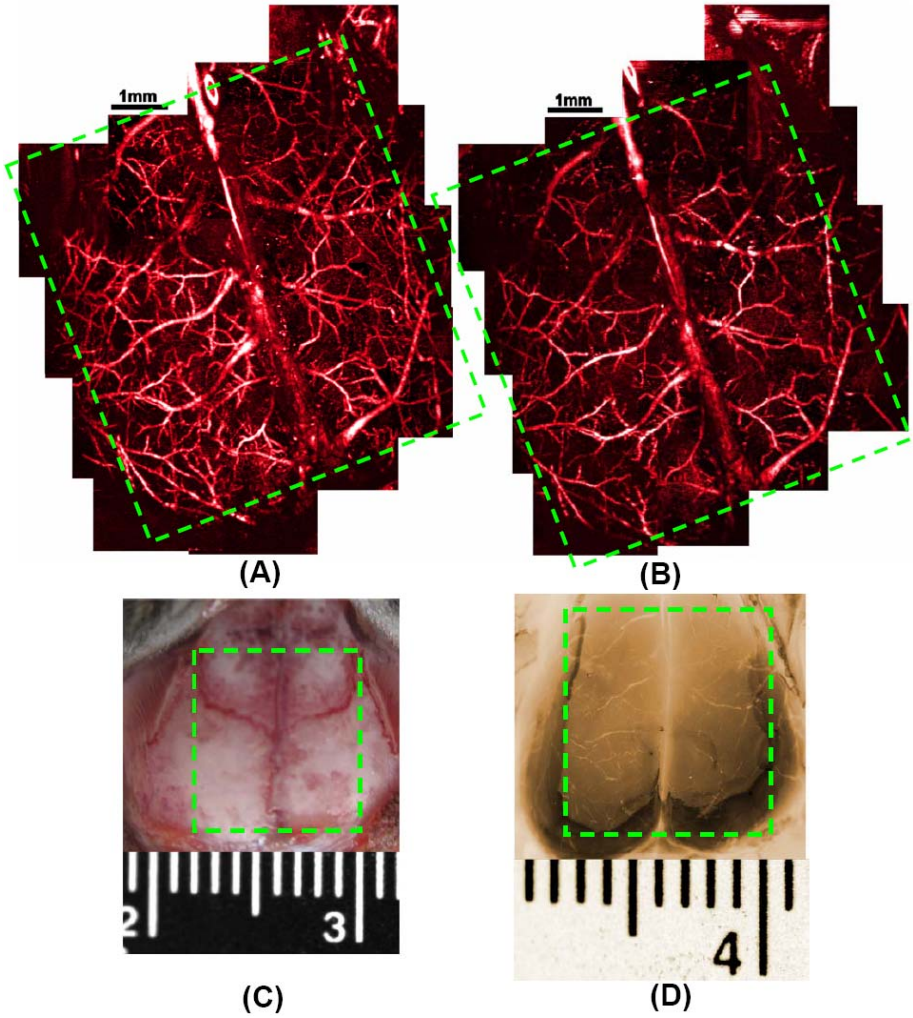

Figure 15: The entire cerebro-vascular flow over the cortex of an adult mouse with the skull intact was imaged with OMAG *in vivo*. (A) and **(B)** are the projection views of blood perfusion before and after the right carotid artery was blocked. Over the entire cortex, the majority of capillaries showing in (A) underwent undetected in (B), and furthermore, the diameters of the blood-flow-reconstructed vessels apparently became smaller in (B). Both are the indications of the blood flow slowing down in the entire cortex, rather than in the right hemisphere, after blocking the right carotid artery. It took ~13 minutes to acquire the 3-D data to obtain (A) or (B) using the current system setup (Figure 12). The projection image was obtained from OMAG scans of 16 different regions one by one, which were then mosaiced to form (A)/(B). The area marked with dashed green box represents 8 by 10 mm^2. **(C)** Photograph of the skull with the skin folded aside, taken right after the experiments where viewing the vasculatures through the skull is impossible. **(D)** Photograph showing blood vessels over the

cortex after the skull and the meninges of the same mouse were carefully removed. The superficial major blood vessels show excellent correspondence with those in (A) and (B). The contrast of this photograph as a whole was digitally enhanced to better illustrate the blood vessels.

Figure 15A shows the blood flow in the cerebral cortex of a mouse with the skull intact. Occlusion of one carotid artery does not cause cerebral infarction or neurological deficits in the mouse. The image of Figure 15B was taken from the same animal while the right carotid artery was blocked for 5 minutes. It is apparent that the blood flow in the cortex, rather than in the right hemisphere only, is reduced as compared to Figure 15A. This is consistent with the well-known collateral circulation between brain hemispheres leading to a total reduction in cortical blood volume due to the occlusion of one common carotid artery. The capacity of OMAG to achieve such high resolution imaging of the cerebral cortex – within minutes and without the need for dye injections, contrast agents or surgical craniotomy, - makes it an extremely valuable tool for studying the hemodynamics of the brain.

3.7 Comparison between OMAG and phase-resolved Doppler OCT

Over the past few years, phase-resolved Doppler OCT (DOCT) based on the time-domain OCT (25, 36, 37) and later on the Fourier domain OCT (24, 38-41) has been reported to make high-resolution and high-velocity sensitivity imaging of blood flow. Briefly, the technique was developed based on the phase measurement between successive axial (A) scans. If the sample moves by an instantaneous distance Δd during a time interval τ between two successive A-scans, the measured phase changes by an amount of $\Delta\phi = 2n_0\bar{k}\Delta d$ due to the well-known Doppler effect, where n_0 is the average refractive index of the sample and $\bar{k}$ is the average wavenumber of the light source used. This phase change is related to the Doppler frequency by $f_D = \Delta\phi(2\pi\tau)^{-1}$. Evaluating $\Delta\phi$ at each depth *z* yields depth-resolved measurements of both the magnitude and direction of the flow velocity under the assumption that this change is solely caused by the moving scatterers within the sample. Assuming that the probe beam intersects

the flow velocity vector at an angle β (Doppler angle), the flow velocity is given by $v = \Delta\phi(2n_0\bar{k}\tau\cos\beta)^{-1}$. This method was originally demonstrated in time-domain OCT (25) and later in Fourier-domain OCT (24) and is the method that is commonly used in OCT nowadays to assess the localized blood flow in tissue.

Theoretically, the sensitivity of phase resolved DOCT to measure the blood flow is in the order of micrometers per second, largely limited by the OCT system noise floor (40). However, in practical *in vivo* applications, the assumption of the phase change between the adjacent A scans solely caused by the moving scatterers within sample will never be true. This is because 1) DOCT essentially measures the relative motion which represents as the Doppler shift in the light frequency between the light it emits and that it receives. This shift is imparted when the light strikes an object which is moving, relative to the probe. Therefore, the inevitable sample movement will give severe artifacts on the blood flow measurement. 2) The tissue sample is naturally of optical heterogeneity. This optical heterogeneity property of the sample will impose a texture background noise floor on the flow images obtained from the phase-resolved DOCT technique (41). Although practically one can employ dense sampling approach in the lateral direction (B scan), i.e. taking more A scans than it is necessary, to minimize this noise floor. The disadvantage is that it dramatically reduces the imaging speed and also increases the computational load to obtain the meaningful flow images. 3) The phases are mathematically limited to the interval $(-\pi\ \pi]$ corresponding to the principal value of the arctangent function. Theoretically, one can use the phase un-wrapping technique to correct the phases, however it is un-practical to implement this under the *in vivo* situations because of the reasons 1) and 2) above, in addition to that the phases are strongly dependent on the OCT signal strength (40) and the system noise level. Therefore, the phase resolved DOCT images are extremely noisy. Despite of these, *in vivo* mapping of vasculature networks in the retina has been most recently reported based on the phase-resolved DOCT technique (42) by use of sophisticated algorithms to minimize the noise artifacts.

In contrast, OMAG rejects the small scale sample movement and the noise signals originated from the optical heterogeneity of the sample. In fact, small sample movement (<0.5mm/s in our current system setup) will improve the OMAG sensitivity to sense the blood flow in tissue because in this case the blood flow velocity can be smaller to meet the requirement for Equation (3) due to the additional contribution from the sample movement. Note that large scale of sample movement is not rejected in OMAG. In addition, only OMAG flow signals appear in the negative space of the output plane which makes the flow image almost free of artifact-induced noises. Furthermore, the calculations are straightforward and do not involve sophisticated algorithms that considerably reduce the computational effort in obtaining the 3-D angiograms as compared to that using the phase resolved DOCT.

In Figure 16, we illustrate the difference between OMAG and phase-resolved DOCT imaging of blood vessel network over the mouse brain using the same data set. In obtaining the DOCT flow image, we followed the algorithms published in (42) where the algorithms for minimization of the sample motion artifacts, segmentation of regions of interest and correction of phase-wrapping errors were implemented, and then the resulted phase shifts between the adjacent A scans were squared (i.e. power Doppler imaging approach) to obtain the map of vasculatures. From Figure 16, the advantages of OMAG in mapping the detailed vasculature network are apparent. Note also that the computation time required to obtain Figure 16(A) and Figure 16(B) were ~35 min and ~105 min, respectively, running on the same personal computer.

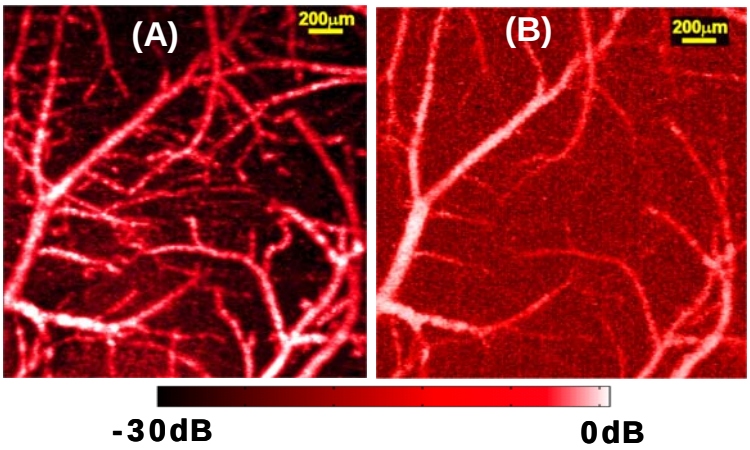

Figure 16: Comparison of blood perfusion projection images obtained from an adult mouse brain with the skull intact *in vivo* by use of (A) OMAG and (B) phase resolved DOCT, respectively. The projection images were obtained from the physical dimension of a volume 2.2x2.2x1.7 mm^3. In obtaining (A) and (B), the pixel values were normalized by the maximum pixel value in each image, and then log compressed to give the images that were displayed using the colorbar shown in the bottom that has a scale of [-30dB 0].

However, the advantage of phase-resolved DOCT is that it could provide us with the magnitude of velocity about the blood flow from the calculated phase shifts with less imaging time and computational efforts. Fortunately, the difference between OMAG and phase-resolved DOCT lies purely in the algorithms. Here, the modulated spectral interferograms during the imaging in OMAG can be easily dealt with in the software. Therefore, although the phase-resolved DOCT is difficult to identify the capillaries in tissue, it can be combined with OMAG to provide the flow velocity in the major blood vessels. Figure 17 gives such an example shown in video format.

It may be worth mentioning that a prior knowledge of the Doppler angle is a prerequisite for DOCT to deduce the true velocity of blood flow. However, the unknown 3-D geometrical orientation of the blood vessel relative to the incident probe beam direction poses a significant difficult problem to know precisely the Doppler angle, and the noise artifacts in the DOCT flow image adds a further difficulty into this problem. Therefore, the true velocity magnitude obtained from the DOCT is in reality a very rough estimate. This calls for the combined use of

OMAG and DOCT if the true velocity of blood flow is critical in the investigations because OMAG provides more accurate 3-D blood vessel orientations, leading to a more accurate estimation of the Doppler angle.

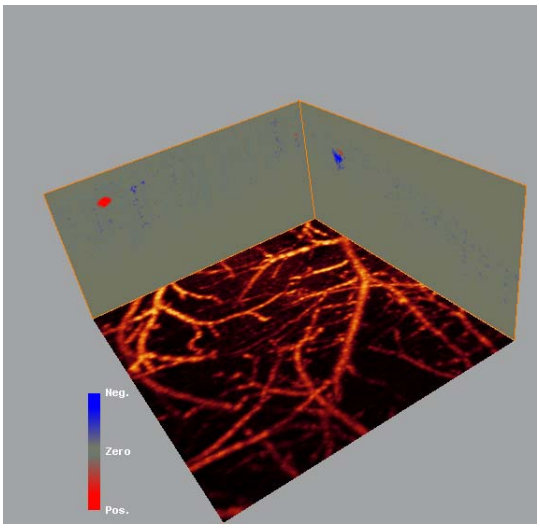

Figure 17: 3-D rendered image showing that the OMAG and Doppler OCT can be combined to quantify the blood flow within individual blood vessels shown in Figure 16. In this particular image, the projection of OMAG flow image is given at the bottom of the frames, and the result from DOCT is updated frame by frame. The color bar represents -2.1mm/s (blue) to 2.1mm/s (red). The velocities calculated are the projections of true velocity vectors onto the incident beam direction (which was shone from the top into sample).

3.8 Summary

We have presented an optical angiography technique capable of high resolution imaging of blood perfusion within localized blood vessel embedded within highly scattering tissue. By exploiting the inherent properties of the OMAG signals, the moving and static scattering elements within tissue can be efficiently separated, thereby enabling precise localization of blood perfusion in 3-dimensional microstructures. The use of contrast agents and newer imaging agents administered into blood, for example nanoparticles and microbubbles (43), might enhance even more the light backscattered from the moving elements, thus enhancing further the sensitivity of 3-D OGA. The system is compact, fast, optically stable, and easily implemented in both the hospital and research laboratory environments.

Although the present report demonstrates the usefulness of OMAG in transcranial cerebrovascular imaging in mice models, it is also well suited for performing 3-D angiograms on thick tissues in other basic and clinical settings, where the visualization and quantification the microcirculation are important for understanding mechanisms and treatments, e.g. tumor angiogenesis, wound healing. Other examples of prospective applications include neuroscience, where changes in cortical blood flow are coupled to certain types of neuropathology, such as dementia; ophthalmology, where ocular and retinal circulatory beds are very important in the diagnosis and management of disorders such as glaucoma, diabetic retinophathy and age-related macular degeneration. As OMAG and the associated computation are developed into a rapid imaging system, we will be able to assess tissue perfusion at the resolution level of capillary flow in real time without interfering with the sample in a significant way.

Chapter 4: Mapping of cortical blood perfusion in mice with skin and skull intact by optical microangiography at 1.3μm wavelength.

4.1 Abstract

Optical micro-angiography (OMAG) was developed to achieve volumetric imaging of the microstructures and dynamic cerebrovascular blood perfusion in mice with capillary level resolution and high signal-to-background ratio. In this paper, we present a high-speed and high-sensitivity OMAG imaging system by using an InGaAs line scan camera and broadband light source at 1.3 μm wavelength for enhanced imaging depth in tissue. We show that high quality imaging of cerebrovascular blood perfusion down to capillary level resolution with the intact skin and cranium are obtained *in vivo* with OMAG, without the interference from the blood perfusion in the overlaying skin. The results demonstrate the potential of 1.3μm OMAG for high-speed and high-sensitivity imaging of blood perfusion in human and small animal studies.

4.2 Introduction

The ability to accurately visualize micro-vascular networks under normal and diseased conditions is critical for evaluating the emerging therapeutic strategies, such as in the development of potential drugs to support or limit neovascular growth (44). Another example is in the treatment and diagnosis of neural vascular diseases where the cerebral blood perfusion is related to the normal and pathophysiologic conditions of brain metabolism (45, 46). Technical constraints currently limit most microvascular imaging to two dimensions, however three-dimensional (3D) visualization of vascular image data is often required in order to reveal the detailed architecture of the microvascular network so that the volumetric rheology and perfusion status of the tissue can be

Wang, R. K. and S. Hurst (2007). "Mapping of cerebro-vascular blood perfusion in mice with skin and skull intact by Optical Micro-AngioGraphy at 1.3 μm wavelength." Opt Express **15**(18): 11402-12.
All figures in Chapter 3 were created with the help of Dr. R.K. Wang

quantified (47, 48).

Numerous techniques have been applied to image the cerebral blood flow (CBF) and volume changes. Conventional X-ray carotid angiography is an excellent clinical tool; however, it is invasive and not suitable for small animal studies. Although autoradiographic methods provide endpoint 3D spatial information, they contain no information about the dynamic CBF evolution (49). Methods based on magnetic resonance imaging (50) and positron emission tomography (51) provide spatial maps of CBF but are limited in their temporal and spatial resolution. Optical intrinsic signal imaging (52) laser speckle imaging (53) and laser-Doppler flowmetry techniques (54) have the desired high spatial resolution, but are limited to two-dimensional mapping of CBF and require surgical opening or substantial thinning of the cranium during the study. Photoacoustic imaging, based on thermal-acoustic phenomena resulting from the strong light absorption of blood and the subsequent thermo-elastic expansion, has recently been reported to map vascular structures deep within the brain of small animals (55, 56). However, the spatial (~100 μm) resolution of this approach is limited by the viscoelastic filtering of higher acoustic frequencies by the tissue. Moreover, blood flow information is not forthcoming with this method. Confocal microscopy, a widely used technique that is capable of ultrahigh resolution mapping of the cerebrovasculature (35) also requires the removal of intervening bone due to its limited imaging depth (up to 300 μm) and the use of injected fluorescent tissue markers.

Optical micro-angiography (OMAG) (57) is a recently developed imaging method, capable of resolving 3D distribution of dynamic blood perfusion at the capillary level within microcirculatory beds *in vivo*. The imaging contrast of blood perfusion is based on the endogenous light scattering from the moving blood cells within biological tissue; thus no exogenous contrasting agents are necessary. This is achieved by efficient separation of the moving scattering elements from the static scattering ones within tissue through the OMAG hardware associated with

mathematical analysis of the optical scattering signals from an illuminated sample. Its development has its origin in the Fourier domain optical coherence tomography (FDOCT) (58) OMAG improves over previous methods, e.g. FDOCT and Doppler OCT (23, 41, 59, 60) by introducing a constant frequency modulation f_M into the time-varying spectral interferograms at the time when the probing beam is scanned over the sample. The introduction of f_M in the interferograms was achieved by linear translation of the reference mirror in the interferometer, synchronized with the OCT cross-sectional (B scan) imaging. This makes it possible to separate the light scattering signals backscattered from the moving particles, such as moving blood cells, from those backscattered from the static particles, such as bulk tissue, leading to high resolution mapping of dynamic blood perfusion down to capillary levels within thick tissue sample *in vivo*. In essence, the OMAG method maps the scattering signals from the moving particles into one image, i.e. flow image, and from the static particles into a second image, i.e. microstructural image. The previous reported OMAG system used light source centered at ~840nm that has shown capable of imaging cerebro-vascular blood perfusion in mice with the cranium intact (57). It would be desirable that the cerebro-vascular blood perfusion can be accessed without removal of the overlaying skin so that the possible complications of dynamic blood flow due to surgical interventions can be minimized.

Because it is a variation of FDOCT method, OMAG has almost the same advantages and disadvantages as those possessed by FDOCT. In the development of FDOCT, one of the efforts is to improve the several system characteristics for *in vivo* imaging applications, these including imaging resolution, signal-to-noise ratio, and imaging depth. These parameters are strongly dependent on the light source characteristics, especially on its emission wavelength. As the optical properties of biological tissue, for example absorption and scattering, have strong relation with the optical frequency (wavelength), OCT/OMAG imaging depth and contrast are no doubt dependent on the emission wavelength of the illuminating light source used. Previous investigations in the

development of OCT have shown that, for a highly scattering biological tissue, enhanced imaging depth for light source centered at ~1300nm wavelength can be resulted when compared to that centered at ~820nm (61-63). This conclusion therefore also holds for OMAG imaging modality.

In this chapter, we demonstrate a high-speed, high sensitivity OMAG imaging system operating at a central wavelength of 1.3 μm for maximum imaging depth in tissue. By using an InGaAs line scan camera as the detecting component in the spectrometer, we have obtained high quality *in vivo* OMAG images of cerebro-vascular blood perfusion in mice with the skin and skull intact. To the best of our knowledge, since the development of OCT, this is the first time that trans-dermal and trans-cranial cerebral blood perfusion can be imaged in 3D at the capillary level resolution.

4.3 OMAG system setup

A schematic of the OMAG system operating at 1.3 μm is shown in Figure 18. Because OMAG has its origin in Fourier domain OCT, the system layout is similar to that of 1.3 μm spectral domain OCT (64, 65) and our previous OMAG system operating at 840nm (57). The light source is a broadband, superluminescent diode (SLD) with full-width-half-maximum (FWHM) of 48nm centered at 1.3 μm (Denselight, Singapore). The total output power was 10mW. This light source yielded a measured axial resolution of 15 μm in air. The light was coupled into the spectral domain fiber-based Michelson interferometer via a broadband optical circulator (Newport, USA). The sample light was delivered to a sample-arm imaging probe that was focused into the sample by an objective lens (f=50mm) with a focal spot of ~20 μm. In order to perform 3D imaging of tissue sample *in vivo*, an X-Y galvanometer scanner (GSI Lumonics, USA) with a scanning priority in X direction was used to scan the focused beam spot over the sample. The X-scanner was driven by 10Hz saw tooth waveform to provide transverse scanning over 2.5mm (B scan) at the sample, while the Y-scanner was driven by 0.02Hz saw tooth waveform that provided the beam scanning in

the elevational direction of also 2.5mm. The reference arm of the interferometer had an adjustable delay reference-mirror and dispersion was matched between the sample and reference arms by use of optical materials with different thickness. The reference mirror was mounted onto a piezo-translation stage (Physik Instrument, Germany) that was also driven by a saw tooth waveform with an amplitude equivalent to the maximum reference delay of 40 μm. This saw tooth waveform was synchronized with that used to drive the X-scanner and provided a constant modulation frequency of f_M = ~0.62 kHz in the spatial spectral interferograms when the probe beam was scanned over the sample. Thus, the minimum blood flow velocity that can be measured by this system is 0.4 mm/s as determined by the constant velocity of the moving mirror driven by the piezo-translation stage (57). Polarization controllers were used in the reference, sampling and detection arms in order to maximize the spectral interference fringe contrast at the detector. Also, a 633 nm visible light from a laser diode was coupled into the interferometer for ease of the positioning during imaging.

Volumetric imaging data was collected by scanning the probe beam spot using the X-Y scanner. In the x direction, there were 1000 discrete points measured over 2.5 mm that makes up a data matrix of 1000 by 512 elements (slice, B scan). In the y direction, there were 500 discrete points over 2.5mm. Thus, a final volume data cube (spectrograms) of 1000 by 500 by 512 (x-y-z) voxels was built from which the 3-dimensional OMAG structural and flow images were computed. It took 50 seconds to obtain such volume data cube using the current setup.

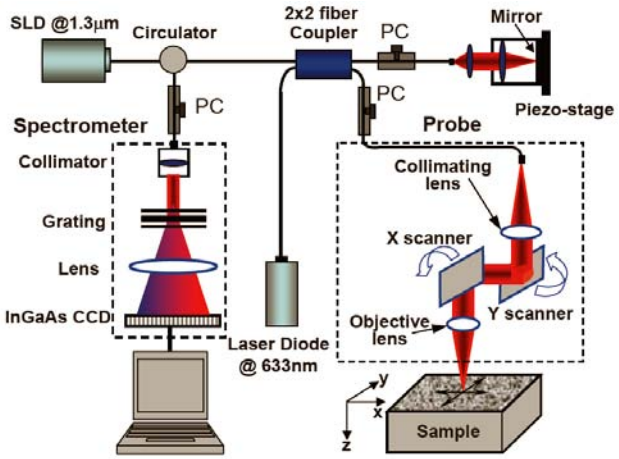

Figure 18: Schematic of the OMAG system operating at 1.3μm where SLD represents the superluminescent diode and PC the polarization controller.

The output of the interferometer was routed into a spectrometer via the optical circulator. The spectrometer consists of an IR achromatic doublet f = 50 mm fiber collimating lens, a 1200 line/mm volume phase holographic grating (Wasatch Photonics, USA) with 80% efficiency, and an f = 190 mm lens that images the spectral interference onto a 512 element infrared InGaAs linescan camera (Sensors Ltd. USA). The optical efficiency of the spectrometer defined as the power incident on the camera detector array divided by the power in the fiber is approximately 78%. The camera has a 14-bit resolution with a maximum line scan rate of 20.5 kHz. The camera integration time was set at 60 μs for imaging, allowing 40 μs to download the spectral data from camera (512 pixels, A scan) to the host computer (Pentium IV, 3.2 GHz, 2 GB RAM) via CameraLink™ and a high-speed frame grabber board (PCI 1428, National Instruments, USA). This means that the camera line scan rate was 10 kHz for the current study. According to the sampling theorem, the maximum speed of blood flow in the direction of incident beam that can be detected by this system setup is 3.25mm/s, equivalent to the Doppler frequency of ±5 kHz. The spectrometer was calibrated over the measured bandwidth by comparing the spectrum registered by the InGaAs camera with a commercial optical spectrum analyzer (Anritsu MS971013B, Japan). The spectrometer had a designed spectral resolution of 0.159 nm. Because OMAG is an *in vivo* full range complex imaging technique (66) this spectral resolution results in an optical ranging of approximately 5.8 mm in air, i.e. the full depth in the Fourier space, (z axis shown in the Figure 18), where the positive frequency space (2.9 mm) was used for micro-structural imaging and the negative frequency space (2.9 mm) for flow imaging. The signal sensitivity of 105 dB was measured at *z=+0.3 mm* and dropped to 95 dB at *z=+2.5 mm* when the camera integration time was set at 60 μs. During the imaging, the actions for probe scanning, piezo-stage translation, data acquisition, data storage and hand-shaking between them were controlled by a custom software package written in Labview® language.

In order to enhance the final OMAG image quality, data-preprocessing was necessary on the raw volumetric spectrogram data set. First, all the spectral interferograms in each slice along the x-direction were ensemble-averaged at each wavelength to obtain a reference spectrum, which was then subtracted from each A scans. This operation effectively removes/minimizes autocorrelation, self-cross correlation, and camera noise artifacts presented in the final OMAG images (30) that considerably improves the image quality. The subtracted spectral interferograms are then converted into the equal frequency space by use of the spline interpolation method as usually done in the FDOCT. Note that before the operation of wavelength to frequency conversion, the spectral data of 512 pixels in each A scan was re-sampled into 1024 pixels by padding with zeros using the Fourier transformation method (67) so that the OCT signal fidelity is improved. Finally, the OMAG algorithm was applied to the pre-processed data set to compute the structural and flow images, i.e. Hilbert (x direction) and Fourier (frequency direction) transformations were performed in tandem (57). Final OMAG structural and flow images were of the dimension of 1000 by 500 by 512 voxels (C scan), respectively. After scaling with an average refractive index of 1.4 for typical biological tissues (68) the C scan represented a physical volume dimension of 2.5x2.5x2.0 mm^3 (x-y-z).

4.4 Results

4.4.1 Performance assessment

To assess the imaging performances afforded by OMAG, we conducted a series of experiments. First, we used a homogeneous scattering phantom, an opaque granular plastic, to evaluate the background noise level. It is important because this metric directly relates to our ability to extract the useful signals from the noisy background. In order to test how the different A scan sampling density affects the OMAG results, we imaged the phantom with A-scan spatial sampling over B-scan (2.5mm) being 1000 and 2000 points, corresponding to 2.5 μm and 1.25 μm separation distance between adjacent A-scans, respectively. The results are shown in Figure 19 where (A) is the conventional OCT/OMAG image

available from the OMAG structural space, while (B) gives the result from the OMAG flow space. There is no visible improvement in the noise floor of the flow image when the A scan sampling density is dramatically increased (from 1000 to 2000 A scans over 2.5mm B scan in this case). To more clearly visualize this, Figure 19(C) plots the noise floor level in the OMAG flow space, calculated as the ensemble average of the OMAG flow signal, from the images of Figure 19(B) as functions of depth in the phantom. Because the system sensitivity falls off over the depth due to the finite size of the detector in the camera, and also OCT/OMAG structural signal magnitude decays approximately exponentially along depth, the dependence of noise level on signal magnitude are also given in the plot, which is shown as the upper horizontal axis in Figure 19(C). Also plotted are the noise floor levels from the two additional cases, i.e. 1) when the sampling arm was blocked, and 2) both the reference and sample arms were blocked, respectively. It is clear that the noise levels are close to the system noise floor when the sample arm was blocked for two different A sampling densities examined, indicating that the noise in OMAG is dominated by the light intensity fluctuation noise and system noise. On the other hand, it implies that the system was not operated at the shot-noise limited detection mode when compared with the system noise floor (see the bottom curve in Figure 19(C)). Therefore, this noise level can still be further reduced if the light energy in the reference arm is optimized for imaging so that the shot-noise limited detection is achieved. In this particular experiment, we set the modulation frequency of f_M = 0.3 kHz in the spatial interferogram, equivalent to a velocity threshold of ~200 μm/s for OMAG imaging. This performance gives superb ability for OMAG to detect the flow within the sample because the flow signal is with much high dynamic range, equivalent to the OCT system dynamic range which in this case is >95dB within the imaging depth of 2.5mm. Note that this flow signal dynamic range is different from the flow velocity dynamic range. The latter is determined by the modulation frequency and the maximum scan rate of CCD used for imaging that is [0.2 3.25] mm/s for this study. More important, the signals at deeper imaging depth are without artifact noise which is important if we are imaging the microcirculation

blood flow through the overlaying tissues, for example accessing the cortical blood perfusion through the skin and skull bone for mice imaging.

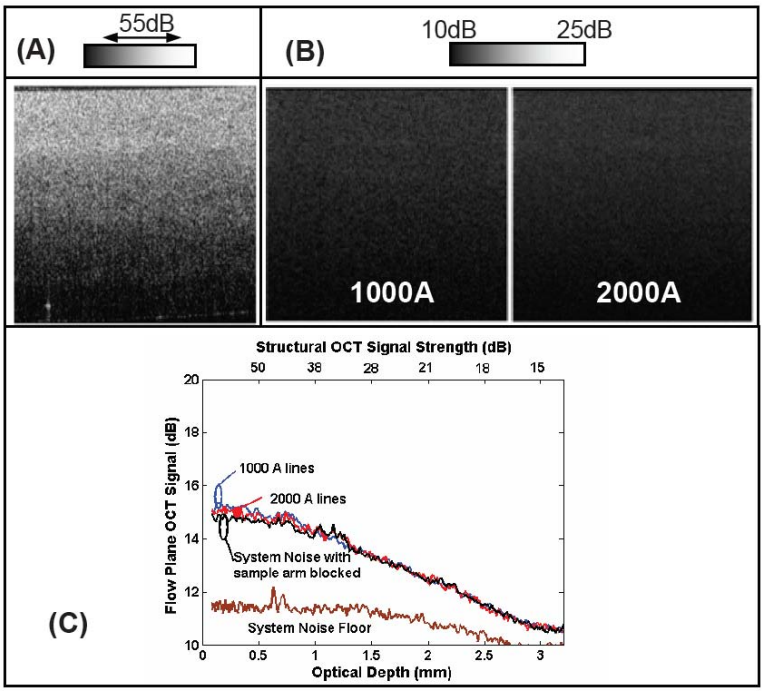

Figure 19: Imaging of a solid scattering material to assess the noise level of OMAG imaging performance. 1000 and 2000 A scan spatial sampling density over 2.5 mm of B scan are given, respectively. (A) OCT/OMAG structural image, (B) OMAG flow image where there is almost no improvement when denser sampling approach is used, and (C) background noise level plotted as a function of depth in OMAG flow image, which results suggesting OMAG delivers superb flow imaging performance.

To evaluate the flow signals at the deeper imaging locations within sample, we used OMAG system to image the blood circulation within the finger nail bed of an adult volunteer. The *in vivo* OMAG imaging results are given in Figure 20. The micro-circulations are located at the living nail bed which in this case is about ~0.8mm beneath the nail surface. Despite attenuation of the OCT signals as well as optical heterogeneity of the nail plate and bed, OMAG clearly identifies the blood perfusion within the capillaries with good signal to background noise ratio. This attributes to that OMAG imaging is free of artifact noises along the imaging depth.

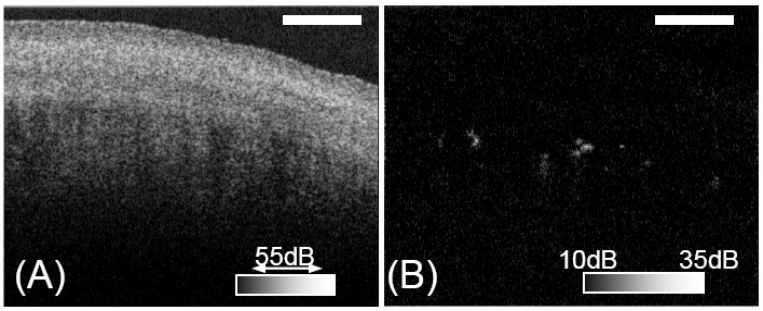

Figure 20: *In vivo* imaging of the finger nail bed of an adult volunteer (41 years age). Shown is a B scan consisting of 1000 A scans across 2.5mm. (A) Structural OCT/OMAG image where the nail plate and bed can be clearly visualized. (B) OMAG flow image where it is evident that the capillary blood flows within nail bed are abundant. The white bar indicates 500 μm.

4.4.2 *In vivo* mouse imaging results

Next, we used the OMAG system to image the cerebro-vascular blood perfusion in mice with the intact skin and skull *in vivo*. All experiments were performed on C57Bl/6 male mice (Charles River Colony) which weighed 15 to 20 g and were approximately 3 months old. All the procedures were done using sterile technique and the mice were prepared for OMAG imaging 24 hours in advance by shaving their heads followed by an application of depilatory cream (Nair) to remove all remaining hair on the skin. For OMAG scans the animal was mounted on a custom made stereotaxic stage which stabilized the head. During imaging, the mouse was lightly anesthetized using 2% isoflurane (0.2L/min O2, 0.8L/min air). The body temperature was maintained by a warming blanket and was kept between 36.7-37.1 C monitored by a rectal thermal probe. A drop of mimeral oil was applied and spreaded uniformily on the skin of head before the imaging was taken place in order to minimize the strong skin surface reflection. After OMAG imaging, the animal was euthanized by cervical dislocation and digital images were taken (Roper Scientific Photometrics Coolsnap cf) of the head. Next the skin and skull on the head were carefully removed to expose the dorsal blood vessels of the brain which were then photographed to be compared with that from the OMAG imaging system. All animals were disposed of according to IACUC regulations. The protocol was approved by the Oregon Health & Sciences University Institutional Animal Care and Use Committee and

was in compliance with the guidelines of the National Institutes of Health for care and handling of laboratory animals.

3-D OMAG images including structural morphology and blood perfusion were computed by evaluating the spectrogram data slice by slice, then re-combining to yield the 3-D volume dataset (x-y-z), from which high quality information regarding vasculature, blood flow and microstructures can be extracted. In the positive space of OMAG imaging method, there was obtained the 3-D localized microstructural image. Figure 21 illustrates the 3D volume rendered image representing the structural information of the scanned tissue volume of 2.5x2.5x2.0 (x-y-z) mm^3, from which the histologically important layers such as skin, skull bone and grey matter are clearly identified. The average thicknesses of the skin and skull were estimated at ~355μm and ~188μm, respectively. This 3-D image can be rotated and cut in any directions and planes so that the detailed morphological information within scanned volume can be examined. It is clear that the 1.3 μm light source penetrated through the skin and skull bone, giving an opportunity to access to the cortex of the mouse brain for evaluating the brain activity without the need to remove the intervening skin and bone for imaging such as in confocal microscopy. However, it is difficult to visualize the blood flows within the scanned tissue from the structural image. Because red blood cells flow through all blood vessels including capillaries, acting as the moving scattering particles when exposed under the OMAG system, the blood flows can be precisely localized in the negative space in OMAG. As the positive and negative spaces are exactly mirrored, they can be folded to fuse a single volume image to localize with high precision the blood vessels within the tissue sample. Figure 22(A) shows such a volume image that was resulted from by fusing the OMAG structural and flow images together, where a cut away view in the central area of micro-structural volume is used to more clearly appreciate how the blood vessels are oriented in the 3D volume.

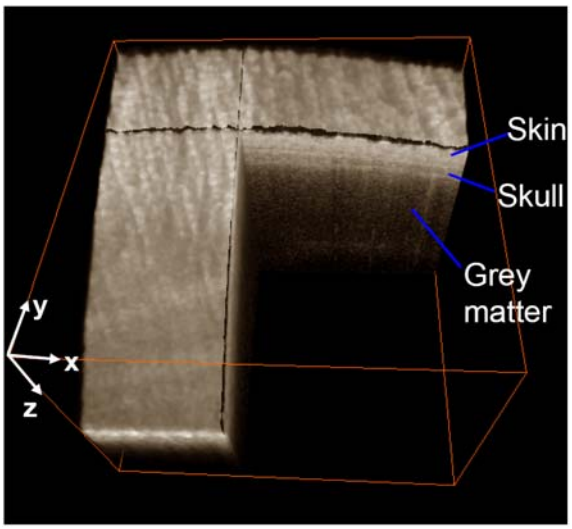

Figure 21: Cut away view of volume image rendered from 3-D micro-structural images of the mouse head obtained by OMAG system *in vivo*, where the important tissue layers, such as skin, skull bone and grey matter are clearly identified. The volume image given has a physical dimension of 2.5x2.5x2.0 mm^3 in x-y-z direction as shown.

Because OMAG gives the depth-resolved blood perfusion image of the scanned tissue volume, the blood flows within the skin and brain cortex can be separated so that the quantification of cerebral vascular perfusion is possible without the interference from the blood perfusion located within the skin. The results are given in the right side of Figure 22, where the x-y projections of blood flows existed within the skin that was detected by OMAG is shown in Figure 22(B), while the cerebral blood perfusion is illustrated in Figure 22(C). In obtaining the depth-resolved blood flow projection images, an image segmentation algorithm was used to separate the blood flow signals within skin from those within the brain cortex. The steps of segmentation algorithm included: 1) By utilizing the 3D OMAG structural image, such as Figure 21, the skin surface was found by a simple intensity-threshold method. 2) The resulted skin surface found in step 1 was then smoothed in 3D space in order to improve the accuracy of the 3-D volume segmentation. 3) Two 3D masks were then generated, i.e. skin mask and brain mask. Skin mask covers the tissue volume 500 μm below the smoothed

surface from step 2. This made sure that the bottom boundary of 3D skin mask was situated approximately within the skull bone. A further 1000 μm below the skin mask was then made up of the brain mask. 4) Because the OMAG structural image coins with the blood perfusion image, the two masks obtained in step 3 was applied to the OMAG blood perfusion image to generate two separate 3D flow images, one representing the signals from the skin and another from the mouse brain. 5) Finally, maximum amplitude projection (MAP) approach was used to project the segmented blood flow images onto the x-y plane. This algorithm resulted in the blood flow projection images in the skin (Figure 22(B)) and the brain cortex (Figure 22(C)). For visual comparison, Figure 22(D) gives the MAP projection image of the blood perfusion without the application of segmentation algorithm as described.

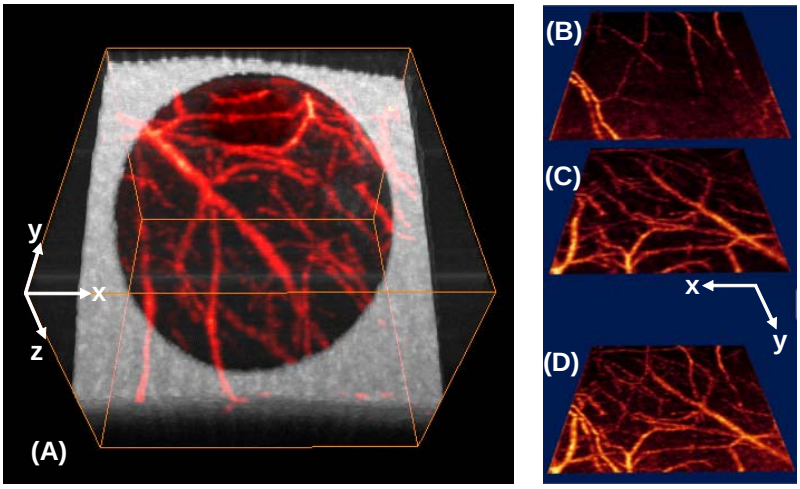

Figure 22. Cerebral blood perfusion was imaged with OMAG *in vivo* with the intact skin and cranium. (A) volumetric rendering of fused 3D OMAG micro-structural and blood perfusion image. The volume size is 2.5x2.5x2.0 mm^3, **(B)** projection image of blood flows from within the skin; **(C)** projection image of cerebro-vascular perfusion from brain cortex; and **(D)** Projection image from all depths.

In the next imaging experiment, we used OMAG to obtain multiple 3-D images of the same mice brain with the skin and skull intact over different regions of the head. The scan was performed clockwise that resulted in six OMAG images covering an area of approximately 4.2x7.2 mm^2 over the mouse head. The total imaging acquisition time required to scan such an area and to stream the spectral data from the camera into the host computer was 7.5 minutes. The volume segmentation algorithm as described above was then applied to the six OMAG images separately to isolate the blood perfusion signals within the skin from those coming from the mouse brain. The MAP images from different regions of head were finally combined as a mosaic. Figure 23(A) shows the mapping of blood flows within the skin of the mouse, while the cerebro-vascular blood perfusion is given in Figure 23(B). For comparison, the photograph of the head right after the OMAG imaging and the photograph of the brain cortex after removal of the skin and skull bone are shown in Figure 23(C) and Figure 23(D), respectively. From Figure 23(C), seeing the blood vessels through the skin is almost impossible. However, OMAG offers the opportunity to visualize the cerebral blood perfusion through the skin and skull. Comparing between Figure 23(B) and Figure 23(D), excellent agreement on the major vascular network over the brain cortex is achieved. Furthermore, the smaller blood vessels not observed in the photograph of Figure 23(D) can be seen in the OMAG images, indicating the OMAG capability to delineate the capillary level vessels. The capacity of OMAG to achieve such high resolution imaging of the cerebral cortex – within minutes and without the need for dye injections, contrast agents, removal of skin or surgical craniotomy, - makes it an extremely valuable tool for studying the hemodynamics of the brain. This may give great potential for OMAG in the investigations of neurological diseases and brain functions in small animal models, for example, ischemic thrombotic stroke and neurological responses to sensory stimulations, which are widely studied in small animal models such as the genetically altered mouse.

It should be noted that the OMAG imaging of blood flow is only sensitive to the z component, i.e. flow velocity projected onto the probe beam direction. This is because the imaging is relied on the Doppler frequency induced in the optical interferogram by the moving blood cells. If a blood cell moves at a velocity of *v*, then the Doppler frequency induced in OMAG signal will be $f_D = {2v\cos(\theta)}/{\bar{\lambda}}$, where θ is the angle between the probe beam direction and the blood flow direction, and $\bar{\lambda}$ is the center wavelength of the light source used. It is obvious that if $\theta = 90^0$, $f_D = 0$. As a consequence, OMAG is not sensitive to the transverse blood flow. This could however be amended if one carefully positions the OMAG probe beam so that $\theta \neq 90^o$ for the targeted tissue volume. Another solution maybe to use a dual-system with the probe-beam from each system pointing to the tissue sample at a different angle, or imaging is being performed by two consecutive scans to the same tissue volume while one changes the angle of OMAG probe beam in the second scan relative to the first scan. In this case, imaging time and computational effort will inevitably be increased.

The acquisition time for a full 3D data volume was ~50 seconds in the current study. This acquisition time was partially limited by the output power of the light source employed in the system. The imaging acquisition time can be shortened by a number of ways in order to investigate the functional changes in the brain that occur on a time scale shorter than ~50 seconds. With the spatial resolution fixed, one obvious approach is to increase the OMAG imaging speed by employing a higher power light source and a faster infrared InGaAs CCD camera. However, if one does not need a high spatial resolution, the OMAG imaging can be configured to acquire less B scans that consist of C scan so that the imaging time is shortened.

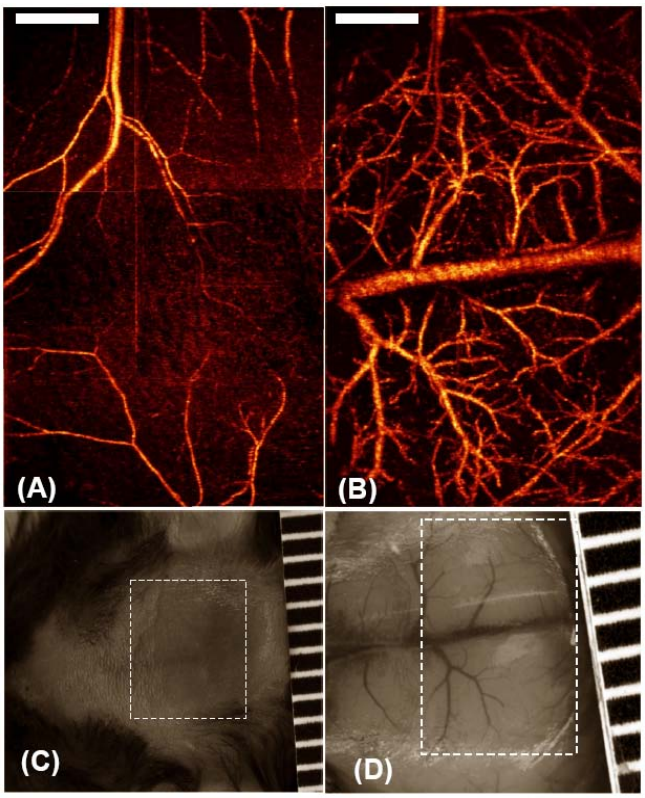

Figure 23. The head of an adult mouse with the skin and skull intact was imaged with OMAG *in vivo*. (A) and **(B)** are the projection views of blood perfusion from within the skin and the brain cortex, respectively. Capillary blood flow can be seen from **(B)**. It took ~7.5 minutes to acquire the 3-D data to obtain **(A)** and **(B)** using the current system setup. **(C)** Photograph taken right after the experiments where viewing the vasculatures through the skin is impossible. **(D)** Photograph showing blood vessels over the cortex after the skull and the skin of the same mouse were carefully removed. The superficial major blood vessels show excellent correspondence with those in **(B)**. The area marked with dashed white box represents 4.2 by 7.2 mm^2; and the scale bar indicates 1.0 mm.

4.5 Conclusions

Because of the increased penetration depth at 1.3μm in biological tissue compared to that of ~800nm band light source, an optical micro-angiography imaging system has been constructed and demonstrated for *in vivo* imaging by employing a broadband SLD with central wavelength at 1.3 μm. The system was based on the spectral domain configuration with a high speed InGaAs line scan camera for spectrogram detection, similar to the spectral domain optical coherence tomography. We have shown that the system is capable of volumetric

imaging of micro-structural morphology and blood perfusion in parallel of tissue samples *in vivo*. With this OMAG imaging system, we have obtained high quality and spatially resolved cerebrovascular blood perfusion images of live mice down to capillary level resolution through the intact skin and cranium without the interference of the blood perfusion from within skin. More important, no exogenous contrasting agents are necessary because the imaging contrast of OMAG is based on the endogenous light scattering signals. Without the need for dye injections, contrast agents, removal of skin or surgical craniotomy, the results demonstrate the potential of 1.3μm OMAG as a high resolution and high sensitivity imaging tool in the investigations of cerebrovascular diseases in small animal models.

Chapter 5: Future Work

5.1 OMAG assessment of experimental stroke in mice

In the standard MCAO model of stroke, infusion of tPA marginally improved disease outcome, but significantly reduced infarct size. This finding was similar to the effect of tPA in human stroke patients, thus verified the research utility of the model and protocol. Table 1 shows the hemorrhage, infarct volume percentage, edema percentage, neurological score, and laser Doppler flow normalized percentage for mice treated with tPA, vehicle, and no treatment. As it can be seen in Figure 24 and from Table 1, the vehicle treated animals had a much larger infarct volume compared to tPA treated animals. This in turn affected the animals' behavior (Figure 24C) which was measured on a modified Hara scale. The Hara scale relates behavior of the animal with 0 being normal and 5 representing death.

After showing that tPA does reduce the infarct volume by 42% and decreases behavior score by half as compared to vehicle we used OMAG to quantify the vascular reperfusion into the ischemic area. First though we needed to quantify the blood flow we observed with OMAG to a standard that already exists. By using the standard perfusion iodoantipyrine (IAP) autoradiographic technique which measures milliliters of blood per 100 grams of tissue per minute we compared the image obtained by OMAG to the IAP in the same animal (n=3).

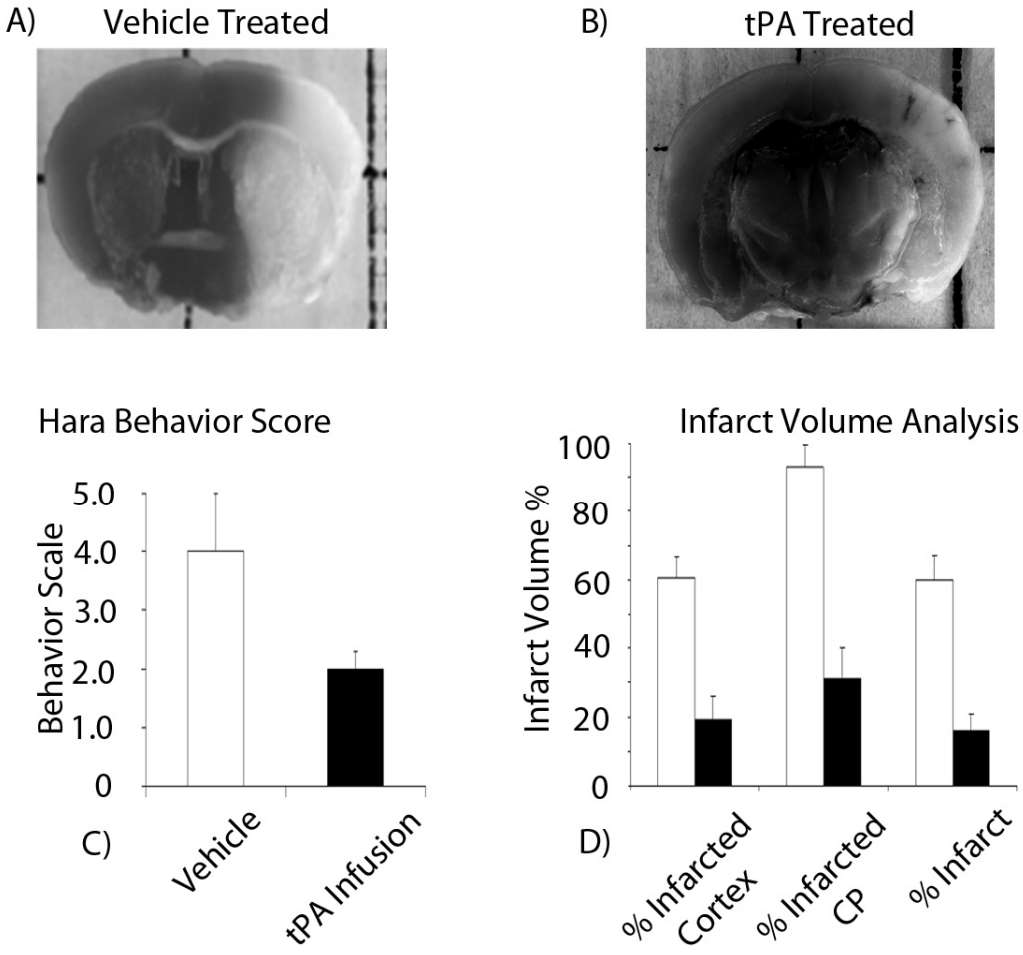

Figure 24. Standard histological analysis of mice with MCAO while being treated with tPA or vehicle. A-B) Vehicle and tPA treated coronal section of TTC stained mouse brain. C) Hara Behavior scale ranked 0: Normal – 5: Death. D) Volumetric Infarct Analysis.

Table 1: Effect of intravenously administered tPA on a mouse with MCAO.

Treatment	Dose	N (number of animals evaluated that survive MCAO surgery)	Mortality (number of deaths between 2 and 24 hours post MCAO)	Hemorrhage (macroscopic intracranial bleeding)	Infarct (% ipsilateral hemisphere, mean ± SEM)	Edema (% ipsilateral hemisphere, mean ± SEM)	Neurology (24 hour behavior performace score, mean ± SEM)	Blood flow (% of baseline at 15 min post-reperfusion, mean ± SEM)
None	-	10	3/13	3/13	60.0 ± 6.7	11.4 ± 1.1	3	ND
Vehicle	0.9% NaCl; IV infusion at 15-60 min, 185 µL	10	2/12	3/12	58.0 ± 5.6	9.0 ± 1.9	4	47.0 ± 3.0
tPA	10 mg/kg/hr; IV infusion at 15-60 min during MCAO, 185 µL	10	3/13	4/13	15.9 ± 4.9	6.7 ± 1.0	2	81.0± 5.2

Figure 25 shows the comparison of OMAG with IAP. Figure 25A is the *In vivo* OMAG Cerebral Blood Flow image. The '+' symbol illustrates locations used to compare the blood flow volume rate obtained from OMAG with those from Iodoantipyrine (IAP) postmortem. Shown are the data from n=3 animals. Figure 25B is the correlation of the data set from OMAG (vertical axis) with IAP (horizontal axis) and Figure 25C is the correlation of the averaged data over hemisphere from OMAG with IAP.

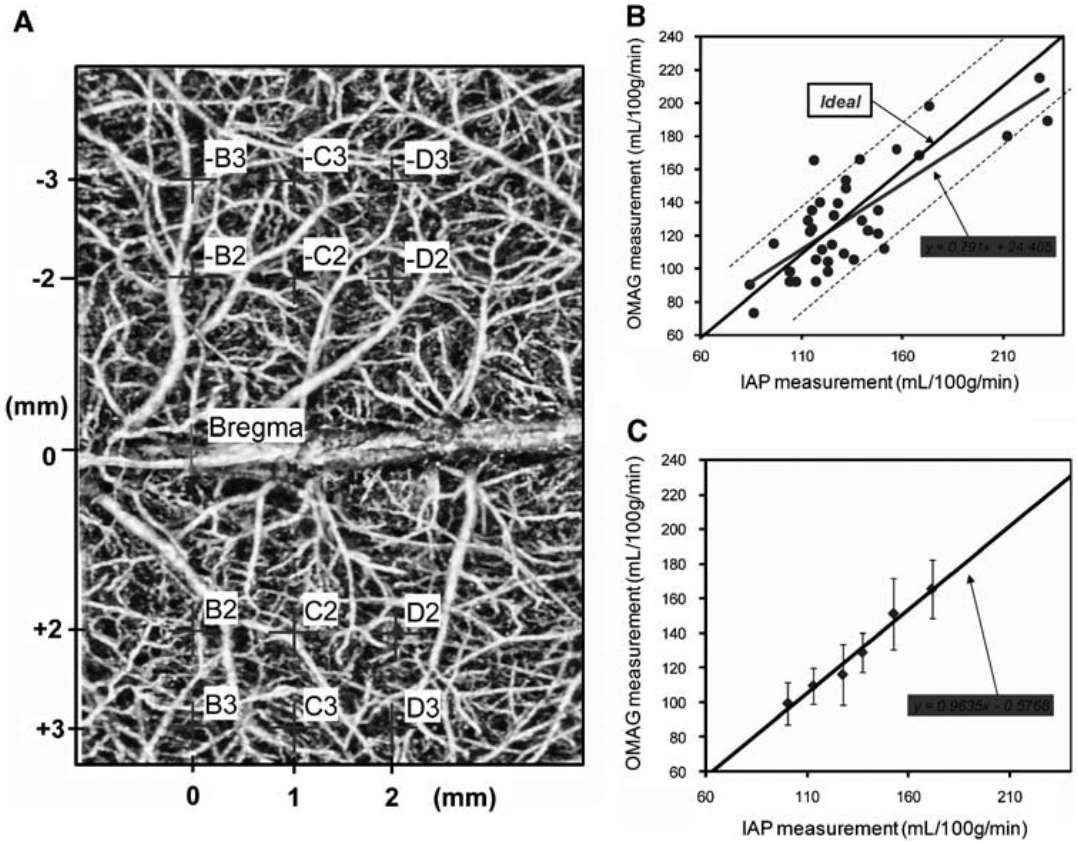

Figure 25: Blood flow volume comparison of OMAG with IAP. A) OMAG image of one mouse (n=3). The '+' represent compared areas. B) Correlation graph of IAP to OMAG in n=3 animals. C) Average blood flow of n=3 animals. IAP flow on x-axis and OMAG flow on y-axis. This figure was presented at *International Stroke Conference*, New Orleans, LA (Feb, 2008). Hurst S, Haung W, Zhang W, Alkayed NJ, Gruber A, Wang RK. "In-Vivo Optical Imaging of Cerebral Blood Perfusion during Focal Ischemia in Mice."

After correlation of OMAG and IAP data we can safely say that the blood flow images observed and analyzed match closely to those of the standard perfusion measurement techniques. One advantage of OMAG is that not only the macrovasculature, like IAP, but the microvasculature as well can be analyzed. Figure 26 is the 3D time progressive compilation of a mouse being treated with vehicle (saline infusion) while induced with MCAO over 60 minutes (Figure 26A-E). Then reperfusion is tracked for 50 minutes (Figure 26F-J).

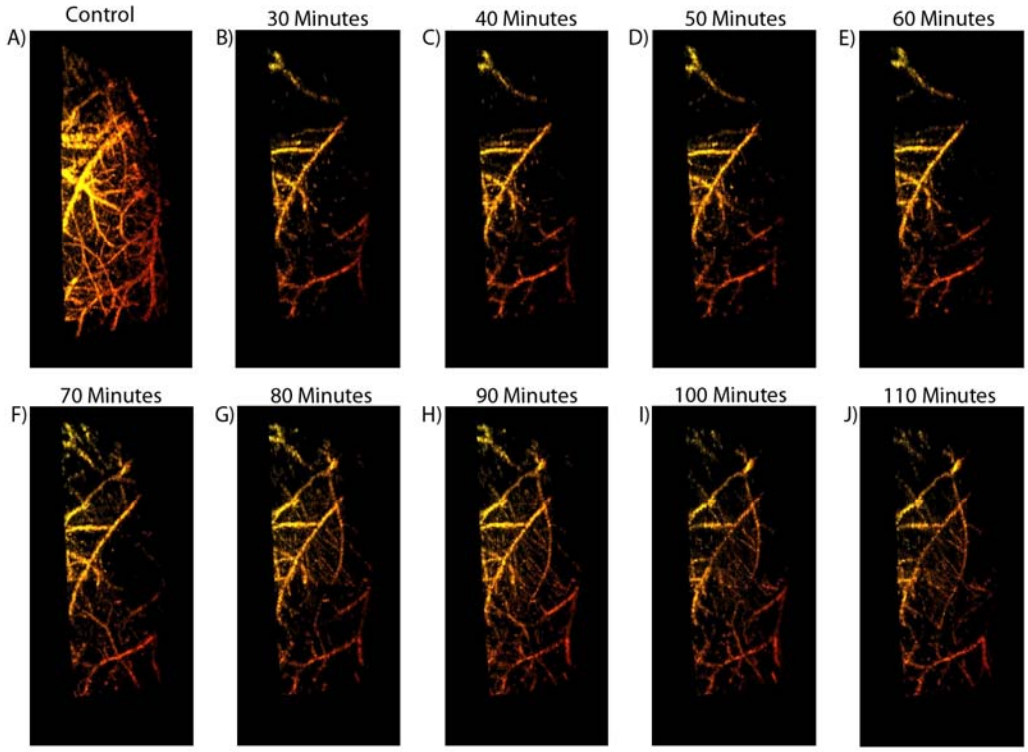

Figure 26: 3-Dl vascular flow imaging taken progressively while mouse is under going MCAO and vehicle (saline) infusion treatment (A-E) then progressive reperfusion images (F-J).

The image can also be processed in a two dimensional projection view as shown in Figure 27. Both images show the drop in blood flow due to the vessels being occluded. While the animal is being imaged, saline is being infused. As it is seen in both Figure 26 and 27, further progression of the ischemic region occurs due to the lack of perfusion in the vessels proximal to the occlusion. The loss of blood flow and blood volume is imaged in real time *in vivo* by OMAG.

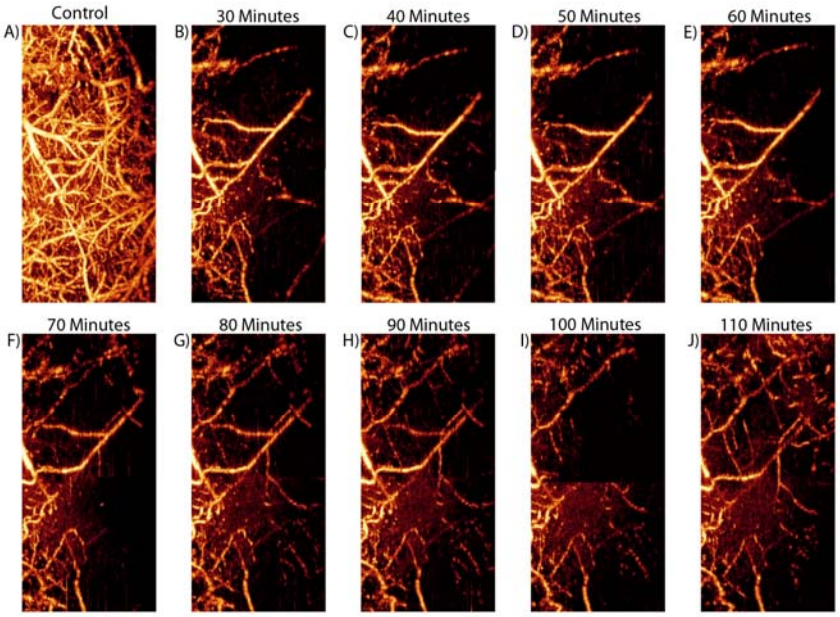

Figure 27: Projection view vascular flow imaging taken progressively while mouse is under going MCAO and Vehicle (saline) infusion treatment (A-E) then progressive reperfusion images (F-J).

While in Figures 28 and 29, which are of a mouse during MCAO while tPA (10 mg/kg/hr) is being infused, shows a much larger return of vascular function. The reperfusion and blood volume is much greater when compared to vehicle. Both have ischemic areas but when reperfusion occurs the thrombolytic activity of tPA allows for a greater reperfusion as well as blood volume to return to the penumbra of the ischemic brain tissue. The returned blood flow and volume allows for more tissue to be recovered and thus a better outcome for the animal can be seen.

Figure 30A shows the blood volume after reperfusion as calculated from the pixel intensity from the OMAG images. Vehicle (n=3) and tPA treated (n=3) animals were compared over 110 minutes. The control image (Figure 26-29A) was used to normalize the following progressive stroke images. The OMAG show a comparable result with the LDF vehicle (n=5) and tPA treated (n=5) which is shown in fig 30B.

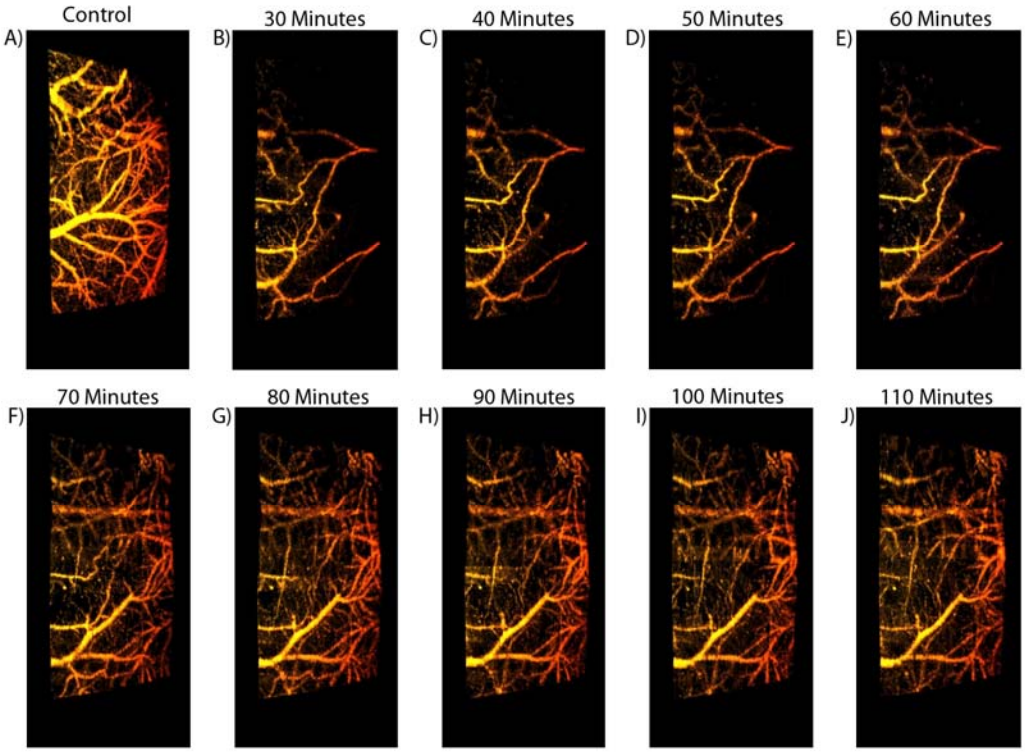

Figure 28: 3D vascular flow imaging taken progressively while mouse is under going MCAO with tPA infusion treatment (A-E) then progressive reperfusion images (F-J).

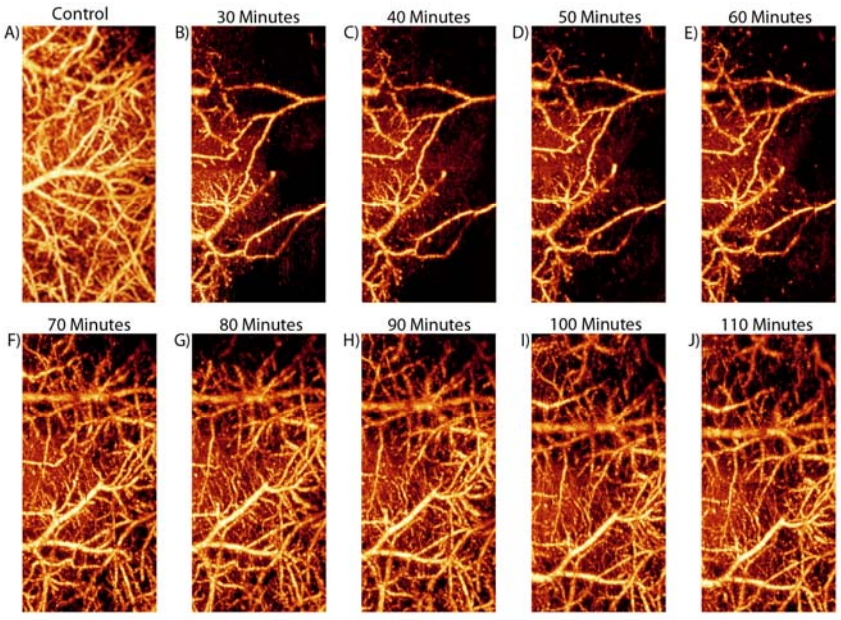

Figure 29. Projection view vascular flow imaging taken progressively while mouse is under going MCAO and tPA infusion treatment (A-E) then progressive reperfusion images (F-J).

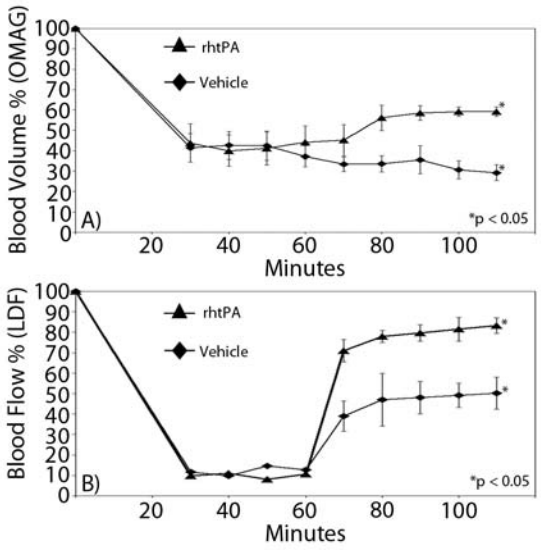

Figure 30: Comparison of OMAG blood volume to transcranial LDF.

5.2 Discussion

OMAG imaging provided real-time volumetric measurements of blood perfusion of the cerebral cortex through the intact skull without the need for dye injection, contrast agents, or surgical craniotomy. Detailed 3D flow architecture obtained by OMAG had an excellent agreement with that from direct photographing of blood vessels on the surface of the cerebral cortex. Quantitative assessment of blood flow rates using OMAG imaging was within 20% of CBF rates measured in the same region using IAP autoradiography. Repeated OMAG imaging during and after mechanical MCAO in mice captured perfusion cessation in the ipsilateral hemisphere during stroke and revealed significant changes in the perfusion pattern of the contralateral hemisphere. Upon removal of the mechanical obstruction from the MCA, blood perfusion resumed in some capillary beds, while other capillaries remained closed, indicating progressive vascular occlusions distal to the primary blockage. The thrombotic origin of these occlusions was verified by responsiveness of reperfusion rate to thrombolytic treatment with tPA. OMAG images were in good agreement with the expectation that thrombotic occlusions during ischemic stroke

reduce cortical perfusion and thrombolytic treatment with tPA dramatically improves the blood supply of the cerebral cortex. Thus, OMAG provides an accurate assessment of perfused vascular architecture, with quantitative dynamic perfusion information in real time and allows for repeated, non-invasive and simultaneous *in vivo* assessment of blood flow rates within near-surface areas, such as the cerebral cortex of mice. OMAG therefore will be useful for the non-invasive evaluation of near-surface microvascular pathology and its responsiveness to treatments,

References

1. Kung, H. C., Hoyert, D. L., Xu, J., and Murphy, S. L., Deaths: final data for 2005, *Natl Vital Stat Rep, 56*, 1 (2008).
2. Lloyd-Jones, D., Adams, R., Carnethon, M., De Simone, G., Ferguson, T. B., Flegal, K., Ford, E., Furie, K., Go, A., Greenlund, K., Haase, N., Hailpern, S., Ho, M., Howard, V., Kissela, B., Kittner, S., Lackland, D., Lisabeth, L., Marelli, A., McDermott, M., Meigs, J., Mozaffarian, D., Nichol, G., O'Donnell, C., Roger, V., Rosamond, W., Sacco, R., Sorlie, P., Stafford, R., Steinberger, J., Thom, T., Wasserthiel-Smoller, S., Wong, N., Wylie-Rosett, J., and Hong, Y., Heart disease and stroke statistics--2009 update: a report from the American Heart Association Statistics Committee and Stroke Statistics Subcommittee, *Circulation, 119*, e21 (2009).
3. Rosamond, W., Flegal, K., Furie, K., Go, A., Greenlund, K., Haase, N., Hailpern, S. M., Ho, M., Howard, V., Kissela, B., Kittner, S., Lloyd-Jones, D., McDermott, M., Meigs, J., Moy, C., Nichol, G., O'Donnell, C., Roger, V., Sorlie, P., Steinberger, J., Thom, T., Wilson, M., and Hong, Y., Heart disease and stroke statistics--2008 update: a report from the American Heart Association Statistics Committee and Stroke Statistics Subcommittee, *Circulation, 117*, e25 (2008).
4. Solomon, N. A., Glick, H. A., Russo, C. J., Lee, J., and Schulman, K. A., Patient preferences for stroke outcomes, *Stroke, 25*, 1721 (1994).
5. Davie, E. W., and Ratnoff, O. D., Waterfall Sequence for Intrinsic Blood Clotting, *Science, 145*, 1310 (1964).
6. Macfarlane, R. G., An Enzyme Cascade in the Blood Clotting Mechanism, and Its Function as a Biochemical Amplifier, *Nature, 202*, 498 (1964).
7. Hacke, W., Kaste, M., Fieschi, C., Toni, D., Lesaffre, E., von Kummer, R., Boysen, G., Bluhmki, E., Hoxter, G., Mahagne, M. H., and et al., Intravenous thrombolysis with recombinant tissue plasminogen activator for acute hemispheric stroke. The European Cooperative Acute Stroke Study (ECASS), *Jama, 274*, 1017 (1995).
8. Albers, G. W., Amarenco, P., Easton, J. D., Sacco, R. L., and Teal, P., Antithrombotic and thrombolytic therapy for ischemic stroke: the Seventh ACCP Conference on Antithrombotic and Thrombolytic Therapy, *Chest, 126*, 483S (2004).
9. Ito, H., Yamamoto, S., Komai, T., and Mizukoshi, H., Role of local hyperfibrinolysis in the etiology of chronic subdural hematoma, *J Neurosurg, 45*, 26 (1976).
10. Effect of intravenous recombinant tissue plasminogen activator on ischemic stroke lesion size measured by computed tomography. NINDS; The National Institute of Neurological Disorders and Stroke (NINDS) rt-PA Stroke Study Group, in *Stroke*, Vol. 31, pp. 2912 (2000).
11. Benchenane, K., Lopez-Atalaya, J. P., Fernandez-Monreal, M., Touzani, O., and Vivien, D., Equivocal roles of tissue-type plasminogen activator in stroke-induced injury, *Trends Neurosci, 27*, 155 (2004).
12. Wardlaw, J. M., and Warlow, C. P., Thrombolysis in acute ischemic stroke: does it work?, *Stroke, 23*, 1826 (1992).

13. O'Collins, V. E., Macleod, M. R., Donnan, G. A., Horky, L. L., van der Worp, B. H., and Howells, D. W., 1,026 experimental treatments in acute stroke, *Ann Neurol, 59*, 467 (2006).
14. Liebeskind, D. S., Imaging the future of stroke: I. Ischemia, *Ann Neurol, 66*, 574 (2009).
15. A.F. Fercher, W. D., C. K. Hitzenberger, and T. Lasser, *Optical Coherence Tomography - Principles and Applications*, Vol. 66, Rep. Prog. Phys. (2003).
16. Wang, P. H. T. a. R. K., Theory, development and applications of optical coherence tomography, *J. Phys. D: Appl. Phys, 38*, 2519 (2005).
17. Huang, D., Swanson, E. A., Lin, C. P., Schuman, J. S., Stinson, W. G., Chang, W., Hee, M. R., Flotte, T., Gregory, K., Puliafito, C. A., and et al., Optical coherence tomography, *Science, 254*, 1178 (1991).
18. Boppart, S. A., Bouma, B. E., Pitris, C., Southern, J. F., Brezinski, M. E., and Fujimoto, J. G., In vivo cellular optical coherence tomography imaging, *Nat Med, 4*, 861 (1998).
19. Drexler, W., Morgner, U., Ghanta, R. K., Kartner, F. X., Schuman, J. S., and Fujimoto, J. G., Ultrahigh-resolution ophthalmic optical coherence tomography, *Nat Med, 7*, 502 (2001).
20. Tearney, G. J., Brezinski, M. E., Bouma, B. E., Boppart, S. A., Pitris, C., Southern, J. F., and Fujimoto, J. G., In vivo endoscopic optical biopsy with optical coherence tomography, *Science, 276*, 2037 (1997).
21. G. Hausler, M. W. L., Coherence radar and Spectral radar- new tools for dermatological diagnosis, *J. Biomed. Opt., 3*, 21 (1998).
22. Leitgeb, R., Hitzenberger, C., and Fercher, A., Performance of fourier domain vs. time domain optical coherence tomography, *Opt Express, 11*, 889 (2003).
23. B.R. White, M. C. P., N. Nassif, et al, In vivo dynamic human retinal blood flow imaging using ultra-high-speed spectral domain optical Doppler tomography, *Opt Express, 11*, 3490 (2003).
24. Leitgeb, R., Schmetterer, L., Drexler, W., Fercher, A., Zawadzki, R., and Bajraszewski, T., Real-time assessment of retinal blood flow with ultrafast acquisition by color Doppler Fourier domain optical coherence tomography, *Opt Express, 11*, 3116 (2003).
25. Z.P. Chen T.E. Milner, S. S., Noninvasive imaging of in vivo blood flow velocity using optical Doppler tomography, *Opt. Lett., 22*, 119 (1997).
26. S. Jiao, L. H. W., Two-dimensional depth-resolved Mueller matrix of biological tissue measured with double-beam polarization-sensitive optical coherence tomography, *Opt. Lett., 27*, 101 (2002).
27. U. Morgner, e. a., Spectroscopic optical coherence tomography, *Opt. Lett., 25*, 111 (2000).
28. Kirkpatrick, S. J., Wang, R. K., and Duncan, D. D., OCT-based elastography for large and small deformations, *Opt Express, 14*, 11585 (2006).
29. R.K. Wang, Z. M., and S.J. Kirkpatrick, Tissue Doppler optical coherence elastography for real time strain rate and strain mapping of soft tissue, *Appl. Phys. Lett., 89*, 144103 (2006).

30. Wang, R. K., and Ma, Z., A practical approach to eliminate autocorrelation artefacts for volume-rate spectral domain optical coherence tomography, *Phys Med Biol, 51*, 3231 (2006).
31. Bedrosian, E. A., Product theorem for Hilbert transforms, *Proc. IEEE, 51*, 868 (1963).
32. C. Dorrer, N. B., J.P. Likforman, M. Joffre, Spectral resolution and sampling issues in Fourier-transform spectral Interferometry, *J. Opt. Soc. Am. B., 17*, 1795 (2000).
33. Tuchin, V. V., Tissue Optics: Light Scattering Methods and Instruments for Medical Diagnosis, SPIE, USA (2000).
34. Wang, R. K., Modelling Optical Properties of Soft Tissue by Fractal Distribution of Scatters, *J. Modern Opt., 47*, 103 (2000).
35. Misgeld, T., and Kerschensteiner, M., In vivo imaging of the diseased nervous system, *Nat Rev Neurosci, 7*, 449 (2006).
36. H.W. Ren, Z. H. D., Y.H. Zhao, et al, Phase-resolved functional optical coherence tomography: simultaneous imaging of in situ tissue structure, blood flow velocity, standard deviation, birefringence, and Stokes vectors in human skin, *Opt. Lett., 27*, 1702 (2002).
37. Y.H. Zhao, Z. P. C., Z.H. Ding, et al, Real-time phase-resolved functional optical coherence tomography by use of optical Hilbert transformation, *Opt. Lett., 25*, 98 (2000).
38. J. Zhang, Z. P. C., In vivo blood flow imaging by a swept laser source based Fourier domain optical Doppler tomography, *Opt Express, 13*, 7449 (2005).
39. R.A. Leitgeb, L. S., C.K. Hitzenberger, et al, Real-time measurement of in vitro flow by Fourier-domain color Doppler optical coherence tomography, *Opt. Lett., 29*, 171 (2004).
40. Vakoc, B., Yun, S., de Boer, J., Tearney, G., and Bouma, B., Phase-resolved optical frequency domain imaging, *Opt Express, 13*, 5483 (2005).
41. Wang, R. K., and Ma, Z., Real-time flow imaging by removing texture pattern artifacts in spectral-domain optical Doppler tomography, *Opt Lett, 31*, 3001 (2006).
42. Makita, S., Hong, Y., Yamanari, M., Yatagai, T., and Yasuno, Y., Optical coherence angiography, *Opt Express, 14*, 7821 (2006).
43. Lindner, J. R., Microbubbles in medical imaging: current applications and future directions, *Nat Rev Drug Discov, 3*, 527 (2004).
44. McDonald, D. M., and Choyke, P. L., Imaging of angiogenesis: from microscope to clinic, *Nat Med, 9*, 713 (2003).
45. Malonek, D., Dirnagl, U., Lindauer, U., Yamada, K., Kanno, I., and Grinvald, A., Vascular imprints of neuronal activity: relationships between the dynamics of cortical blood flow, oxygenation, and volume changes following sensory stimulation, *Proc Natl Acad Sci U S A, 94*, 14826 (1997).
46. Hossmann, K. A., Viability thresholds and the penumbra of focal ischemia, *Ann Neurol, 36*, 557 (1994).
47. Padera, T. P., Stoll, B. R., So, P. T., and Jain, R. K., Conventional and high-speed intravital multiphoton laser scanning microscopy of microvasculature, lymphatics, and leukocyte-endothelial interactions, *Mol Imaging, 1*, 9 (2002).

48. Jain, R. K., Delivery of molecular medicine to solid tumors: lessons from in vivo imaging of gene expression and function, *J Control Release, 74*, 7 (2001).
49. Sakurada, O., Kennedy, C., Jehle, J., Brown, J. D., Carbin, G. L., and Sokoloff, L., Measurement of local cerebral blood flow with iodo [14C] antipyrine, *Am J Physiol, 234*, H59 (1978).
50. Calamante, F., Thomas, D. L., Pell, G. S., Wiersma, J., and Turner, R., Measuring cerebral blood flow using magnetic resonance imaging techniques, *J Cereb Blood Flow Metab, 19*, 701 (1999).
51. Heiss, W. D., Graf, R., Wienhard, K., Lottgen, J., Saito, R., Fujita, T., Rosner, G., and Wagner, R., Dynamic penumbra demonstrated by sequential multitracer PET after middle cerebral artery occlusion in cats, *J Cereb Blood Flow Metab, 14*, 892 (1994).
52. Grinvald, A., Lieke, E., Frostig, R. D., Gilbert, C. D., and Wiesel, T. N., Functional architecture of cortex revealed by optical imaging of intrinsic signals, *Nature, 324*, 361 (1986).
53. Dunn, A. K., Bolay, H., Moskowitz, M. A., and Boas, D. A., Dynamic imaging of cerebral blood flow using laser speckle, *J Cereb Blood Flow Metab, 21*, 195 (2001).
54. Nielsen, A. N., Fabricius, M., and Lauritzen, M., Scanning laser-Doppler flowmetry of rat cerebral circulation during cortical spreading depression, *J Vasc Res, 37*, 513 (2000).
55. Zhang, H. F., Maslov, K., Stoica, G., and Wang, L. V., Functional photoacoustic microscopy for high-resolution and noninvasive in vivo imaging, *Nat Biotechnol, 24*, 848 (2006).
56. Wang, X. D., Non-invasive laser-induced photoacoustic tomography for structural and functional imaging of the brain in vivo, *Nature Biotech, 21*, 803 (2003).
57. Wang, R. K., Jacques, S. L., Ma, Z., Hurst, S., Hanson, S. R., and Gruber, A., Three dimensional optical angiography, *Opt Express, 15*, 4083 (2007).
58. G. Hausler, M. W. L., Coherence radar and Spectral radar-new tools for dermatological dianosis, in *J. Biomed. Opt.*, Vol. 3, pp. 21 (1998).
59. Chen, Z. P., Noninvasive imaging of in vivo blood flow velocity using optical Doppler tomography, *Opt. Lett., 22*, 1119 (1997).
60. R.K. Wang, Z. M., and S.J. Kirkpatrick, Tissue Doppler optical coherence elastography for real time strain rate and strain mapping of soft tissue, *Appl. Phys. Lett., 89*, 1441 (2006).
61. Bouma, B. E., and Tearney, G. J., Clinical imaging with optical coherence tomography, *Acad Radiol, 9*, 942 (2002).
62. Carrion, L., Lestrade, M., Xu, Z., Touma, G., Maciejko, R., and Bertrand, M., Comparative study of optical sources in the near infrared for optical coherence tomography applications, *J Biomed Opt, 12*, 014017 (2007).
63. Y. Pan, a. D. L. F., Non-invasive imaging of living human skin with dual-wavelength optical coherence tomography in two and three dimensions, *J. Biomed. Opt., 3*, 446 (1998).
64. S.H. Yun, G. J. T., B.E. Bouma, B.H. Park, J.F. de Boer, High-speed spectral-domain optical coherence tomography at 1.3 ❍m wavelength, *Opt Express, 11*, 3598 (2003).

65. B.H. Park, M. C. P., B. Cense, S.H. Yun, M. Mujat, Real-time fiber-based multi-functional spectral-domain optical coherence tomography at 1.3 ❍m, *Opt Express, 13,* 3931 (2005).
66. Wang, R. K., In vivo full range complex Fourier Domain optical coherence tomography, *Appl. Phys. Lett., 90*, 054103 (2007).
67. C. Dorrer, N. B., J.P. Likforman, M. Joffre, Spectral resolution and sampling issues in Fourier-transform spectral Interferometry, *J. Opt. Soc. Am. B, 17*, 1795 (2000).
68. Wang, R. K., Modelling Optical Properties of Soft Tissue by Fractal Distribution of Scatters, *J. Mod. Opt., 47*, 103 (2000).

Biographical Sketch

A. Positions and Honors. List in chronological order previous positions, concluding with your present position. List any honors. Include present membership on any Federal Government public advisory committee.

Employment:

06/95 – 12/96	Biological Research Assistant, Dr. Marsha Trenary Laboratory, Institute of Molecular Biology, University of Oregon, Eugene, OR
01/97 – 03/97	Environmental Health and Safety, Cindy Jones, University of Oregon, Eugene, OR
04/97 – 01/99	Research Assistant, Dr. David Tyler Laboratory, Department of Chemistry, University of Oregon, Eugene, OR
03/00 – 09/04	Research Assistant 2, Dr. De-Ann M. Pillers Laboratory, Department of Pediatrics, Oregon Health & Science University, Portland, OR
09/04 – 03/10	Research Associate, Dr. Stephen Hanson Laboratory, Department of Biomedical Engineering, Oregon National Primate Research Center, Beaverton, OR
09/05 – Present	Research Associate, Dr. Ruikang Wang Biophotonics and Imaging Laboratory, Department of Biomedical Engineering, Portland, OR

09/04 – Present Research Associate, Dr. Andras Gruber Laboratory, Department of Biomedical Engineering, Oregon Health & Science University, Portland, OR

B. Selected peer-reviewed publications (in chronological order).

Sawan Hurst, * MS; Michelle A. Berny,* BS; Erik I. Tucker, PhD; Leslie A. Pelc, MS; Ruikang K. Wang, PhD; Patricia D. Hurn, PhD; Enrico Di Cera, MD; Owen J.T. McCarty, PhD; András Gruber, MD. Thrombin Mutant W215A/E217A Treatment Improves Neurological Outcome and Reduces Cerebral Infarct Size in a Mouse Model of Ischemic Stroke. Submitted to stroke 06/2010.

Erik I Tucker, Ulla M Marzec, Michelle A Berny, Sawan Hurst, Stuart Bunting, Owen J T Mccarty, Andras Gruber, Stephen R Hanson. Safety and antithrombotic efficacy of moderate platelet count reduction by thrombopoietin inhibition in primates. Science Translational Medicine 2010; 2(37): 1-8.

Erik I Tucker, Ulla M Marzec, Tara C White, Sawan Hurst, Sandra Rugonyi, Owen J T Mccarty, David Gailani, Andras Gruber, Stephen R Hanson. Prevention of vascular graft occlusion and thrombus-associated thrombin generation by inhibition of factor XI. Blood 2009; 113: 936—944.

Erik I Tucker, David Gailani, Sawan Hurst, Qiufang Cheng, Stephen R Hanson, Andras Gruber.Survival Advantage of Coagulation Factor XI-Deficient Mice during Peritoneal Sepsis. Journal of Infectious Diseases 2008; 198(2): 271—274.

William R. Woodward, Dongseok Choi, Jared Grose, Bojan Malmin, Sawan Hurst, Jiaqing Pang, Richard G. Weleber, De-Ann M. Pillers. Isoflurane is an

effective alternative to ketamine/xylazine/acepromazine as an anesthetic agent for the mouse electroretinogram. Documenta Ophthalmologica 2007; 115(3): 187—201.

Ruikang K. Wang, Steven L. Jacques, Zhenhe Ma, Sawan Hurst, Stephen R. Hanson, and Andras Gruber. Three dimensional optical angiography. Optics Express 2007; 15(7): 4083—4097.

Ruikang K. Wang, Sawan Hurst. Mapping of cerebro-vascular blood perfusion in mice with skin and skull intact by Optical Micro-Angiography at 1.3 um wavelength. Optics Express 2007; 15(18): 11402—11412.

Abstracts

Donald D. Duncan, Sean J. Kirkpatrick, James C. Gladish, and Sawan A. Hurst. Laser speckle contrast imaging for the quantitative assessment of flow. SPIE, 7176(03) (Jan, 2009)

Tucker EI, Marzec UM, Hurst S, Gruber A, Hanson SR. Moderate pharmacological platelet count reduction limits thrombus formation without haemostatic impairment in primates Blood 2008 (abstract # 1033)

White TC, Berny MA, Tucker EI, Hurst S, Urbanus RT, de Groot PG, Gruber A, McCarty OJT. Identification of Factor XI as a ligand for the platelet receptor apolipoprotein E receptor 2 Platelets 2008: 5th International Platelet Symposium, Woods Hole, MA (Oct, 2008).

Hurst S, Haung W, Zhang W, Alkayed NJ, Gruber A, Wang RK. In-Vivo Optical Imaging of Cerebral Blood Perfusion during Focal Ischemia in Mice. International Stroke Conference, New Orleans, LA (Feb, 2008).

A Gruber, S Hurst, PD Hurn, OJT McCarty, SR Hanson, R Razie, Non-anticoagulant activated protein C analog improves the neurological outcome of experimental stroke in mice. International Stroke Conference, New Orleans, LA (Feb, 2008).

Gruber A, Hurn PD, Hurst S, Bush L, Tucker EI, Hanson SR, Di Cera E. Protein C activator treatment improves the neurological outcome of experimental thrombotic ischemic stroke in mice. XXIst Congress of the International Society on Thrombosis and Haemostasis, Geneva, Switzerland (July, 2007).

Gruber A, Hurn PD, Hurst S, Bush L, Marzec UM, Tucker E, Hanson SR, Di Cera E., Thrombomodulin-dependent protein C activator treatment improves the short-term outcome of experimental ischemic stroke in mice. Blood. 108(11), 2006 (abstract #895).

D.M. Pillers, S. Hurst, G.K. Mack, R.G. Weleber, D.R. Trune, W.R. Woodward. Abnormalities in retinal electrophysiology in the laminin-deficient dy muscular dystrophy mouse model are part of a spectrum of organ pathophysiology suggesting critical role of laminin in development. Poster presentation at the Annual Meeting of the Association for Research in Vision and Ophthalmology (ARVO), Fort Lauderdale, May 2001. Investigative Ophthalmology and Visual Science 42:S767 (2001).

C. Research Support.

Ruth L. Kirschstein National Research Service Award (T32 grant) 1/07-3/09

OREGON HEALTH & SCIENCE UNIVERSITY

OHSU

Effect of intravenous recombinant tissue plasminogen activator on ischemic stroke in a mouse model of Middle Cerebral Artery Occlusion measured by Optical Microangiography

Presented by: Sawan Hurst

Date: 28 April 2010

Summary

- **Background**
- Hemostasis and Thrombolysis
- Effect of tPA on MCAO mouse model
- Development of OMAG
- Use OMAG to quantify tPA effect
- Conclusion and future work

Causes of Death in the US between 2000-2008

2.5 million deaths per year

150,000 deaths per year

765,000 strokes annually

85% due to ischemic injury

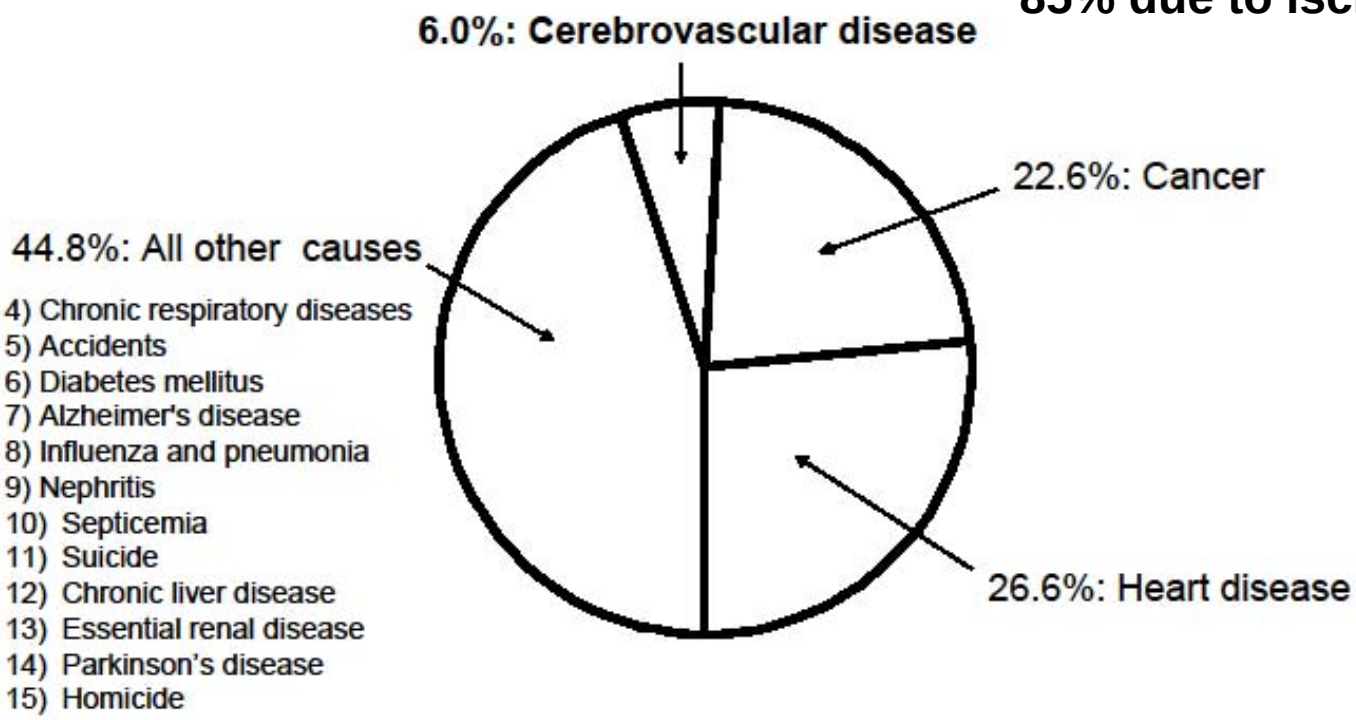

(Kung, Hoyert et al. 2008)

Disabilities in Surviving Population

2.5 million deaths per year

150,000 deaths per year

765,000 strokes annually

85% due to ischemic injury

615,000 survive

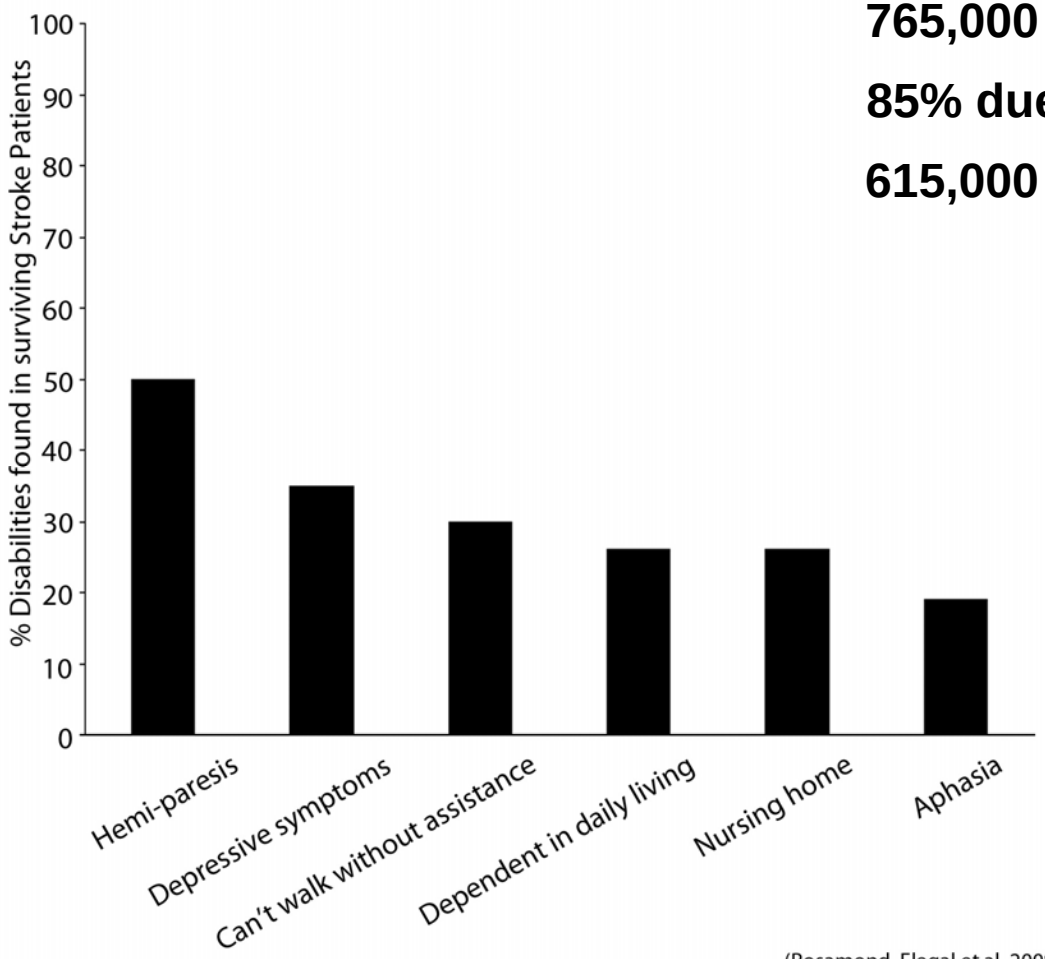

(Rosamond, Flegal et al. 2008)
(Solomon, Glick et al. 1994)

OREGON HEALTH & SCIENCE UNIVERSITY
OHSU

Cost analysis of Stroke

Hospital care

Nursing home care

Home healthcare

Physicians

Drugs and Disposable

43.7 billion dollars

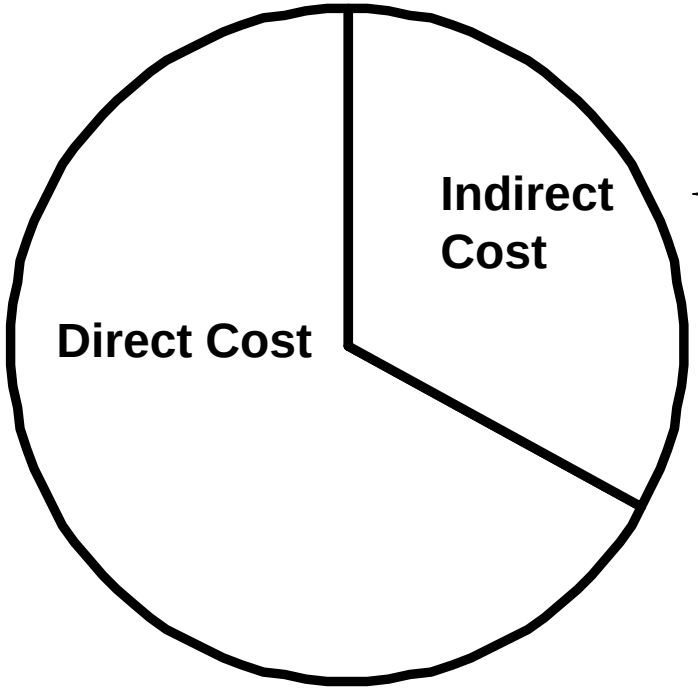

Lost Productivity, Mortality

Lost Productivity, Morbidity

21.8 billion dollars

(Solomon, Glick et al. 1994)

Summary

- Background
- **Hemostasis and Thrombolysis**
- Effect of tPA on MCAO mouse model
- Development of OMAG
- Use OMAG to quantify tPA effect
- Conclusion and future work

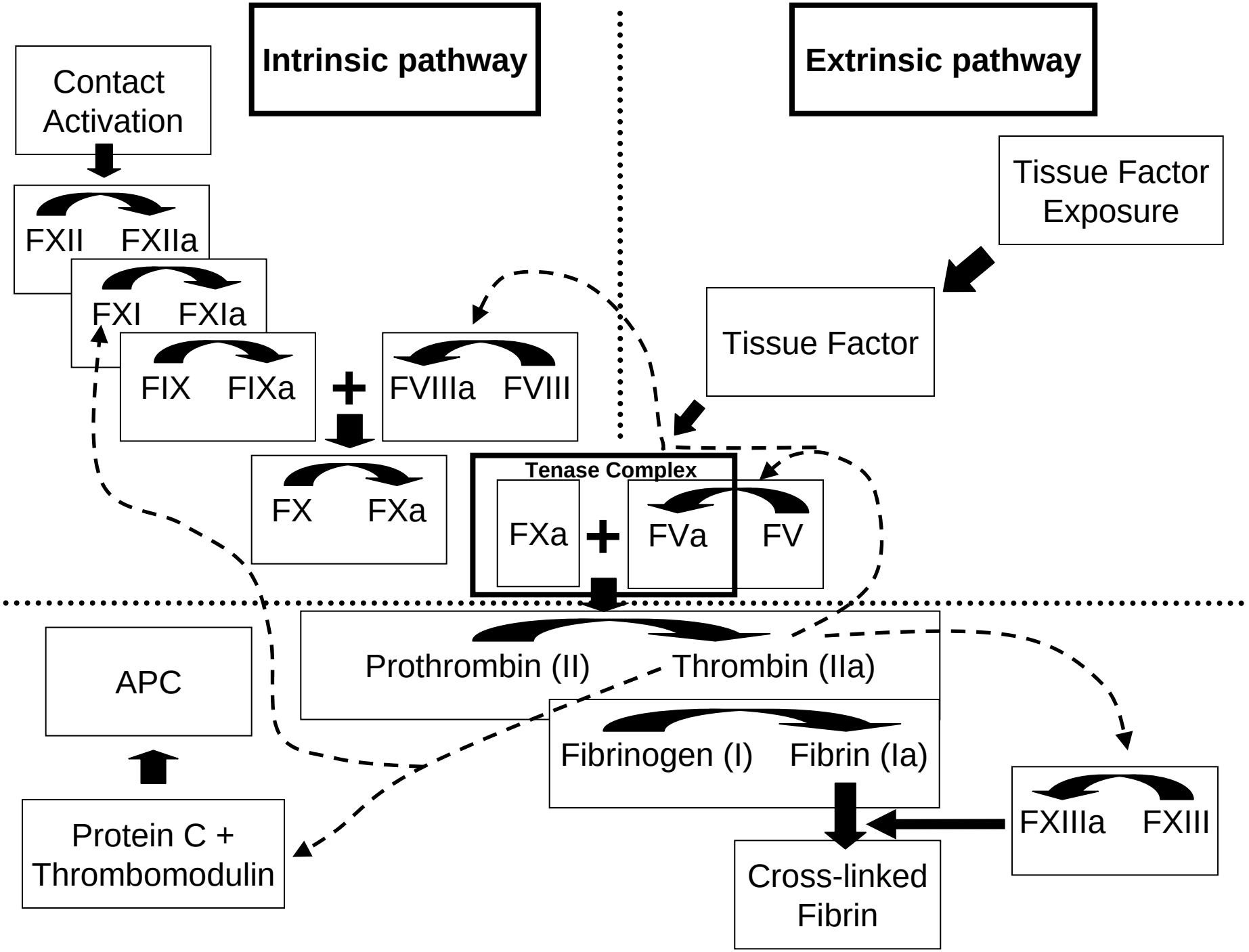
Intrinsic pathway
Extrinsic pathway
Contact Activation
FXII FXIIa
FXI FXIa
FIX FIXa
FVIIIa FVIII
Tissue Factor Exposure
Tissue Factor
FX FXa
Tenase Complex
FXa
FVa FV
Prothrombin (II) Thrombin (IIa)
APC
Fibrinogen (I) Fibrin (Ia)
FXIIIa FXIII
Protein C + Thrombomodulin
Cross-linked Fibrin

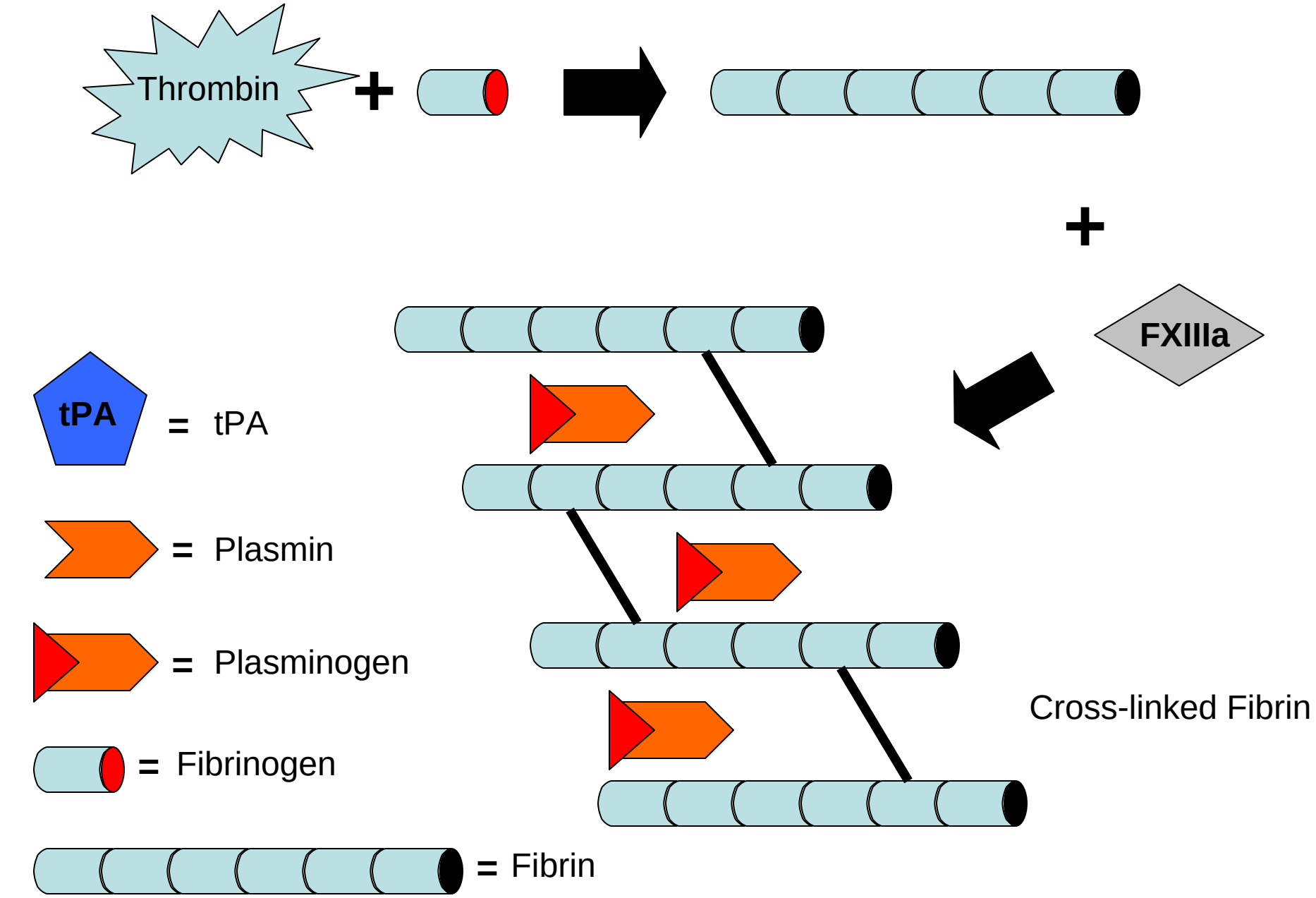
Thrombin
+
+
FXIIIa
tPA
= tPA
= Plasmin
= Plasminogen
= Fibrinogen
= Fibrin
Cross-linked Fibrin

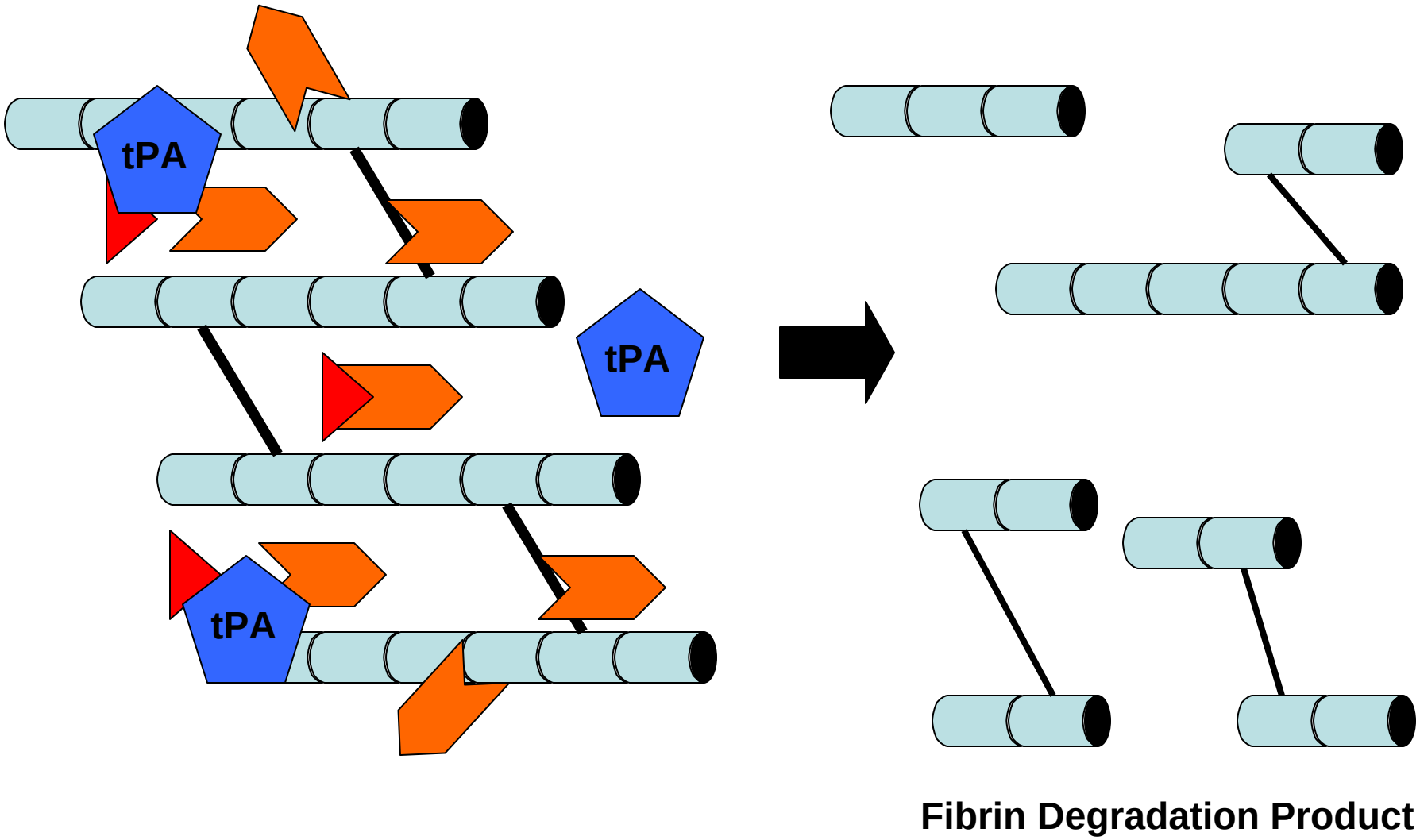
tPA
tPA
tPA
Fibrin Degradation Product

What is the cause of Cerebrovascular Disease?

Thrombi are ***not blood clots***

Thrombus is an <u>intravascular</u> body **comprising fibrin, platelets, and leukocytes at 10 to 50-fold higher concentration than blood**

Thrombi that *occlude* arteries, capillaries, or veins can cause thrombotic and thrombo-embolic diseases

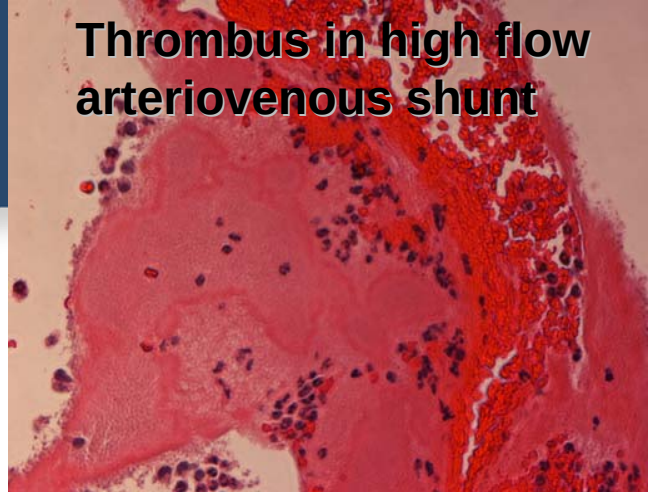

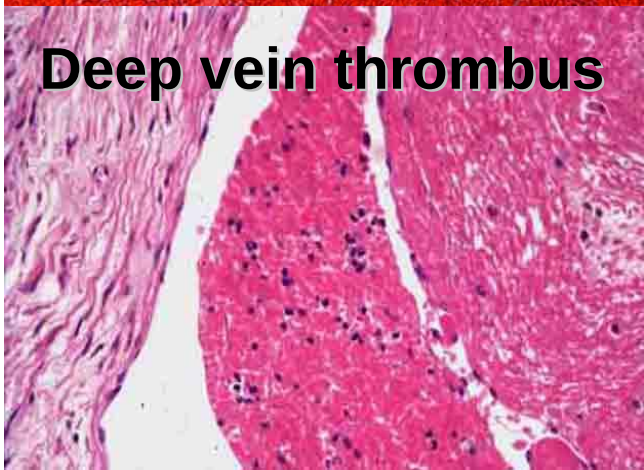

Summary

- Background
- Hemostasis and Thrombolysis
- **Effect of tPA on MCAO mouse model**
- Development of OMAG
- Use OMAG to quantify tPA effect
- Conclusion and future work

Middle Cerebral Artery Occlusion mouse model

- Experimentally induced ischemic stoke model in mice.
- Standard mouse model for experimental stoke.
- Controllable occlusion and reperfusion.
- Transcranial doppler flow measurement.
- Measures infarct volume, behavioral outcome, edema and blood flow recovery.

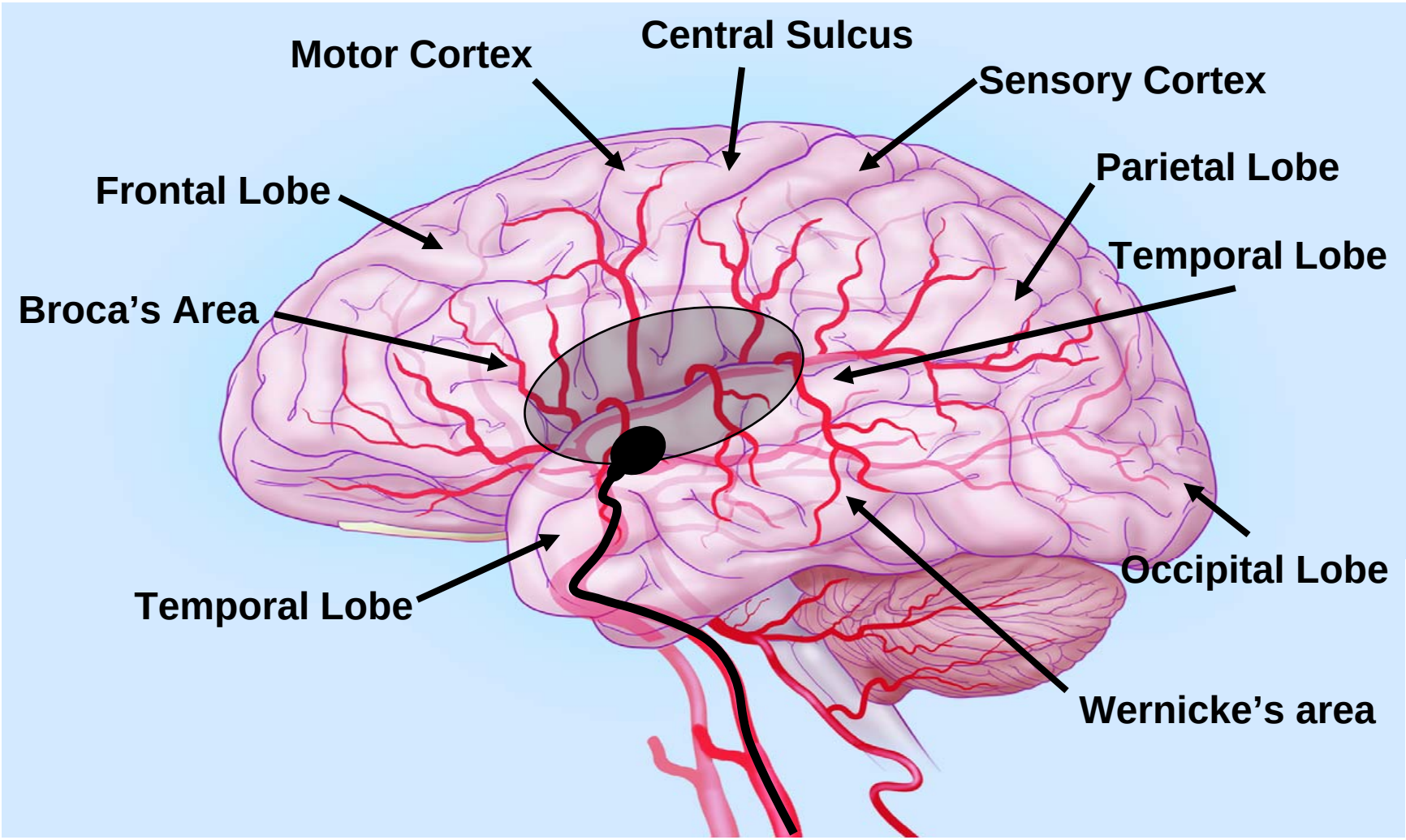
Motor Cortex
Central Sulcus
Sensory Cortex
Frontal Lobe
Parietal Lobe
Temporal Lobe
Broca's Area
Occipital Lobe
Temporal Lobe
Wernicke's area

Laser Doppler Flow (LDF) Monitor

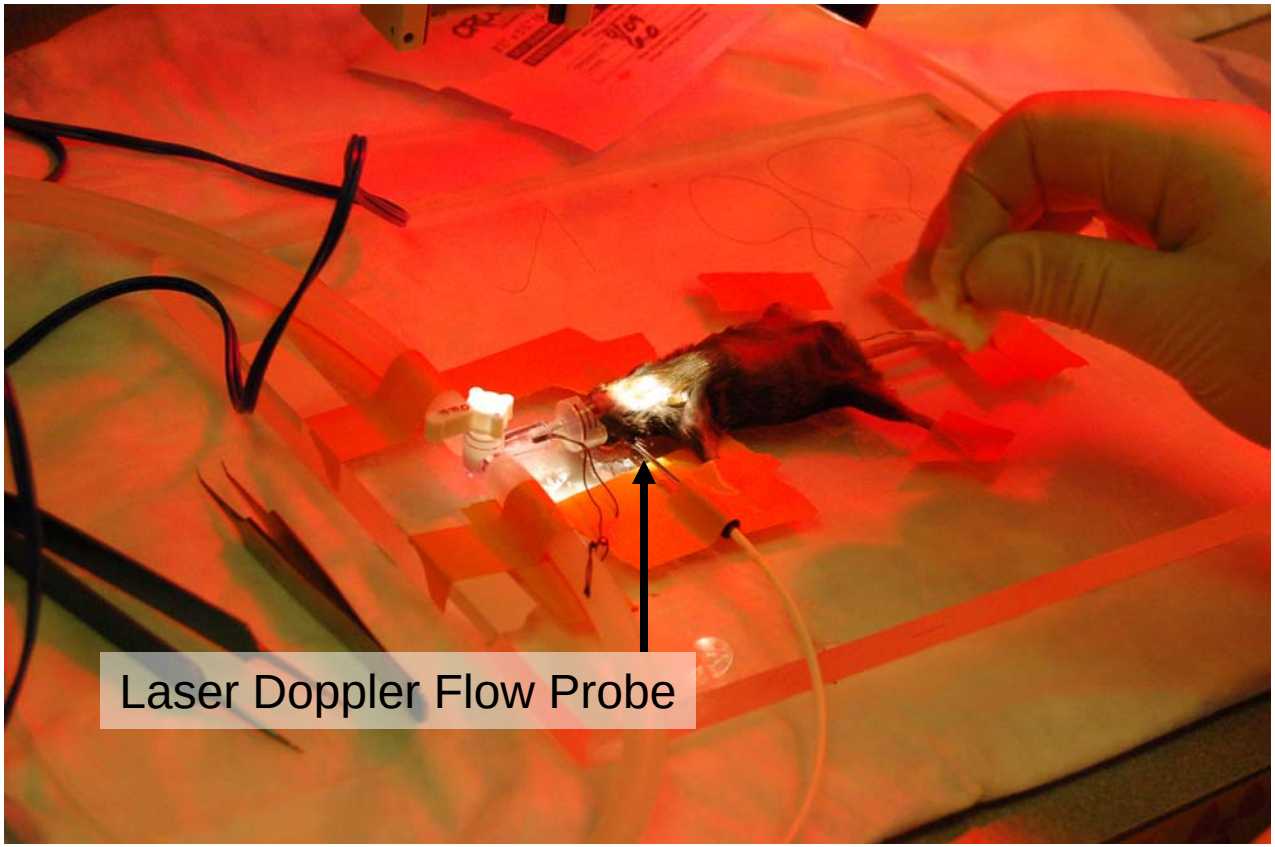

Surgically induced occlusion

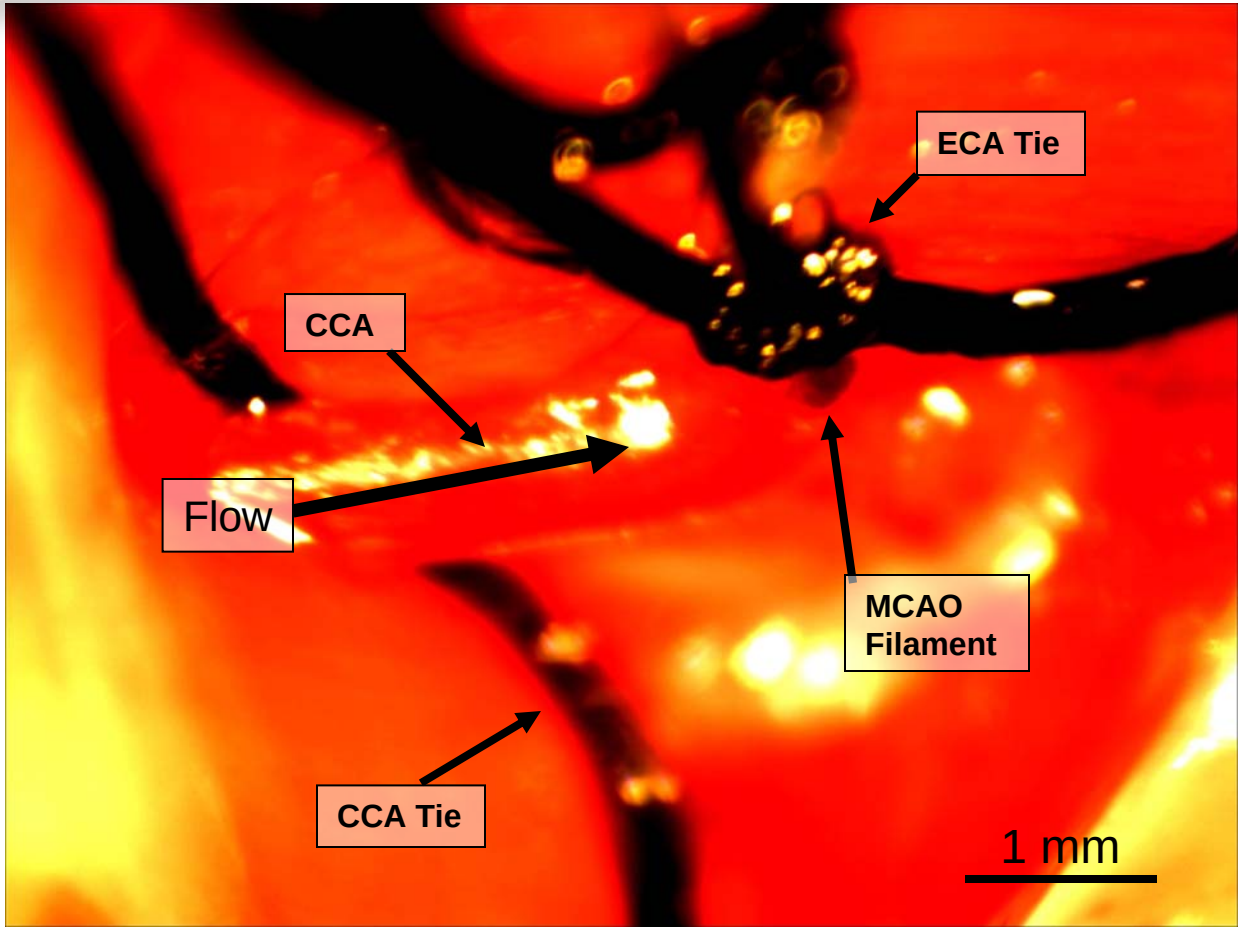

Standard analysis of tPA effect on Mouse

Treatment	Dose	N (number of animals evaluated that survive MCAO surgery)	Mortality (number of deaths between 2 and 24 hours post MCAO)	Hemorrhage (macroscopic intracranial bleeding)	Infarct (% ipsilateral hemisphere, mean ± SEM)	Edema (% ipsilateral hemisphere, mean ± SEM)	Neurology (24 hour behavior performace score, mean ± SEM)	Blood flow (% of baseline at 15 min post-reperfusion, mean ± SEM)
None	-	10	3/13	3/13	60.0 ± 6.7	11.4 ± 1.1	3	ND
Vehicle	0.9% NaCl; IV infusion at 15-60 min, 185 µL	10	2/12	3/12	58.0 ± 5.6	9.0 ± 1.9	4	47.0 ± 3.0
tPA	10 mg/kg/hr; IV infusion at 15-60 min during MCAO, 185 µL	10	3/13	4/13	15.9 ± 4.9	6.7 ± 1.0	2	81.0± 5.2

2,3,5-triphenyltetrazolium chloride (TTC) Stained Brains

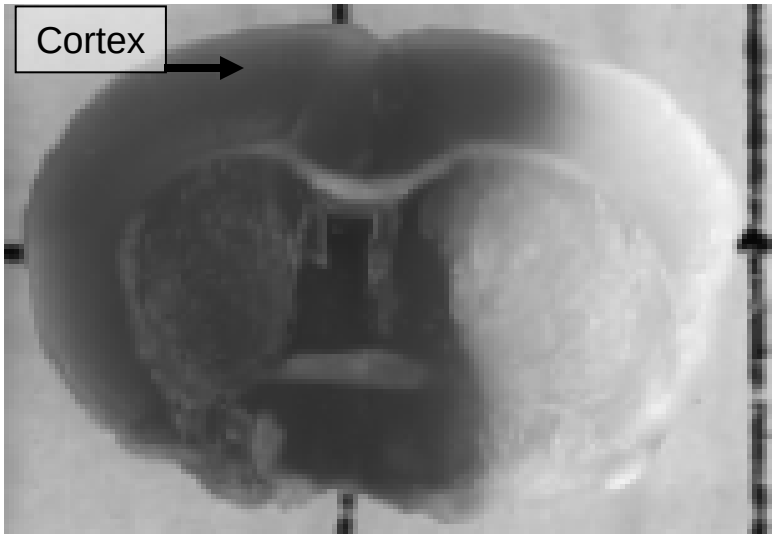

Vehicle

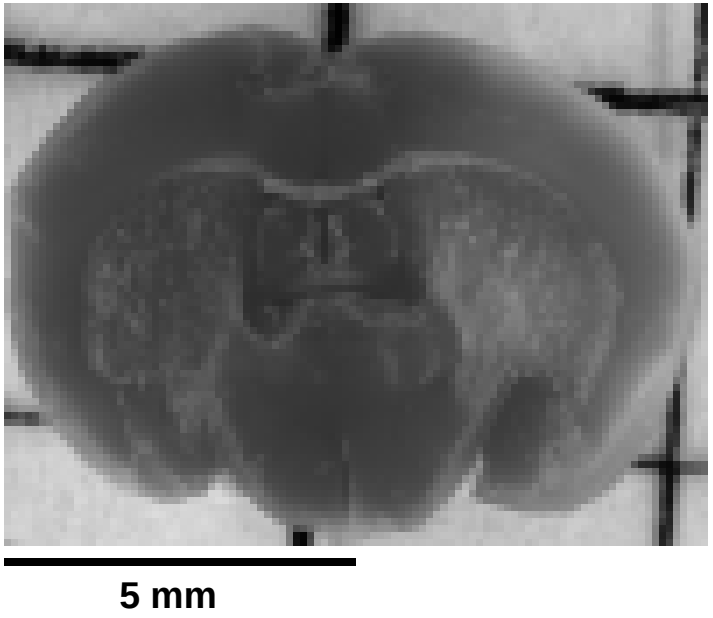

tPA infusion

Hara Behavioral Scoring

Behavioral scale used to score animal 24 hours after post-ischemic injury.

0 = normal motor function.

1 = flexion of contralateral torso and forelimb.

2 = circling to contralateral side, normal posture.

3 = leaning to contralateral side, posture change.

4 = no spontaneous motor activity.

5 = death.

(Atochin, D.N. 2003)

Behavior and Infarct Analysis

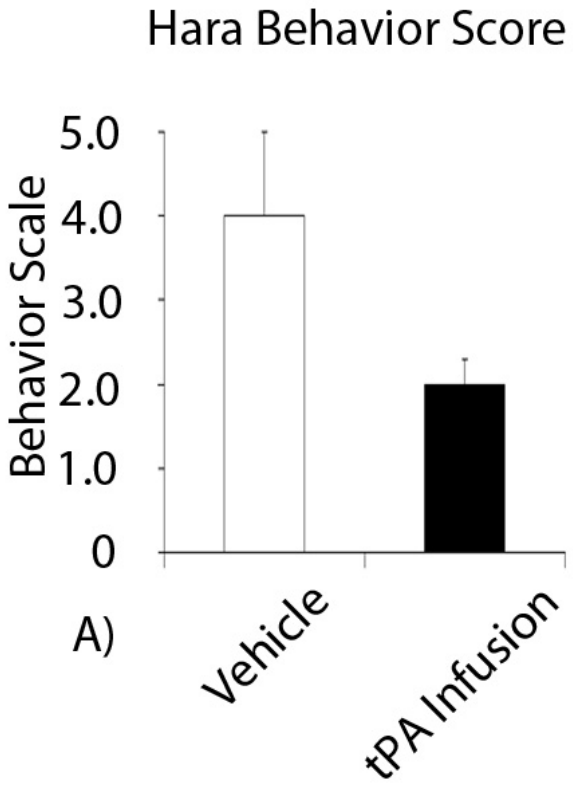

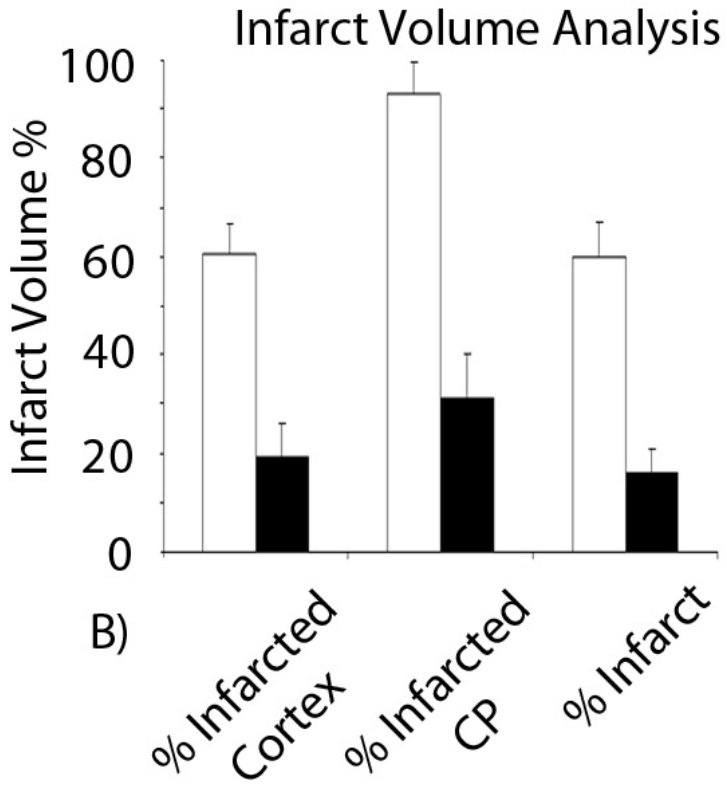

Summary

- Background
- Hemostasis and Thrombolysis
- Effect of tPA on MCAO mouse model
- **Development of OMAG**
- Use OMAG to quantify tPA effect
- Conclusion and future work

Optical microangiography (OMAG)

- Optical Coherence Tomography (OCT).
- Non-invasive optical imaging technique.
- Static and Dynamic information from the reflectance through tissue depth imaged.
- Blood perfusion is the endogenous contrast which causes light scattering.
- OMAG can be used to obtain real time perfusion images

OMAG signal from Real sample

$$I(t,k_j) = S(k_j)\{E_R^2 + 2E_R\int_{-\infty}^{\infty} a(z,t)\cos(2k_j n(z,t)z)dz + 2E_R a(z_1,t)\cos[2k_j n(z_1,t)(z_1 - vt)]\}$$

The signal obtained by the CCD camera:

j: *the pixel of the CCD camera;* ***k_j:*** *the wave number of the nth pixel;*

z: *relative distance between reference mirror and the scatters within the sample;*

$S(k_j)$: *is the spectral density of the light source at kj;* ***v:*** *velocity of moving particles;*

t: *sampling time which corresponding to lateral position.*

n: *is the refractive index of the sample;* ***a:*** *is the amplitude of the light.*

- **Sample used in our experiment, (e.g. mouse head) is optically heterogeneous**

OMAG system setup

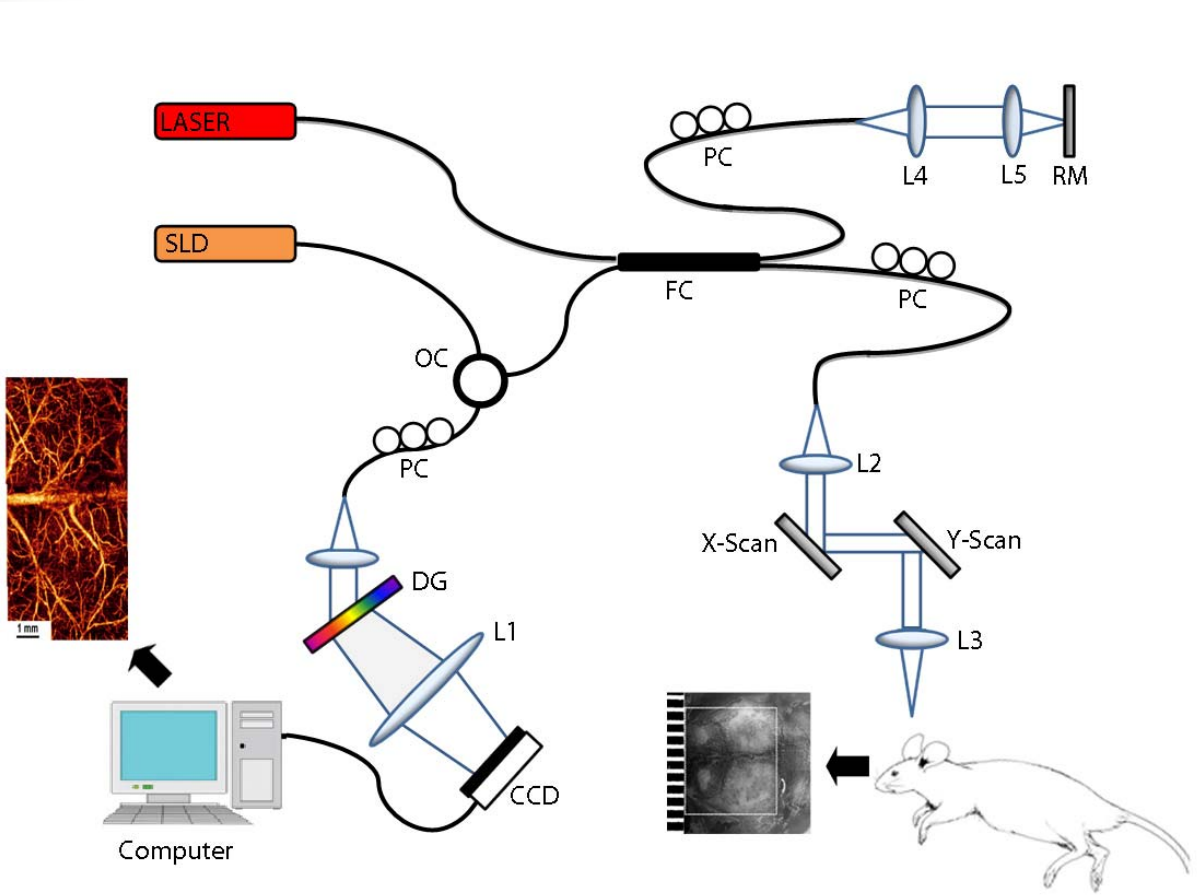

OREGON HEALTH & SCIENCE UNIVERSITY

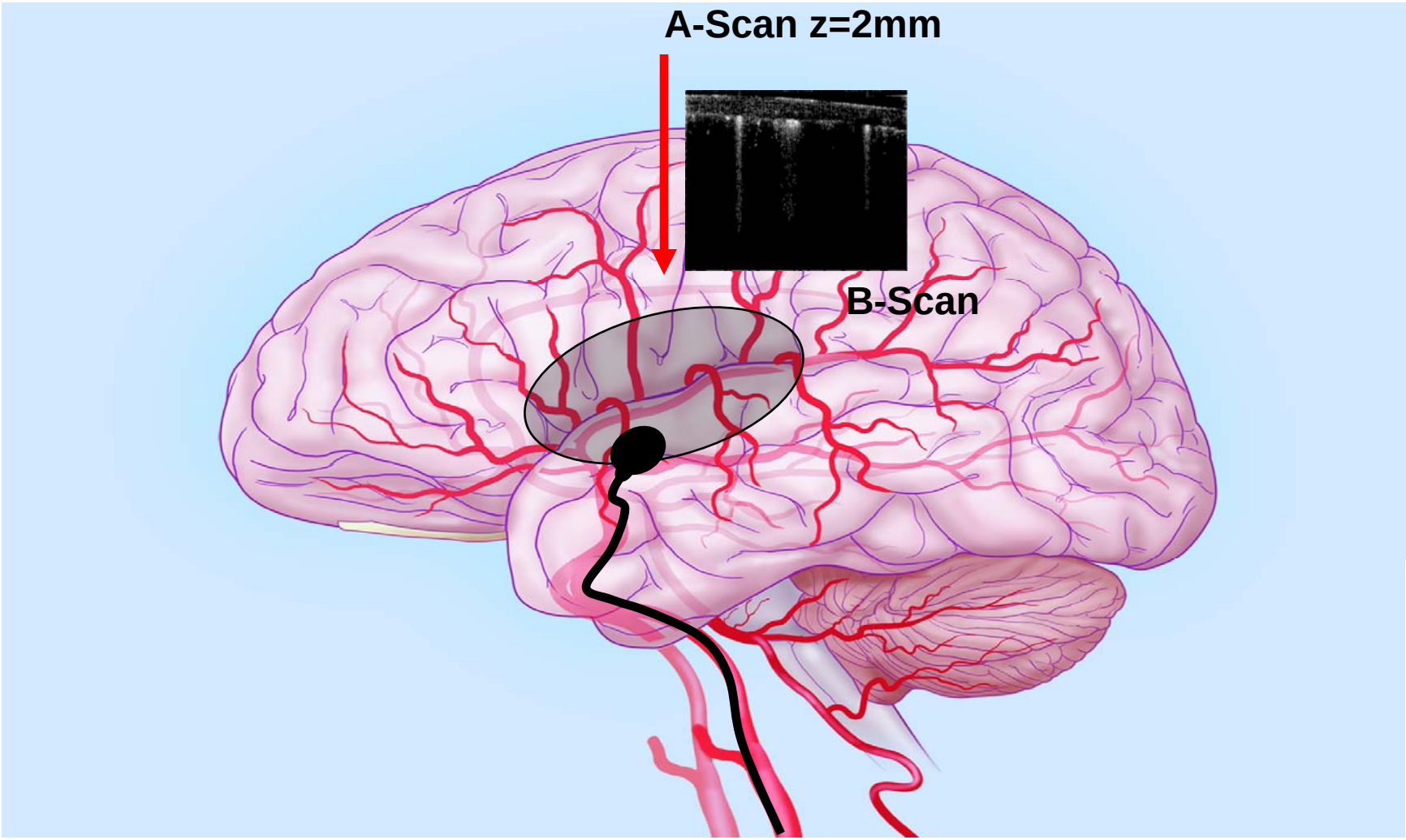
A-Scan z=2mm
B-Scan

OMAG image voxel area

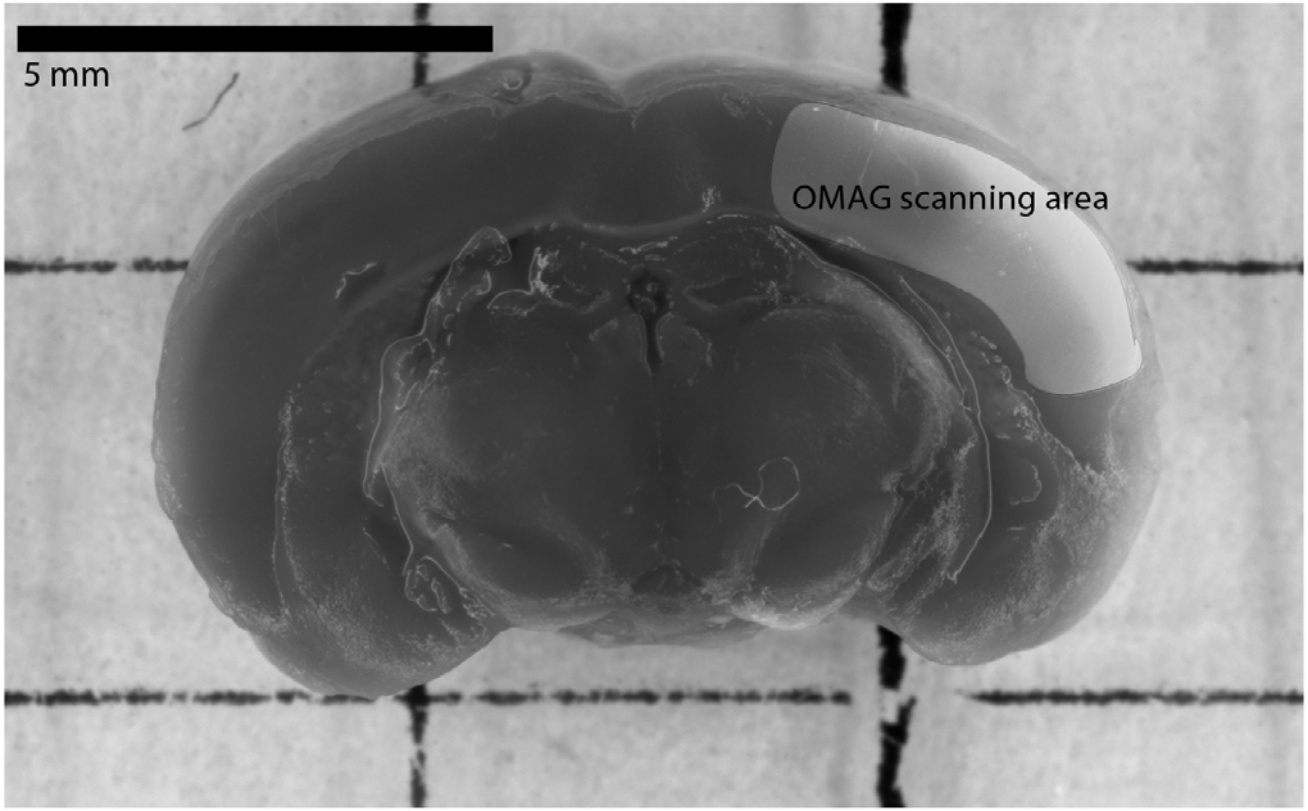

1 scan = 2.2 X 2.2 mm^2 with 1.7 mm depth

Experiment in Progress

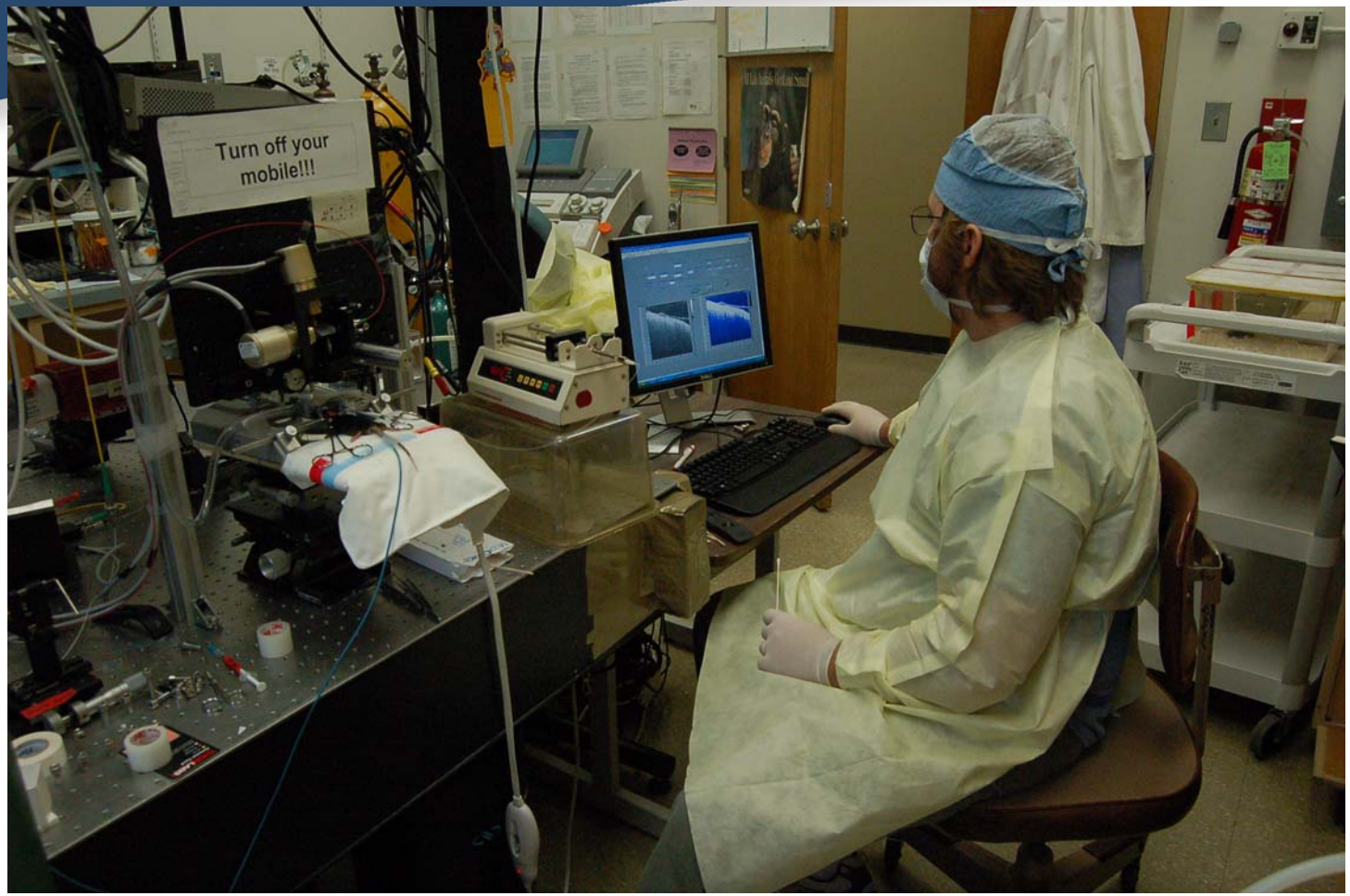

OREGON HEALTH & SCIENCE UNIVERSITY

Summary

- Background
- Hemostasis and Thrombolysis
- Effect of tPA on MCAO mouse model
- Development of OMAG
- **Use OMAG to quantify tPA effect**
- Conclusion and future work

Quantification of blood flow

1) Laser Doppler Flow (LDF) quantification:

Small volume sampled.

Single large vessel flow monitored.

2) Iodoantipyrine (IAP) quantification:

Standard blood perfusion measurement technique.

Invasive radiolabeled blood perfusion measurement.

Quantification of Flow Velocities

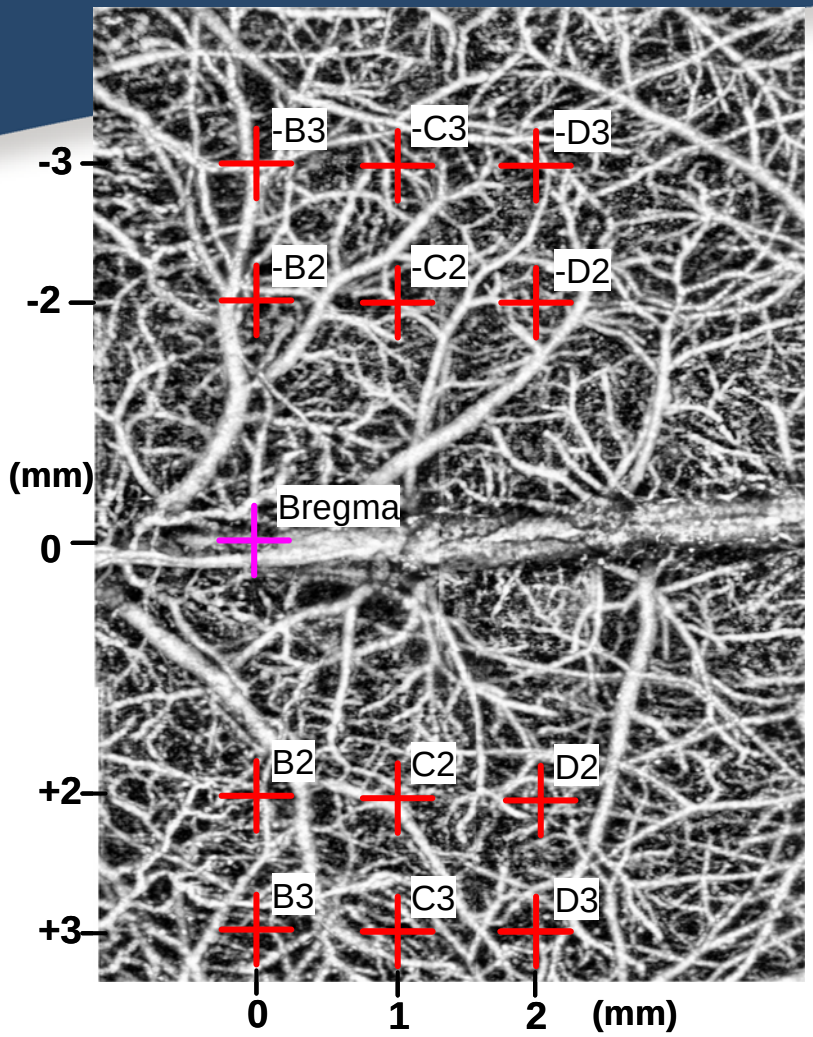

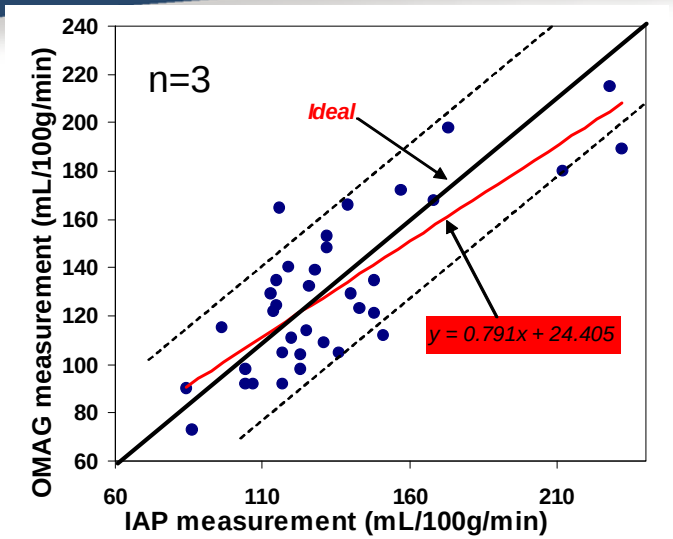

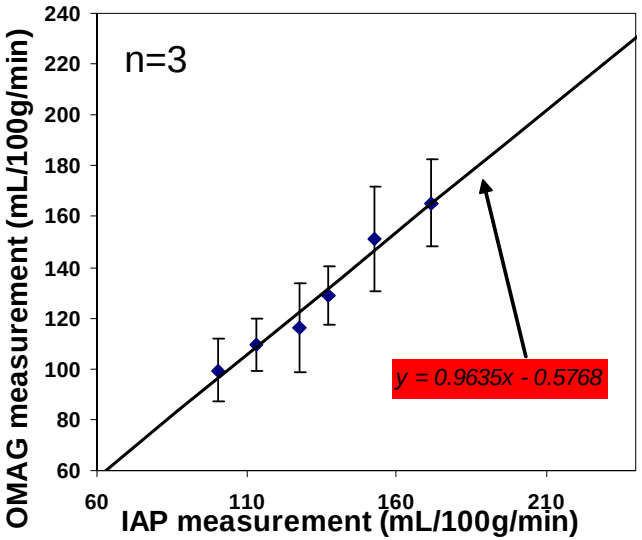

(Zhang, Wenri et al. 2009)

3D vehicle treated progressive stroke

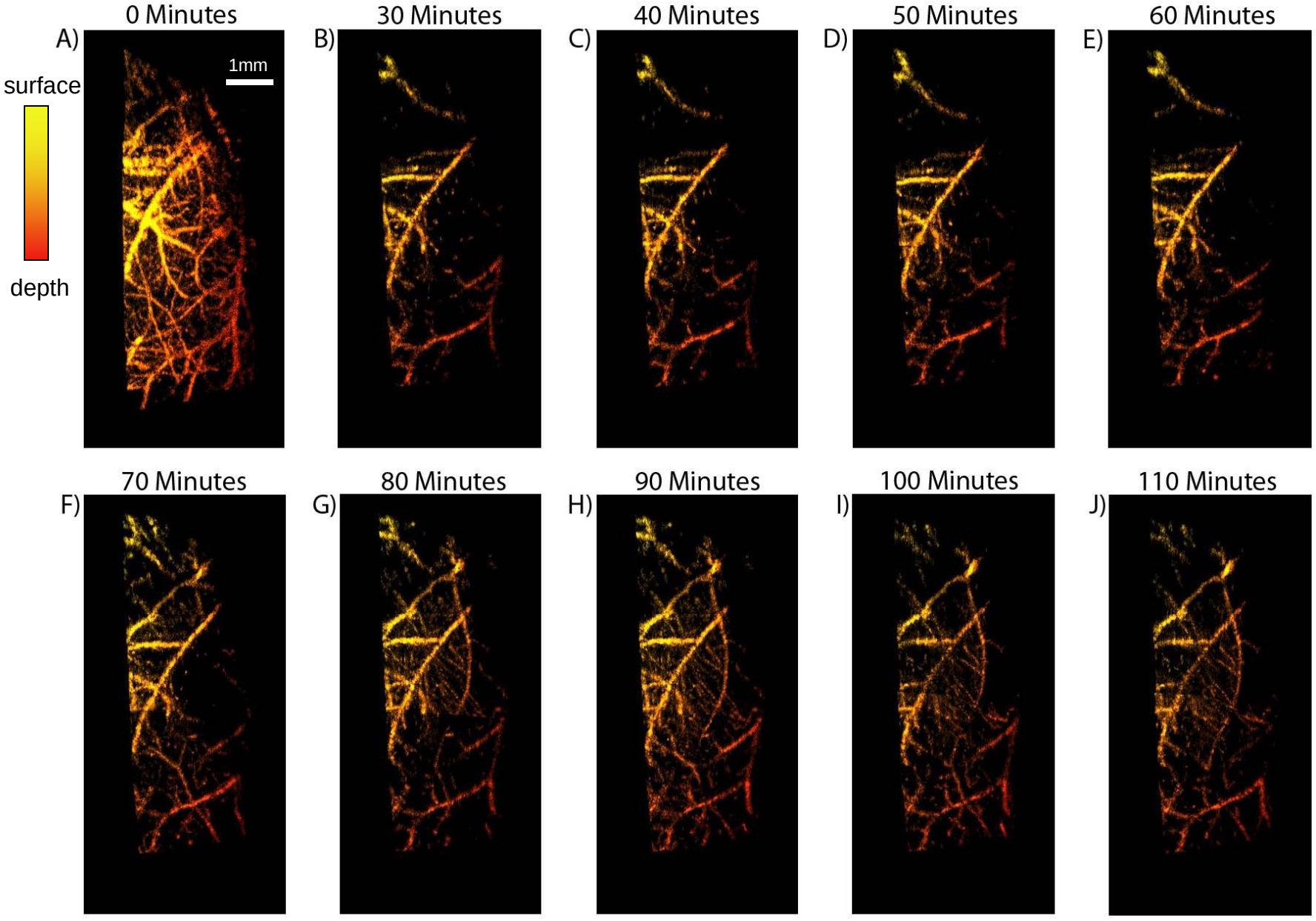

2D vehicle treated progressive stroke

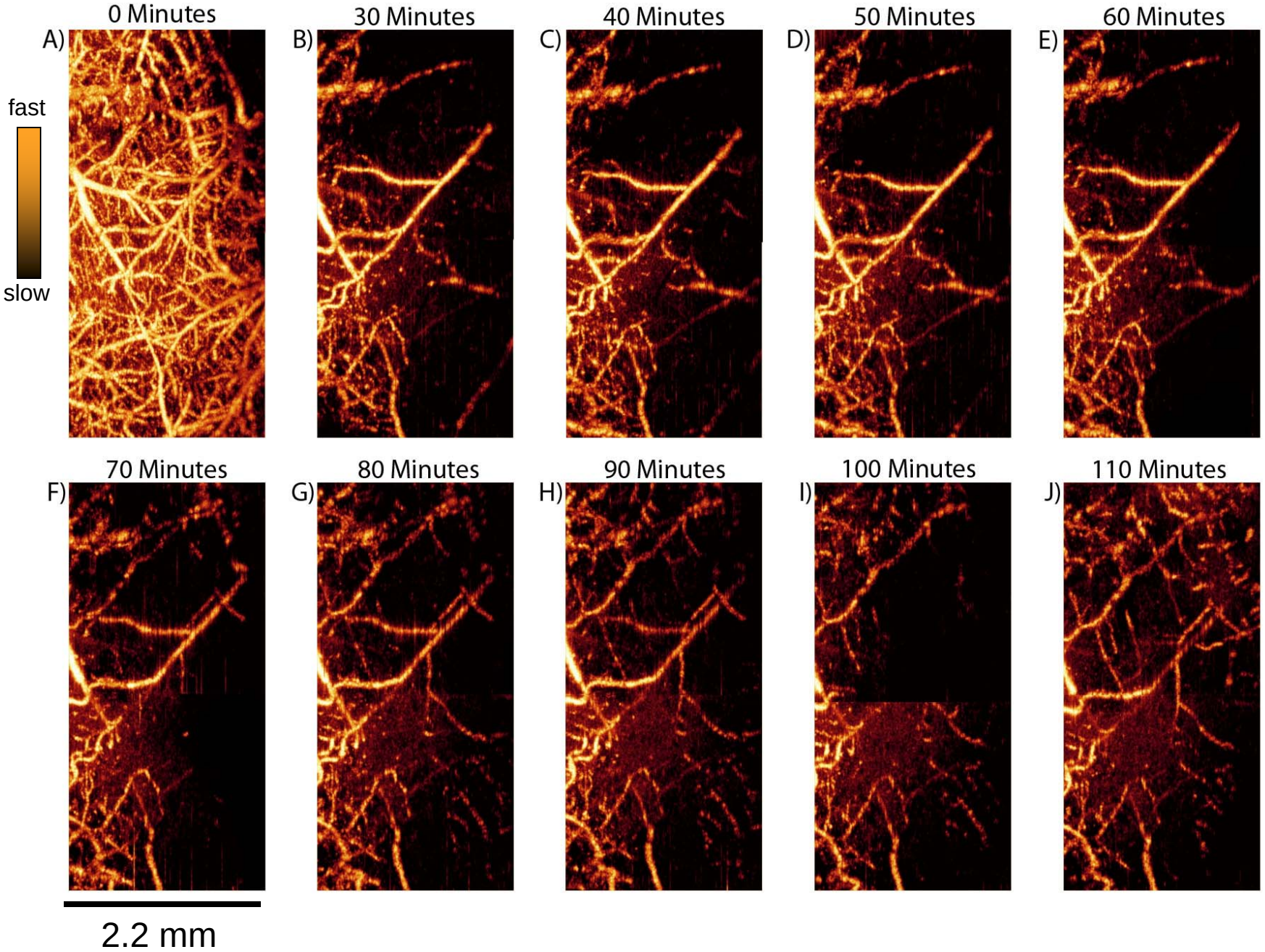

3D tPA treated progressive stroke

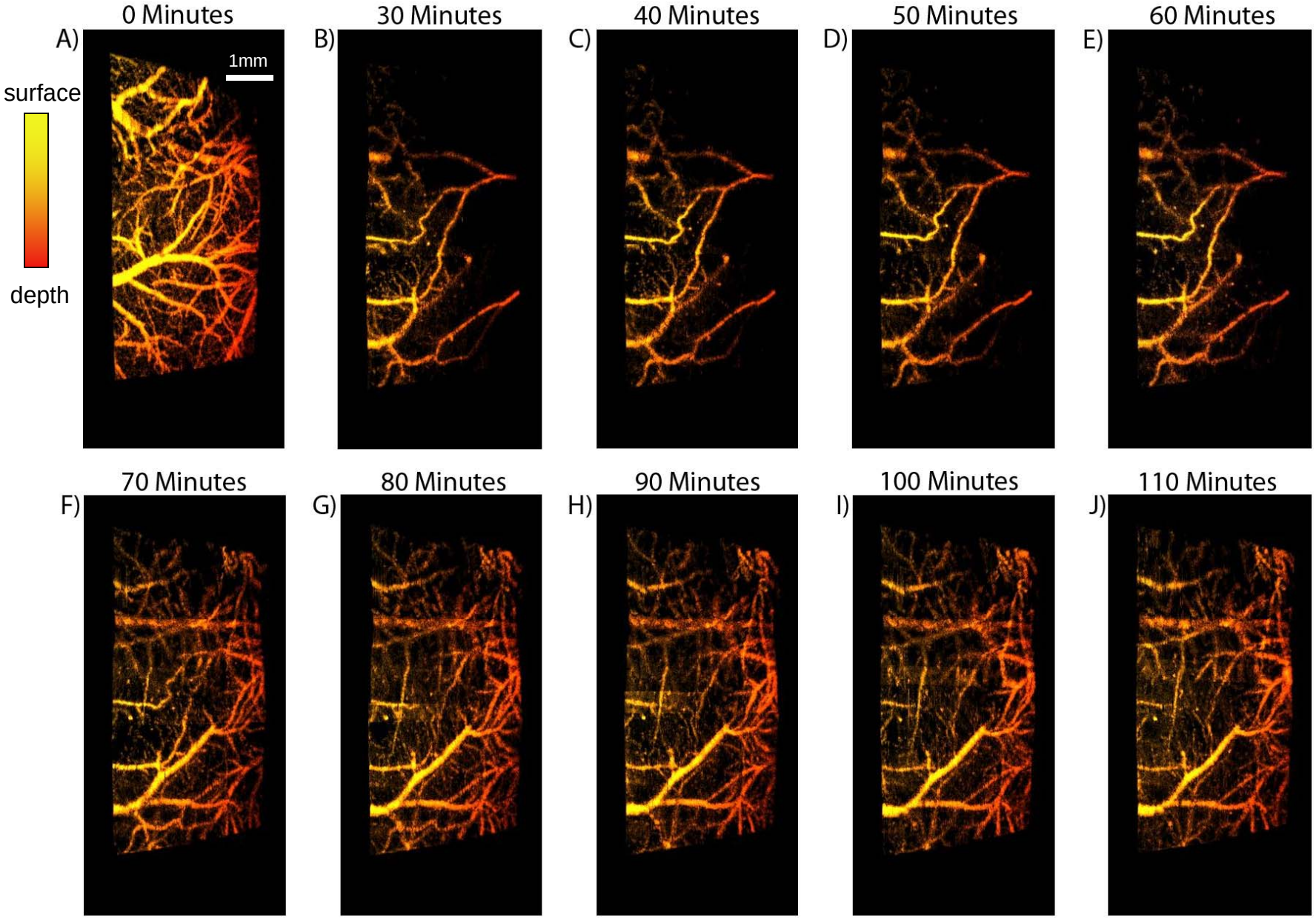

2D tPA treated progressive stroke

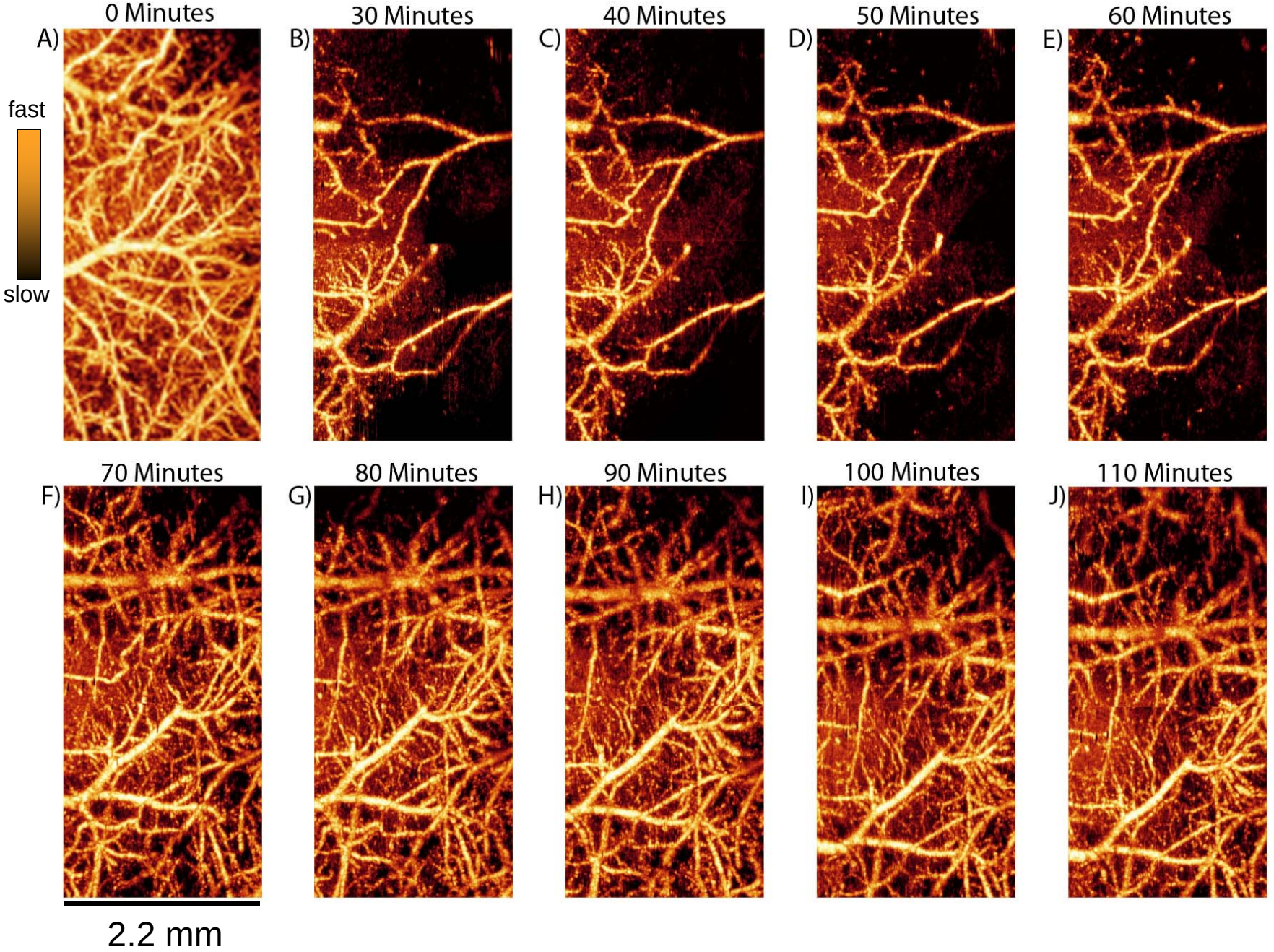

3D OMAG movie of MCAO time progression

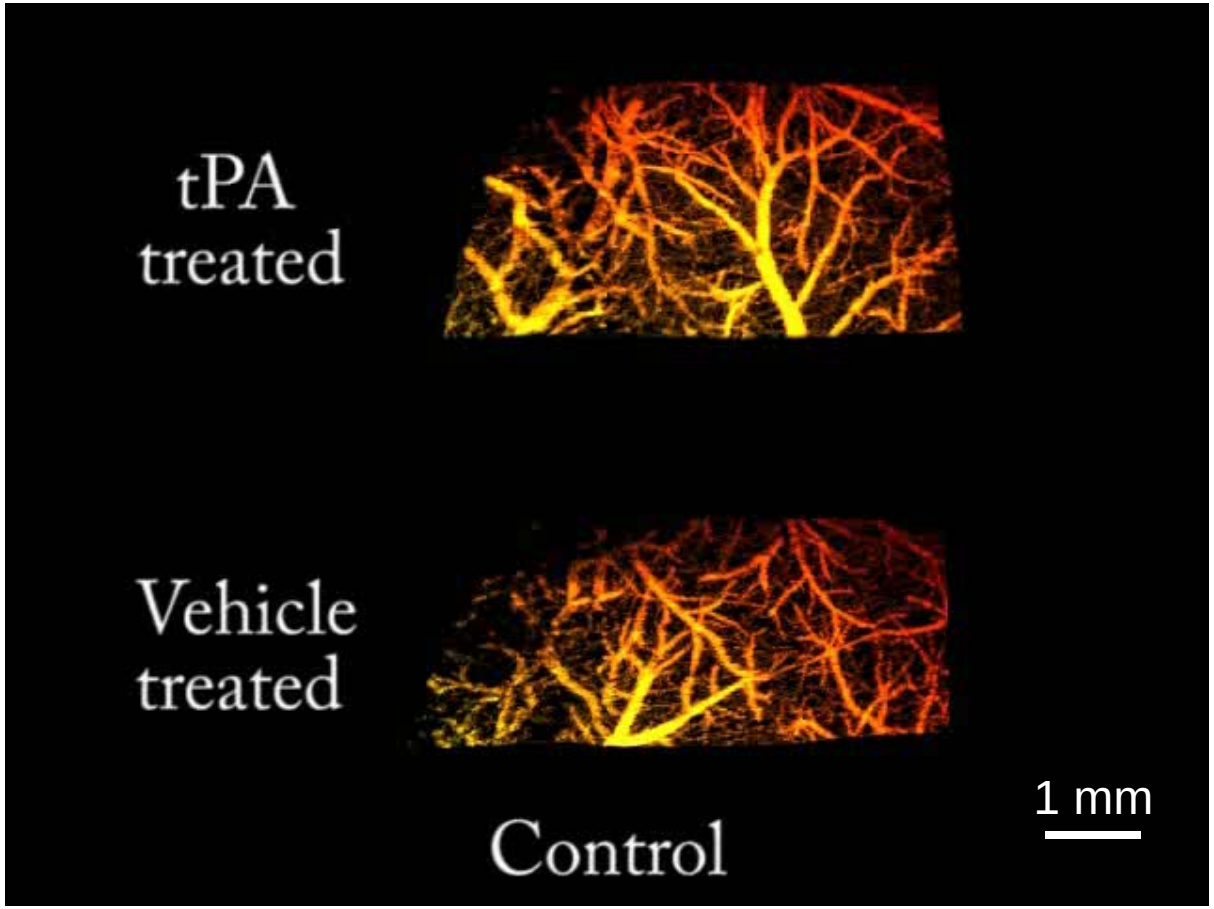

OMAG volume and LDF flow graphs

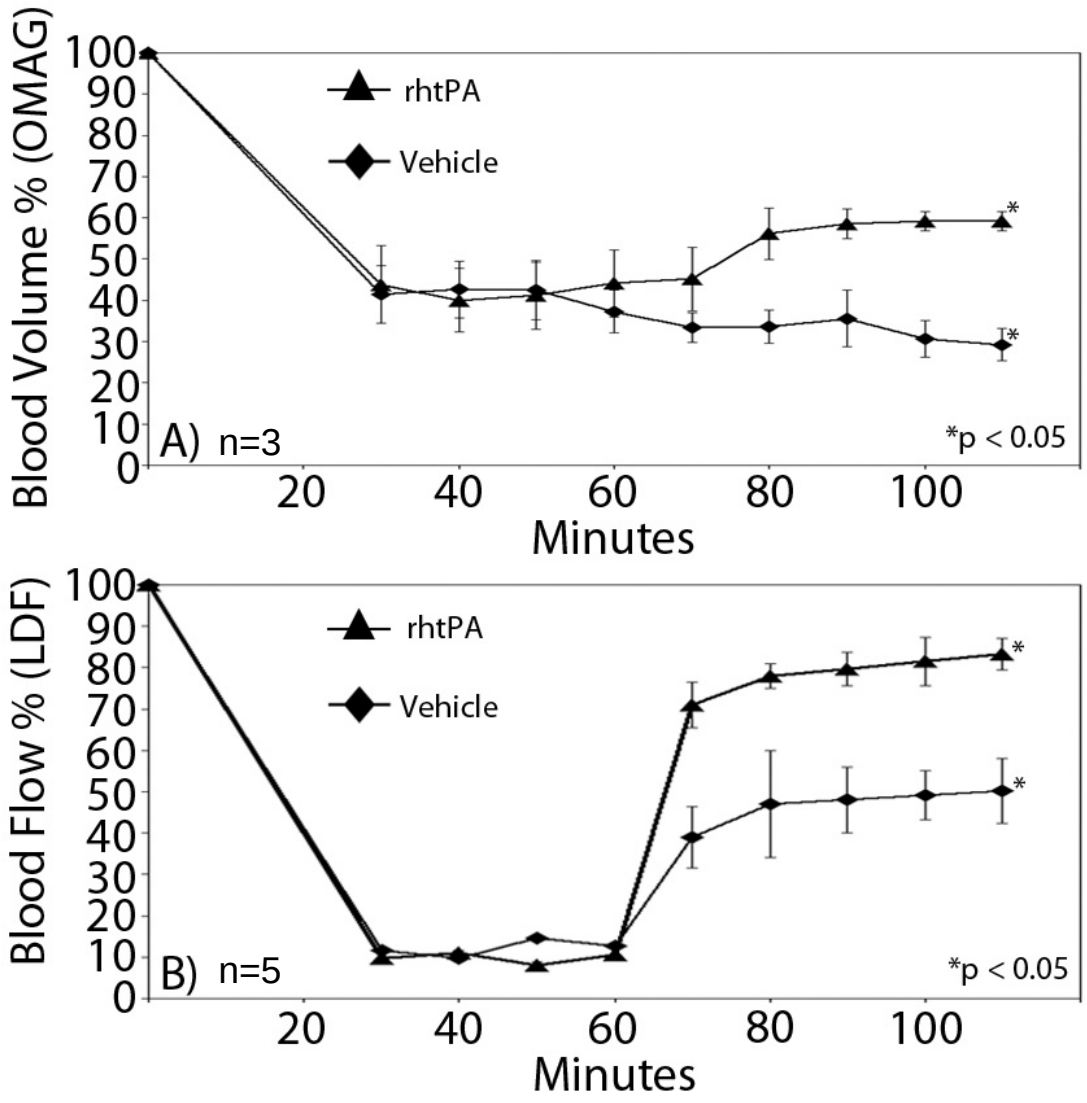

OREGON HEALTH & SCIENCE UNIVERSITY

Conclusion and future work

- OMAG can quantify reperfusion by imaging real time *in vivo* progression of blood flow.
- OMAG has more quantification ability compared to LDF.
- tPA works by increasing reperfusion after ischemic injury.
- Future work; use OMAG to evaluate other pharmaceutical stroke treatments.
- Quantify blood perfusion limits for system.
- Use OMAG to do functional analysis of vessels.

Acknowledgements

Funding:

- NIH R01HL093140-01
- NIH R01EB009682-01
- AHA 0855733G
- AHA 0850056Z
- Department of Biomedical Engineering
- Ruth L. Kirschstein National Research Service Award

Committee Members:

R.K. Wang, PhD
Andras Gruber, MD
Owen McCarty, PhD
Nabil Alkayed, MD, PhD

Yali Jia
An Lin
Yin Xin
Wenri Zhang
Erik Tucker

OREGON HEALTH & SCIENCE UNIVERSITY

Thank you

OREGON HEALTH & SCIENCE UNIVERSITY